OULU 2020
C 756

ACTA
UNIVERSITATIS OULUENSIS

Mohammed Ali

DEVELOPMENT OF LOW-COST CrNiMoWMnV ULTRAHIGH-STRENGTH STEEL WITH HIGH IMPACT TOUGHNESS FOR ADVANCED ENGINEERING APPLICATIONS

UNIVERSITY OF OULU GRADUATE SCHOOL;
UNIVERSITY OF OULU,
FACULTY OF TECHNOLOGY

ACTA UNIVERSITATIS OULUENSIS
C Technica 756

MOHAMMED ALI

DEVELOPMENT OF LOW-COST CrNiMoWMnV ULTRAHIGH-STRENGTH STEEL WITH HIGH IMPACT TOUGHNESS FOR ADVANCED ENGINEERING APPLICATIONS

Academic dissertation to be presented with the assent of the Doctoral Training Committee of Technology and Natural Sciences of the University of Oulu for public defence in the OP auditorium (L10), Linnanmaa, on 28 August 2020, at 12 noon

UNIVERSITY OF OULU, OULU 2020

Copyright © 2020
Acta Univ. Oul. C 756, 2020

Supervised by
Professor Jukka Kömi
Professor David Porter
Professor Mamdouh Eissa
Professor Taha Mattar

Reviewed by
Professor Pasi Peura
Associate Professor Anders Tilliander

Opponents
Professor Pasi Peura
Professor Lauri Holappa

ISBN 978-952-62-2671-2 (Paperback)
ISBN 978-952-62-2672-9 (PDF)

ISSN 0355-3213 (Printed)
ISSN 1796-2226 (Online)

Cover Design
Raimo Ahonen

PUNAMUSTA
TAMPERE 2020

Ali, Mohammed, Development of low-cost CrNiMoWMnV ultrahigh-strength steel with high impact toughness for advanced engineering applications.

University of Oulu Graduate School; University of Oulu, Faculty of Technology
Acta Univ. Oul. C 756, 2020
University of Oulu, P.O. Box 8000, FI-90014 University of Oulu, Finland

Abstract

Increasing carbon dioxide (CO_2) emissions from steel plants due to ever-growing steel production make the increased use of scrap-based production routes more attractive. Also, increasing demands for ultrahigh-strength steels (UHSSs) in commercial and military applications have raised interest in finding alternatives to the expensive steels currently used.

This thesis studies the possibilities of using low-cost air induction melting followed by refining using electroslag remelting (ESR) for the production of ultrahigh-strength, tough steel. The influence of ESR on the chemical composition, cleanliness, microstructure, and mechanical properties of novel martensitic and martensitic-bainitic UHSSs is examined to provide a good platform for the future production of tough UHSSs using the above-mentioned route. As a starting point for the studies of the steels concerned, the effect of cooling rate from austenite on phase transformation temperatures and final microstructures, as well as the mechanical properties in the as-cooled, untempered condition, are examined. Also, the evolution of precipitation and microstructure during the thermomechanical processing of austenite is described. Furthermore, the influence of double austenitization and quenching followed by tempering at 200 °C is discussed.

ESR is shown to lead to a high yield of alloying elements, low levels of impurities and non-metallic inclusions (NMIs) and a refinement of the final microstructures due to slight changes in the chemical composition. The effect of ESR on mechanical properties depends on the steel composition.

For the studied steels, the cooling rates leading to the formation of martensite provide a better combination of strength and toughness than a cooling rate that leads to proeutectoid carbides and granular bainite.

It is shown that good combinations of strength and toughness can be obtained through the use of the following process route: low-cost air induction melting, ESR, and temperature-controlled forging and cooling followed by reheating, quenching and tempering at 200 °C. Charpy-V impact toughness can be improved by applying double austenitization and quenching prior to tempering.

Keywords: cleanliness, continuous cooling transformation diagrams, electroslag remelting, heat treatments, impact toughness, microstructure features, non-metallic inclusions, steel recycling, strain induced precipitates, tensile properties, thermomechanical processing, ultrahigh-strength steels

Ali, Mohammed, Edullinen ja kylmänkestävä CrNiMoWMnV-tyyppinen ultraluja rakenneteräs vaativiin käyttökohteisiin.

Oulun yliopiston tutkijakoulu; Oulun yliopisto, Teknillinen tiedekunta
Acta Univ. Oul. C 756, 2020
Oulun yliopisto, PL 8000, 90014 Oulun yliopisto

Tiivistelmä

Kasvihuonepäästöt (CO_2) kasvavat jatkuvasti, koska teräksen valmistus ja kulutus lisääntyvät. Tämä lisää kiinnostusta myös romupohjaiseen teräksenvalmistukseen, koska se mahdollistaa päästöjen vähentämisen. Lisäksi nykyisille ultralujille teräksille, joita voidaan käyttää erilaisissa kaupallisissa sovelluksissa, haetaan valmistusteknisesti edullisempia vaihtoehtoja.

Opinnäytetyössä selvitettiin mahdollisuutta hyödyntää ultralujien teräksen valmistuksessa teknisesti edullisen induktiosulatuksen ja sähkökuona-uudelleensulatuksen (ESR = electroslag remelting) yhdistelmää. ESR:n vaikutusta selvitettiin uusien martensiittisten ja martensiittis-bainiittisten ultralujien terästen kemialliseen koostumukseen, epäpuhtauksiin, mikrorakenteeseen ja mekaanisiin ominaisuuksiin. Tarkoituksena on mahdollistaa ultralujien terästen tehokas tuotanto tällä valmistusteknologialla. Lähtökohtana on jäähdytysnopeuden vaikutus austeniitti-ferriitti faasinmuutoslämpötiloihin sekä niiden vaikutus mikrorakenteisiin ja mekaanisiin ominaisuuksiin, kun teräksiä ei ole päästökäsitelty. Tähän yhdistettiin kaksinkertainen austenointi-, karkaisu- ja 200 °C päästökäsittely. Lisäksi tutkimuksessa selvitettiin myös erkaumien ja mikrorakenteen muodostuminen termomekaanisessa kuumamuokkauksessa.

Tutkimuksessa osoitettiin, että ESR:n tekniikka johtaa erittäin hyvään seosaineiden tuotokseen, niiden pieneen hajontaan, alhaiseen epäpuhtaustasoon ja siten vähäiseen määrään ei-metallisia sulkeumia. Tällöin saadaan lopputuotteen mikrorakenne ja mekaaniset ominaisuuden tarkasti optimoitua ja ominaisuushajonta jää varsin pieneksi.

Tutkituille teräksille jäähdytysnopeudet, jotka aikaansaavat martensiitin muodostumisen, antavat paremman lujuus-sitkeys yhdistelmän kuin jäähdytysnopeus, joka johtaa esieutektoidisen karbidin ja granulaarisen bainiittiin muodostumiseen.

Tutkimuksessa osoitettiin, että erinomaiset lujuuden ja sitkeyden yhdistelmät voidaan saada aikaan käyttämällä prosessireittiä: induktiosulatus, ESR, lämpötilakontrolloitu taonta ja jäähdytys, jota seuraa uudelleenkuumennus, karkaisu ja päästö 200 °C. Lisäksi kylmänkestävyyttä (Charpy-V testi) voidaan parantaa käyttämällä kaksinkertaista austenitointia, karkaisua ja päästöä.

Asiasanat: ei-metalliset sulkeumat, iskusitkeys, jatkuvan jäähtymisen käyrä, jännityksen aiheuttamat erkaumat, lämpökäsittely, mikrorakenteen ominaisuudet, puhtaus, sähkökuona-uudelleensulatus, termomekaaninen käsittely, teräksen kierrätys, ultralujat teräkset, vetolujuus

To the souls of my mother and my father, and to my wife Rehab, My Children Moaz, Malek and Yousef.

Acknowledgements

The work presented in this thesis is based on an industrial project proposed by the Steel Technology Department, Central Metallurgical Research and Development Institute (CMRDI), Cairo, Egypt. It was carried out during 2015-2020 in the Materials and Mechanical Engineering research unit of the Centre of Advanced Steel Research (CASR) at the University of Oulu in collaboration with CMRDI, where I stayed for the first year (2015-2016) for production and refining of the materials investigated in this work, in addition to some preliminary investigations. The forging for all investigated materials has been done in Nasr Forging Company, Cairo, Egypt. The research was funded during 2015-2016 from CMRDI. This thesis was financially supported during 2016-2018 by the Egyptian Ministry of Higher Education (Cultural Affairs and Missions Sector).

I would like to express my deep gratitude to my supervisor, Professor David Porter, for his guidance, continuous supervision and valuable feedback and suggestions for improving all my research works and articles in this thesis. I thank my supervisor Professor Jukka Kömi, for his help and support during this work. I wish to thank my supervisors from CMRDI, Professor Mamdouh Eissa and Professor Taha Mattar, for their supervision and guidance during my stay in Egypt at the beginning of this project. I would like to thank Dr. Eetu-Pekka Heikkinen from the Process Metallurgy Research Unit at the University of Oulu for his collaboration for some thermodynamic calculations.

Furthermore, I would like to thank my colleagues at the Materials and Mechanical Engineering research unit for creating a friendly and productive research environment at work. Also, I would like to thank Dr. Jussi Paavola for his help during some heat treatments in this work, Mr. Juha Uusitalo for all Gleeble work performed during this work, Mr. Ilpo Alasaarela and Mr. Tun Nyo for their technical support in the workshop and sample preparation work, and Mr. Henri Tervo for his help at the beginning of my work in University of Oulu. Special thanks to Dr. Mahesh Somani, Dr. Vahid Javaheri, Dr. Antti Kaijalainen, Dr. Sakari Pallaspuro, Dr. Satish Kolli, Mr. Shashank Ramesh Babu for the fruitful and valuable discussion. Special thanks to Mr. Seppo Järvenpää for his help and support from my first day in Finland to the end of this project.

Furthermore, I would like to thank my colleagues from CMRDI, Prof. Hoda El-Faramawy, Prof. Michael Lamie, Prof. Azza Ahmed, Prof. Hossam Halfa, Prof. Saeed Nabil for the fruitful and valuable discussions. Special thanks to Dr. Mohammed El-Fawakhry and Dr. Hassan Bahaa for their countless encouragement,

support and help during my work in Egypt. I would like to thank Mr. Islam Salem, Mr. Mahmoud Sherif and Mr. Ahmed Hamed for their help. Special thanks to Mr. Ayman Abdelkarim, Mr. Abdullah Mohammed, Mr. Hefni Saleh, Mr. Fadl holail, Mr. Abdul-Naser Ahmed for the production of the studied steels and their help in the refining process using ESR. Also, I would like to thank Mr. Ghazoly Sayed, Mrs. Magda Zeinhom and Mrs. Salloha Abdul-Gawad for their help.

Special thanks to my doctoral training committee Professor Timo Fabritius and Dr. Mamdouh Omran. I would like to thank the pre-examiners of this thesis, Professor Pasi Peura from Tampere University and Associate Professor Anders Tilliander from KTH for the careful review of this thesis and the suggestions for improvements.

Also, I would like to thank all my friends in Oulu specially Dr. Mamdouh Omran, Dr Amr Hamada, Dr. Khaled Abbas, Dr. Mahmoud El-khwanky and Dr. Atef Hamada for their support and help.

Finally, I would like to thank all my family, especially my wife Rehab and my sons Moaz, Malek and Yousef, my sisters Abeer and Asmaa and my brother Khaled for their love, endless support, and encouragement during my life.

Oulu, August 2020 Mohammed Ali

Abbreviations and symbols

BF	Blast furnace
BOF	Basic oxygen furnace
CCS	Carbon capture and storage
CCT	Continuous cooling transformation
CCU	Carbon capture and utilization
CO_2	Carbon dioxide
CR	Cooling rate
CVN	Charpy V-notch
DAQT	Double austenitization and quenching followed by tempering
DBTT	Ductile-brittle transition temperature
DF	Ductile fracture
DRI	Direct reduced iron
EAF	Electric arc furnace
EBSD	Electron backscatter diffraction
ECD	Equivalent circle diameter
EDAX	Energy-dispersive X-ray spectroscopy
EDS	Energy-dispersive X-ray spectroscopy
EGS	Effective grain size
El.	Elongation to fracture
EPMA	Electron probe microanalysis
ES	Eglin steel
ESR	Electroslag remelting
FESEM	Field emission scanning electron microscopy
FFT	Finish forging temperature
HRTEM	High-resolution transmission electron microscopy
I-ESR	ESR operated under protective inert gas
IF	Induction furnace
IPF	Inverse pole figure
IQ	Image quality
LSCM	Laser scanning confocal microscopy
M-A	Martensite-austenite
MTEX	Texture and crystallographic analysis toolbox
NMIs	Non-metallic inclusions
PAGS	Prior austenite grain size
RA	Retained austenite
SAD	Selected area diffraction
SAQT	Single austenitization and quenching followed by tempering

TAS	Total applied strain
TEM	Transmission electron microscopy
TIL	Total impurity level
UHSSs	Ultrahigh-strength steels
UTS	Ultimate tensile strength
VAC-ESR	ESR operated under vacuum
VAR	Vacuum arc remelting
VIM	Vacuum induction melting
XRD	X-ray diffraction
XRF	X-ray fluorescence
YS	Yield strength

A_{c1}	Ferrite to austenite transformation start temperature (°C)
A_{c3}	Ferrite to austenite transformation finish temperature (°C)
a_i	Activity of each element in the molten steel
B_f	Bainite finish transformation temperature
B_s	Bainite start transformation temperature
C_γ	The wt.% of carbon in the retained austenite
$D90\%_{GA}$	Effective grain size at 90% in the cumulative grain area distribution
$D90\%_{GN}$	Effective grain sizes at 90% in the ECD distribution
$D95\%_{ppt}$	Precipitate size at 95% in the cumulative ECD distribution
e_i^j	Interaction coefficient between solutes (i and j)
f	Volume fraction of the precipitates
f_i	Activity coefficient of the solute atom i
M_f	Martensite finish transformation temperature
M_s	Martensite start transformation temperature
V_γ	Volume fractions of retained austenite

ΔG°	Standard Gibbs free energy
ζ_i	Nominal segregation index
σ_D	Dislocation density strengthening
σ_L	Lath refinement strengthening
σ_P	Precipitation strengthening

List of original publications

This thesis is based on the following publications, which are referred to throughout the text by their Roman numerals:

I Ali, M., Eissa, M., El Faramawy, H., Porter, D., Kömi, J., El-Shahat, M. F., & Mattar, T. (2017). Electroslag refining of CrNiMoWMnV ultrahigh-strength steel. *Journal of Minerals and Materials Characterization and Engineering*, *5*(6), 385–407.

II Ali, M., Porter, D., Kömi, J., Eissa, M., El Faramawy, H., El-Shahat, M. F., & Mattar, T. (2018). Effect of electroslag refining on cleanness, microstructure and mechanical properties of a newly developed CrNiMoWMnV ultrahigh-strength steel. *Key Engineering Materials*, *786*, 10–22.

III Ali, M., Porter, D., Kömi, J., Heikkinen E.-P., Eissa, M., El Faramawy, H., & Mattar, T. (2019). The effect of electroslag remelting on the cleanliness of CrNiMoWMnV ultrahigh-strength steels. *Journal of Mining and Metallurgy, Section B: Metallurgy*, *55*, 381–395.

IV Ali, M., Porter, D., Kömi, J., Eissa, M., El Faramawy, H., & Mattar, T. (2020). The effect of electroslag remelting on the microstructure and mechanical properties of CrNiMoWMnV ultrahigh-strength steels. *Metals*, *10*(2), 262.

V Ali, M., Porter, D., Kömi, J., Eissa, M., El Faramawy, H., & Mattar, T. (2020). Characterization of the microstructure and precipitates formed during the thermomechanical processing of a CrNiMoWMnV ultrahigh-strength steel. *Steel Research International*, *91*(6),1900580.

VI Ali, M., Porter, D., Kömi, J., Eissa, M., El Faramawy, H., & Mattar, T. (2019). Effect of cooling rate and composition on microstructure and mechanical properties of ultrahigh-strength steels. *Journal of Iron and Steel Research International*, *26*, 1350–1365.

VII Ali, M., Porter, D., Kömi, J., Eissa, M., El Faramawy, H., & Mattar, T. (2019). The effect of double austenitization and quenching on the microstructure and mechanical properties of CrNiMoWMnV ultrahigh-strength steels after low-temperature tempering. *Materials Science & Engineering: A*, *763*, 138169.

Mohammed Ali has been the main corresponding author of all the publications. He has planned all experimental work started from the secondary refining using electroslag remelting, performed the laboratory refining process of all investigated steels and executed all tests and materials characterization except the following: chemical analysis of the charging materials for Paper I, and XRD and tensile test for Paper II, IV, VI and VII. Thermodynamics calculations were made by Eetu-Pekka Heikkinen for Paper III, and the Gleeble simulation for Paper V and VI has been done by Mr. Juha Uusitalo. The impact toughness test for Paper VI has been done at Lapland University of Applied Sciences with the help of Dr. Timo Kauppi. The EPMA tests have been done with the aid of the operator Mrs. Leena Palmu for

Paper II and IV, and TEM work in Paper V and VII has been done with the aid of the operator Mr. Sami Saukko. Dr. Vahid Javaheri provided the Matlab script and related texts for the prior austenite grain reconstruction in Papers VI and VII. However, Mohammed Ali modified the script using the MTEX toolbox for use in Paper V. Prof. David Porter commented on all Papers and Prof. Taha Mattar commented on Paper I.

Contents

Abstract
Tiivistelmä
Acknowledgements **9**
Abbreviations and symbols **11**
List of original publications **13**
Contents **15**
1 Introduction **17**
1.1 Aim of the research ... 19
2 Background **23**
2.1 Steelmaking and CO_2 emissions ... 23
2.2 Ultrahigh-strength steels ... 25
2.2.1 Low alloy steels ... 25
2.2.2 Secondary hardening steels ... 29
2.2.3 Maraging steels ... 29
2.2.4 Eglin steel ... 30
2.3 Strengthening and toughening of steels ... 30
2.3.1 Role of alloying elements in steel ... 30
2.3.2 Strengthening mechanisms of martensitic steel ... 34
2.3.3 Factors affecting impact toughness ... 39
2.4 Electroslag remelting ... 40
2.5 Double quenching and tempering process ... 45
3 Experimental **47**
3.1 Materials and production methods ... 47
3.2 Methods and characterization techniques ... 49
3.2.1 Characterization techniques ... 49
3.2.2 Gleeble simulation tests ... 53
3.2.3 Heat treatment ... 54
4 Results and discussion **57**
4.1 Effect of ESR on the yield of alloying elements and impurities ... 57
4.1.1 Effect of ESR on the yield of alloying elements ... 57
4.1.2 Effect of ESR on the S, P and N contents ... 65
4.2 Effect of ESR on NMIs ... 71
4.2.1 Size and frequency of NMIs ... 71
4.2.2 Chemical composition of NMIs ... 75
4.2.3 Thermodynamic calculations for NMIs ... 84

4.3 Construction of CCT diagrams 87
4.4 Microstructure characterization..... 90
4.4.1 Effect of ESR on the microstructure features, precipitates and segregations 91
4.4.2 Microstructure and precipitates variation during the forging 106
4.4.3 Microstructure changes with the variation in the chemical composition and cooling rate..... 118
4.4.4 Microstructure of UHSSs after single and double austenitization and quenching followed by tempering 126
4.5 Mechanical properties characterization..... 135
4.5.1 Effect of ESR on mechanical properties..... 135
4.5.2 Effect of chemical composition and cooling rate on mechanical properties..... 140
4.5.3 Effect of double austenitization and quenching on mechanical properties after tempering 146
5 Summary and conclusions 149
5.1 Influence of electroslag remelting on the yield of alloying elements, cleanliness, microstructure and mechanical properties of the investigated CrNiMoWMnV ultrahigh-strength steels 149
5.2 Effect of cooling rate and composition on the microstructure and mechanical properties of ultrahigh-strength steels..... 151
5.3 The effect of double austenitization and quenching on the microstructure and mechanical properties of CrNiMoWMnV ultrahigh-strength steels after low-temperature tempering..... 152
6 Novel features 155
7 Recommendation for further research 157
List of references 159
Original publications 175

1 Introduction

Steel industry is one of the most important industries in the world and the production has increased continuously. The annual global production of crude steel is 1808 million tonnes in 2018 compared to 1730 million tonnes in 2017. In most of this production, nearly 70.8% is produced using an ore-based production route, which includes blast furnace (BF) and basic oxygen furnace (BOF) [1]. This increase in the production is associated with an increase in the CO_2 emissions as a result of an increase in the reducing agents, i.e. for example, coke, coal, oil, and natural gas in the BF. About 2.1 tonnes of CO_2 emissions are emitted per one tonne of produced crude steel [2].

According to the European Council in 2009, CO_2 emissions should be decreased from about 80 to 95% of 1990 levels by 2050. In order to reduce CO_2 emissions, steel industries in different parts of the world are involved in different on-going projects such as hydrogen as a reducing agent, carbon capture and storage (CCS), carbon capture and utilization (CCU), biomass as a reducing agent and electrolysis, as it reduces iron ore using electricity [3]. One of the possibilities to decrease CO_2 emissions is to have an additional shift from the ore-based production route to a scrap-based production route to increase its share, for example, in Europe from 41% to 44% of the total crude steel production. However, this depends mainly on the availability and quality of the scrap, which limits the steel qualities that could be obtained via the scrap-based production route [4].

On the other hand, recently, there have been increasing demands for more economical, high-performance, ultrahigh-strength steels (UHSSs) with high impact toughness for use in advanced engineering applications as a replacement for the highly alloyed high-cost steels such as AF-1410, Aermet-100 and HP9-4-30. Recently, Eglin steel was developed by Dilmore and Ruhlman [5], and it is a medium carbon low-alloy steel containing moderate levels of Mn, Si, Cr, Ni, W, V, and Mo and that gives a good strength and toughness combination.

The current work was undertaken to extend the studies of Dilmore and Ruhlman [5] by studying the possibilities to develop ultrahigh-strength high-impact toughness steel with even lower production cost via steel recycling through air-induction melting followed by secondary refining using electroslag remelting (ESR) which is applied to the produced low-purity UHSSs which contain high levels of impurities (total impurity level (TIL), % = O + S + P + N) compared to those produced via vacuum induction melting.

ESR is a low-cost secondary refining process used to provide high-quality steel and improve the mechanical properties, such as impact toughness, ductility and corrosion resistance, through its effect on the total impurities level and non-metallic inclusions (NMIs) content [6]–[8]. However, in the last decades, there have been many studies about the effect of ESR on different steel compositions that reveal controversies concerning the effect of ESR. Using the same slag as that used in our study as well as other slags, Hossam et al. [9] studied the effect of ESR on the tensile properties of various maraging steels. They showed that ESR produced a significant increase in the yield strength (YS), ultimate tensile strength (UTS) and elongation to fracture (El.%) in some steels but a sharp decrease in others. Unfortunately, they only mentioned the beneficial effects of ESR in their conclusion and failed to mention the fact that the effects can also be detrimental. In another publication, Pribulová et al. [10] studied the effect of various ESR slags on various steels. They, too, showed that ESR produced a small improvement in YS, UTS and El.% for some steels but a slight decrease in YS for other steels. Maity et al. [11] investigated the effect of inoculating with Ti and Nb during the ESR and showed that the yield strength is improved without any change in the ductility and impact toughness. However, in another study, Maity et al. [12] concluded that inoculation with titanium in the presence of nickel produces no improvement in strength or toughness.

In martensitic steels, refining the prior austenite grain, packet and block sizes improves the yield strength [13]–[15], impact toughness and ductile-brittle transition temperature (DBTT) [16], [17]. Kennett et al. [18] concluded that in microalloyed ASTM A514 steel, refinement of the prior austenite grain size (PAGS) can improve the strength and toughness simultaneously after quenching and low-temperature tempering. Also, strength can be improved via formation of fine precipitates during low-temperature tempering. But the precipitates become detrimental to the toughness if they are formed on the prior austenite grains and the martensitic lath boundaries [19], [20].

Double quenching and tempering was used to enhance the strength and toughness properties of steel simultaneously. In this treatment, the first austenitization is performed at high temperatures to dissolve the coarse carbides which are detrimental to the toughness of steel. However, this leads to an increase in the size of the austenite grains, which is harmful to the toughness of steel. So, the second low-temperature austenitization is performed to provide finer austenite grains [21]. Based on the previous studies [22]–[26], the influence of double austenitization and quenching on mechanical properties depends on the steel

composition because of the variation in the response of the microstructure features, i.e. carbide and grain sizes distributions.

So, there are different research gaps to be filled based on the aim of an additional shift from an ore-based production route to a scrap-based production route to reduce the CO_2 emissions, and find more economical, high-performance, UHSSs with high impact toughness for use in advanced engineering applications as replacements for the highly alloyed high-cost steels.

Six low-purity Eglin UHSSs were chosen for detailed study as an extension of the Eglin steel research mentioned above. The studied steels' compositions were designed to contain low to medium C (0.1 to 0.3 wt.%), Cr (1.6 to 3.5 wt.%), Ni (1.0 to 4.4 wt.%), Mo (0.3 to 0.5 wt.%), W (1.1 to 1.8 wt.%), Mn (0.3 to 0.7 wt.%), Si (0.7 to 0.9 wt.%), V (0.05 to 0.09 wt.%), Ti (0.001 to 0.003 wt.%), Nb (0.001 to 0.002 wt.%), Cu (0.01 to 0.02 wt.%) and Al (< 0.1 wt.%).

1.1 Aim of the research

Many different questions have been raised before and during this work which increased the motivation to go through this work and complete this thesis. The main research questions are listed below:

- Is it possible to get low-cost, low-alloy UHSS with high impact toughness from steel scrap using the proposed production route mentioned above?
- Does ESR lead to the removal of all NMIs in the consumable electrode and the formation of new NMIs in the remelted ingot? What are the changes in the NMIs' characteristics, i.e. chemical composition, number density, and size, as a result of ESR?
- For a given steel composition, is it possible to predict the chemical composition and quantity of the NMIs present with and without ESR using the thermodynamic software FactSage?
- Is there an effect of ESR on the microstructural features such as the prior austenite grain size, effective high-angle grain size and lath size, and the number and size of precipitates?
- Are the commercial software packages JMatPro, Thermo-Calc and IDS able to predict the effect of ESR on the microstructure given the composition of the steel without and with ESR?
- Is there any effect of ESR on the mechanical properties before any heat treatment?

- What is the effect of forging parameters on the microstructure and precipitation of these UHSSs?
- What is the effect of the cooling rates and composition on the microstructure and the mechanical properties of the as-cooled and untempered condition of these UHSSs?
- At slow cooling rate, which microstructure leads to the best combination of strength and toughness: a 100% martensite or bainite with proeutectoid carbides?
- Is there any improvement in the mechanical properties that can be gained from using the double austenitization and quenching heat treatment in the case of these UHSSs?

In order to answer these questions, the current work is divided into four stages. The main idea in the *first stage* is using a different combination of low-cost alloying elements to get the best combination between strength and toughness and using induction furnace (IF) and ladle treatment as a low-cost melting process, and also using IF and ladle treatment followed by ESR to enhance the quality of the produced steel.

The main idea in the *second stage* is a comparison of the forged bars of the ingots produced via simple air induction melting with those that have also been processed with ESR. The comparison will be based on materials characterizations that include the chemical composition, microstructure, and NMI content and, in addition, mechanical properties which are compared and related to the microstructure and chemical composition. Paper I, II, III and IV focus on this stage.

In the *third stage* to determine the optimum heat treatment cycles, the continuous cooling transformation (CCT) diagrams of selected steels from the investigated UHSSs will be determined dilatometrically using a Gleeble thermomechanical simulator in addition, to study the effect of cooling rate (CR) and composition on the mechanical properties of selected steels from the investigated UHSSs in the as-cooled and untempered condition. Also, the effect of total applied strain (TAS) and finish forging temperature (FFT) on the microstructure and precipitation kinetics has been investigated. Paper V and VI focus on this stage.

The main idea at the *fourth stage* is to obtain an optimum combination of strength and toughness using different heat treatment cycles like single and double quenching and tempering to obtain optimum microstructures with small grain,

packet, block and lath sizes, and finely distributed carbides. Paper VII focuses on this stage.

Paper I discusses the effect of the ESR on the yield of valuable alloying elements, together with S and P removal and the possibility of N removal from the investigated UHSSs when using CaF_2-based slag containing by weight about 70% CaF_2, 15% Al_2O_3 and 15% CaO. Also, it studies the relationship between elemental activities and their effect on yield of the alloying elements and impurities in the molten state.

Paper II investigates the influence of ESR for one steel composition in the as-forged and air-cooled state, considering cleanliness, microsegregation, microstructure and mechanical properties. Microstructural parameters covered included the morphologies of martensite, PAGS, grain sizes and grain boundary misorientations, and the number density and size of precipitates.

Paper III gives high quality images using the modern image acquisition tools and detailed descriptions of the counts, sizes, shapes, and chemical compositions of the NMIs, which is not given elsewhere in forged bars from the same steel produced without and with ESR. Also, it discusses the chemical changes in the NMIs and the secondary NMIs formed during ESR. Also, thermodynamic calculations for the predicted NMIs are included.

Paper IV provides a detailed description of the microstructure features of the selected UHSSs, which includes the phases formed; PAGS, high-angle grains and laths; number and size of precipitates; and the level of micro-segregation. This information is used to illustrate the influence of ESR on the mechanical properties of selected UHSSs.

Paper V evaluates the influence of the hot forging parameters, i.e. TAS and FFT, on the final overall microstructure features, including the phase formed, PAGS, effective grain sizes and grain boundary misorientations and, in addition, the morphology, chemical composition, crystallography, number density and size of precipitates.

Paper VI studies the phase transformations of two selected UHSSs with different chemical compositions. In addition, it investigates the influence of composition and CR on the microstructure and mechanical properties.

Paper VII provides a detailed description of the steel microstructures, which includes the phases formed; PAGS, high-angle grains and laths; and the number, size and chemical composition of precipitates. The information is used to explain the observed effects of the double austenitization treatment on the mechanical properties of selected steels from the investigated UHSSs.

2 Background

2.1 Steelmaking and CO_2 emissions

Nowadays, steel is produced using two main production routes (see Fig. 1): the ore-based production route, which emits about 2.1 tonnes of CO_2 emissions per tonne of crude steel, and the scrap-based production route, which emits 0.6 tonnes of CO_2 emissions per tonne of crude steel [27]. The ore-based production route is based on BF and BOF and uses different raw materials, such as iron ore, metallurgical coal, limestone, and recycled steel (representing about 30% of the total charge materials). The scrap-based production route is based on the electric arc furnace (EAF) and uses recycled steels (up to 100% of the total charge materials) and direct reduced iron (DRI) or hot metal, and electricity. In 2018, about 71.2% (about 1286 million tonnes) of the total world steel production is produced by the ore-based production route and 28.8% (520 million tonnes) is produced by the scrap-based production route [1].

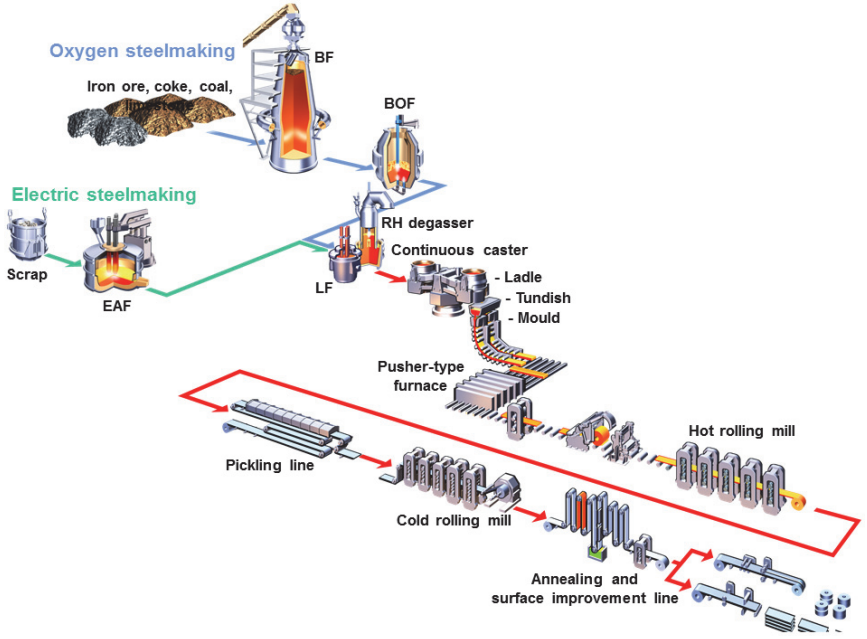

Fig. 1. Steel production routes (Reprinted by permission from [28] © 2018 Authors, and Associazione Italiana Di Metallurgia).

The CO_2 emissions in iron and steel making represent about 7–9% of total world CO_2 emissions [29] and the continuous increase in the production of steel (see Fig. 2) will increase the CO_2 emissions and increase the problem of global warming and climate change. So, nowadays, the reduction of the CO_2 emissions is the most significant challenge and the top priority for all steel companies in order to fulfill the objective of the Paris climate agreement of reducing the CO_2 emissions by 80% to 95% compared to 1990 levels.

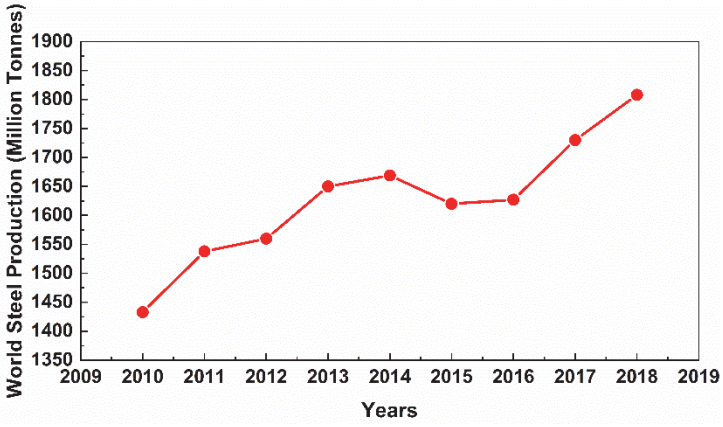

Fig. 2. World crude steel production from 2010 to 2018 (Reprinted by permission from [1] © 2019 World Steel Association).

To reach the objective of the Paris climate agreement, different promising research projects are ongoing in different places in the world to develop alternatives and new technologies to be used instead of the currently used technologies. These projects can be divided into five categories. The first category is *Hydrogen as a reducing agent*, in which using carbon is avoided and hydrogen is used for the reduction process of the iron ores, which leads to forming water (H_2O) instead of CO_2. The second category is *Biomass as a reducing agent*, which is targeted to use biomass such as charcoal instead of coal. The third category is *Electrolysis*, which is targeted to reduce the iron ore using electricity instead of carbon. The fourth category is *CCS*, which is targeted to produce a clean and concentrated stream of CO_2 that can be captured and stored. The fifth category is *CCU*, which is targeted to use the components of the co-product gases from existing processes to produce fuels or input material for the chemical industry [30].

Increasing the share of crude steel production using the scrap-based production route can be considered one of the possibilities to reduce the CO_2 emissions [31]. For example, Germany is considered the first producer of crude steel in Europe by 42.4 million tonnes in 2018, with a share of about 25.3% of the total production of crude steel in Europe [32]. It was observed that production of 12.6 million tonnes of crude steel from the scrap using the scrap-based production route led to reducing the CO_2 emissions by 17 million tonnes annually in Germany [33].

2.2 Ultrahigh-strength steels

The definition of structural UHSSs depends mainly on the field of applications. Philip [34] defines UHSSs as those steels with yield strength exceeding 1380 MPa, but recently they have been defined as those steels with yield strength of 900 MPa or more [35]. Ultrahigh-strength tough steels are used in many engineering applications, i.e. pressure vessels; automotive, locomotive and truck components; aircraft undercarriage parts; and rocket motor cases, missile bodies and offshore platforms. UHSSs include many categories of steels, but in this section only four categories of UHSSs will be discussed: i) low alloy steels typified by AISI 4340, ii) secondary hardening steels typified by AF1410, and iii) maraging steels typified by 18Ni(250) [36]–[39], and iv) Eglin steel. The chemical composition and mechanical properties of selected grades of UHSSs are given in Table 1 and Table 2, respectively. These steels have a dislocated martensitic structure with fine dispersed carbides obtained by different heat treatments. There are many differences between these categories of steels, mainly in the size and shape of martensite, carbon content in solid solution, the volume fraction of retained austenite, the type of the fine formed precipitates after tempering or aging and the types of NMIs and their volume fractions [37], [40], [41].

2.2.1 Low alloy steels

These steels contain a medium carbon level range from 0.30-0.50 wt.% and are hardened through conversion of austenite to martensite via austenitization and quenching, followed by tempering. The hardness, strength and toughness varied significantly based on the composition, section thickness, quenching media and tempering temperature [39]. The microstructure formed in ultrahigh-strength low-alloy steel consists mainly of a fine lath martensitic structure with high dislocation density and strengthened by the formation of transition carbides, such as ε-carbides

($Fe_{2.4}C$) and η-carbides (Fe_2C), at the early stage of tempering at temperature up to 250 °C (stage I).

At intermediate tempering temperatures (stage II; 250–400 °C), the fine retained austenite (RA) formed between the martensitic laths starts to transform to carbides, which subsequently causes temper martensite embrittlement in addition to decreasing the strength, while tempering at (stage III; 250–700 °C) leads to increasing the toughness at the expense of strength, as a result of transformation of the RA and transition carbides into a mixture of ferrite and cementite. So, in order to get a good balance between the strength and toughness in this category, the tempering should be limited on stage I [36], [42]. However, these steels cannot be used in the form of quenched-tempered at yield strength level higher than 1378 MPa, due to the lower level of toughness at these high levels of strength [38].

The chemical composition of all steels included in this category is based on the modification of 4340 steel. For example, 300M is basically 4340 steel modified by adding about 1.45-1.80 wt.% of Si, which increases the possibility for tempering 300M at a little higher temperature (250–300 °C) without deteriorating the strength and toughness properties [40].

Table 1. Chemical compositions of selected ultrahigh-strength steels [36]–[39].

Alloy	C	Mn	Si	Cr	Ni	Mo	V	Co	W	Ti	Al
Low alloy steels											
4340	0.38-0.43	0.60-0.80	0.15-0.30	0.70-0.90	1.65-2.00	0.20-0.30	-	-	-	-	-
300M	0.38-0.46	0.60-0.90	1.45-1.80	0.70-0.95	1.65-2.00	0.30-0.65	0.05 min	-	-	-	-
Secondary hardening steels											
AF1410	0.13-0.17	0.10 max	0.10 max	1.80-2.20	9.50-10.50	0.90-1.10	-	13.50-14.50	-	-	-
AerMet 100	0.21-0.25	0.10 max	0.10 max	2.90-3.30	11.00-12.00	1.10-1.30	-	13.00-14.00	-	-	-
HP 9-4-30	0.29-0.34	0.10-0.35	0.20 max	0.90-1.10	7.00-8.00	0.90-1.10	0.06-0.12	4.25-4.75	-	-	-
Maraging steels											
18Ni(250)	0.03 max	0.12 max	0.12 max	-	17.00-19.00	4.60-5.10	-	7.00-8.50	-	0.30-0.50	0.05-0.15
18Ni(300)	0.03 max	0.12 max	0.12 max	-	18.00-19.00	4.60-5.20	-	8.00-9.50	-	0.50-0.80	0.05-0.15
18Ni(350)	0.01 max	0.10 max	0.10 max	-	17.00-18.00	3.50-4.00	-	12.00-13.00	-	1.60-2.00	0.10-0.20
Recently developed steel											
Eglin steel	0.16-0.35	0.85 max	1.25 max	1.50-3.25	5.00 max	0.55 max	0.05-0.30	-	0.70-3.25	-	0.05 max

Table 2. Mechanical properties of selected ultrahigh-strength steels [5], [34], [36], [39], [43].

Alloy	Heat treatment	UTS [MPa]	YS [MPa]	El. [%]	Hardness [HV]	Impact toughness at RT (at -40°C) [J]
Low alloy steels						
4340	845 °C, oil quenched, tempered at 205 °C	1980	1860	11	567	20
300M	860 °C, oil quenched, tempered at 205 °C	2140	1650	7	589	21
Secondary hardening steels						

Alloy	Heat treatment	UTS [MPa]	YS [MPa]	El. [%]	Hardness [HV]	Impact toughness at RT (at -40°C) [J]
AF1410	675 °C, air cooled, 900 °C, oil quenched, 830 °C, oil quenched, refrigerated at -73 °C, 510 °C, air cooled	1750	1545	16	-	65
AerMet 100	885 °C, air cooling, refrigerated at -73 °C, aged at 482 °C	1965	1724	13-14	567-589	40
HP 9-4-30	845 °C, oil quenched, refrigerated to -73 °C, double tempered at 205 °C	1650-1790	1380-1450	8-12	497-567	20-27
Maraging steels						
18Ni(250)	815 °C, air cooled, aged at 482 °C for 3h	1792	1703	8	490-505	24-45
18Ni(300)	815 °C, air cooled, aged at 482 °C for 3h	2048	2000	7	531-649	16-26
18Ni(350)	815 °C, air cooling, aged at 482 °C for 12h	2468	2448	6	-	-
Recently developed steel						
Eglin steel (ES-1)	950 °C, air cooled, 927 °C, oil quenched, 260 °C, air cooled	1700	1337	18	448	76 (58)
Eglin steel (ES-2)	950 °C, air cooled, 927 °C, helium or nitrogen gas quenched, 260 °C, air cooled	1685	1392	18	458	37 (27)
Eglin steel (ES-3)	950 °C, air cooled, 927 °C, still air quenched to 538 °C then oil quenched, 260 °C, air cooled	1611	1285	18	448	61 (29)
Eglin steel (ES-4)	950 °C, air cooled, 927 °C, simulating air-cooling using helium or nitrogen to 538 °C, then quenched in helium or nitrogen, 260 °C, air cooled	1712	1373	18	458	54 (33)
Eglin steel (ES-5)	950 °C, air cooled, 927 °C, still air quenched to 538 °C then water quenched, 260 °C, air cooled	1863	1489	17	490	36 (30)

Most of these steels are produced via air melting and to enhance the cleanliness, obtain less variation in the properties from heat to heat, and obtain high quality products with greater ductility and toughness, it is followed by various advanced melting techniques such as vacuum degassing, ESR, vacuum arc remelting (VAR) and double vacuum melting practice (vacuum induction melting followed by vacuum arc remelting [VIM-VAR]) [39], [44]. Most of these steels are fabricated by forging. Table 2 provides the mechanical properties of some selected ultrahigh strength low alloy steels.

2.2.2 Secondary hardening steels

This category of steels (Ni-Co-Fe alloy) have a lower level of carbon compared to the low alloy steel category. This contributes to the high ductility and toughness of these steels. The high nickel contents gives high hardenability and toughness while the high level of Co eliminates the RA and increases the driving force for carbide precipitation, and delays the dislocation recovery, which enhances the precipitation kinetics and increases the numbers of precipitates [37], [40], [41]. These steels are hardened through conversion of austenite to martensite via austenitization and quenching followed by tempering. During the tempering, fine-dispersed stable alloy carbides are formed, leading to increasing the hardenability, and this process, called secondary hardening effect and increases the strength via precipitation strengthening. These steels are produced by vacuum melting (VIM+VAR) in order to obtain high toughness [36], [39]. The mechanical properties of selected secondary hardening steels are given in Table 2.

2.2.3 Maraging steels

Maraging steels [36], [38], [39], [41], [45]–[48] have a low level of carbon, which acts as impurity in these steels, and a high level of Ni depresses the martensite start temperature M_s to lower than 150 °C, which allows forming a martensitic structure from the austenitization temperature on air cooling even in heavy sections. However, the strength of the formed martensite after air cooling is not like the strength of those formed in high-carbon alloy steels. This category of steels is strengthened by precipitation hardening via age hardening at about 450–510 °C to form fine precipitates of intermetallic compounds, i.e. Ni_3Mo, Ni_3Ti and the Laves phase (Fe_2Mo) with the aid of substitutional elements and the presence of high dislocation density imparted to the martensitic structure. The presence of Co

reduces the solubility of Mo in the matrix, thereby providing more Mo to form Mo rich precipitates. Precipitates formed in maraging steels are finer than those transition carbide precipitates formed by tempering in low alloy steels. Maraging steels are characterized by a good combination of high hardenability, high strength, high ductility, excellent toughness, and good weldability. Maraging steels are produced by air melting followed by VAR or VIM followed by VAR. However, for aerospace application, the steels are produced by a triple melting process, air melting, VIM and VAR in order to decease the residual elements, i.e. C, Mn, S and P and gases, i.e. O, N and H, which can deteriorate the properties of these steels. Usually, maraging steels are fabricated using rolling or forging. The mechanical properties of selected maraging steels are given in Table 2.

2.2.4 Eglin steel

Eglin steel [5], [49]–[52] is an UHSS that was recently developed at Eglin Air Force Base in the early 2000s, and it was patented in 2009. Eglin steel was developed as a replacement to the high-cost high-alloyed UHSSs, i.e. AerMet100, HP 9-4-30, and AF 1410, which contain a high percentage of the high cost alloying elements Co and Ni. The microstructure of Eglin steel consists mainly of martensitic structure with intra-lath ε-carbides in addition to M_3C, M_6C and MC carbides which are obtained after quenching and tempering at stage I. To get a high quality of this steel, it is produced by vacuum melting and remelting practices. Eglin steel can be fabricated by die forging, close die forging, solid or hollow extrusion methods, static or centrifugal castings, continuous casting, plate rolling, bar rolling or other conventional methods. Typical mechanical properties of Eglin steel with different elemental composition and heat treatment are given in Table 2.

2.3 Strengthening and toughening of steels

The strength and toughness of steel are governed by different parameters. Some of these parameters will be discussed in this section.

2.3.1 Role of alloying elements in steel

Based on the influence of alloying elements on the matrix, there are two groups of alloying elements: i) austenite stabilizer, i.e. Ni, Co, Mn, Cu, C, and N, and ii) ferrite stabilizer, i.e. Si, Cr, W, Mo, P, Al, Sn, Sb, As, Zr, Nb, B, S, and Ce. While

based on the interaction of the alloying elements with carbon, the alloying elements are divided into two groups: i) carbide forming elements, i.e. Mn, Cr, Mo, W, V, Nb, Ti, and Zr, and ii) non-carbide forming elements, i.e. Ni, Co, Cu, Si, P, and Al [53].

However, different alloying elements and impurities in steel, combined with the parameters of an applied thermomechanical and heat treatment process, can give large variation in the microstructure and mechanical properties of steel.

The chemical composition of proposed UHSSs in the current work is designed based on variable alloying elements, as mentioned above, to achieve the targeted mechanical properties after heat treatment. Roles of different alloying elements used in proposed UHSSs are illustrated below.

Carbon (C)

Carbon is a strong austenite former and used as a strengthener in steel. However, it is not recommended to use it in a high percentage as a strengthener because it has a detrimental effect on the weldability and toughness of steel [54]. Increasing the C content leads to increased DBTT. C enhances the hardenability and strength of the steel through different mechanisms: i) phase transformation strengthening by shifting the transformation of martensite and bainite to start at lower temperatures, ii) solid solution strengthening, and iii) carbide precipitation strengthening [38], [53], [54].

Usually, precipitation strengthening reduces the toughness, unless there is another mechanism, i.e. microstructure refinement is used at the same time, leading to increasing the strength without decreasing the toughness of the steel [54]. For UHSSs, C is used in the range of 0.15 to 0.45 wt.%, but the concentration depends on the required combined level of strength, hardenability, ductility and toughness [37].

Silicon (Si)

Silicon is used as a primary deoxidizer in the steel industry. Si is an effective solid solution strengthener, ferrite stabilizer and non-carbide forming element that dissolves in the matrixes of austenite, ferrite or martensite [38], [53]. Up to 1 wt.% of Si is used in UHSSs to achieve high toughness, and high and deep hardenability, and prevent the temper embrittlement of steel during the low temperature tempering (150–300 °C). This is because of the limited solubility of Si in the cementite (Fe_3C),

which causes the nucleation and growth of Fe_3C to be sluggish at low tempering temperatures [34], [39], [55]. Si leads to increasing the stability of austenite at high tempering temperatures. Si dissolves in martensite and causes the decomposition of martensite to be sluggish at low temperature tempering, i.e. 300 °C [38], [53].

Manganese (Mn)

Manganese is commonly used in the steel industry as a deoxidizer and desulfurizer. In most practical situations, Mn is added to react with SiO_2 forms a complex manganese silicate ($MnO.SiO_2$), which has a very low melting temperature that is desirable for subsequent formability. The formation of $MnO.SiO_2$ reduces the activity of silica in the oxide phase, shifting equilibrium and leading to much lower residual oxygen in the steel [56].

Mn is a solid solution strengthener, austenite stabilizer and a weak carbide forming element; however, it can dissolve only in cementite [53], [54]. Mn can increase the strength of the ferrite matrix, thereby improving the hardenability. The presence of manganese enhances the hardness of the tempered martensite via inhibiting the carbide coalescence and minimizing the ferrite grain coarsening. The lower level of Mn (<2 wt.%) leads to improving the tensile strength of cast steels [38].

Chromium (Cr)

Chromium is used to enhance strength and hardenability through transformation strengthening and, when it is combined with C, it is a powerful hardening alloying element. Also, it increases corrosion resistance. Cr is a strong ferrite stabilizing element and a medium carbide forming element and behaves like Mo, and it can retard the softening of martensite at high temperatures [38].

Nickel (Ni)

Nickel is a strong austenite and non-carbide former. Ni can enhance hardenability, strength, and toughness simultaneously. This behavior can be illustrated by the ability of Ni to produce high stable austenite which is favorable to toughness, while the hardenability and strength improved by solid solution strengthening. In addition, the solid solution strengthening of Ni is high at room temperatures and it is reduced by decreasing the temperature, which may lead to enhancing the impact toughness

at lower temperatures. The combination of Ni, Cr and Mo can provide excellent hardenability, impact toughness, and fatigue resistance in steels [38], [39], [54].

Molybdenum (Mo)

Molybdenum is a solid solution strengthener and considered one of the strongest carbides forming elements that can provide secondary hardening during tempering of quenched steels. Mo enhances the strength at high temperatures and delays the temper embrittlement of some alloyed steels [37], [39], [57]. Mo can improve the hardenability of steel through promoting the formation of martensite or bainite, or a mixture between martensite and bainite, which gives good combinations between strength and toughness [54].

Tungsten (W)

Tungsten is one of the strongest carbides forming elements and behaves in steel like Mo. Due to the M_2C stoichiometry of W rich carbides, the addition of a small amount of W provides finer and higher volume fraction of carbides compared to the other carbides forming elements at the same content of carbon. Tungsten provides secondary hardening during the tempering of quenched steel. The addition of W provides high hardness, strength and wear resistance at high temperatures [37], [38], [53].

Vanadium (V)

Vanadium is a strong carbide former. V forms fine V(C,N) precipitates at lower temperatures compared to Ti and Nb carbonitrides [57]. V is a grain refiner and it can enhance the strength and impact toughness properties of steel simultaneously. Also, it leads to an increase in the hardenability of steel via its high dissolution in the austenite phase, but the undissolved vanadium carbides decrease hardenability. After controlled rolling and cooling, the presence of fine dispersed vanadium carbides provides a great dispersion hardening. Vanadium can provide high secondary hardening during tempering and improve the wear resistance and strength at high temperature [39], [53].

Titanium (Ti)

Titanium is a strong carbide and nitride forming element. Titanium carbides and nitrides are more stable than those produced by V or Nb. The fine TiN precipitates react as a grain refiner at high temperatures due to its high stability in austenite at high temperatures [53]. But the formation of large TiN precipitates deteriorates the impact toughness of steel because it acts as a crack initiation site [57].

Niobium (Nb)

Niobium is widely used as a microalloying element to obtain a good combination of strength and toughness via controlled rolling and cooling practices. Niobium is a strong carbide and nitride former, and a small addition of Nb leads to forming fine nitride or carbonitrides which can refine the PAGS significantly during soaking of the slab. At high temperatures, Nb retards the recrystallization as a result of the solute drag effect on the grain boundaries, while at low temperatures it can inhibit the recrystallization as a result of the formation of Nb(CN) via strain induced precipitation. The free Nb in the matrix retards the phase transformation to lower temperatures, which increases the transformation hardening and toughening effect [54].

Aluminium (Al)

Aluminium is commonly used as a deoxidizer in steel and most of it combines with the free dissolved nitrogen to form AlN. Compared to TiN, the solubility temperature of AlN in austenite is a little high but still has the ability to control the grain growth through the pinning effect [58]–[61].

2.3.2 Strengthening mechanisms of martensitic steel

There are various strengthening mechanisms in martensitic steels which have been discussed over decades; however, there is no clear agreement on the main controlling strengthening mechanisms. Generally, the strengthening mechanisms are related to the interaction between the dislocations with various obstacles, such as solute atoms, precipitates, grain boundaries, or other dislocations [62]. In this section, only four different strengthening mechanisms are discussed briefly, which

include solid solution strengthening, grain size strengthening, dislocation strengthening and precipitation strengthening.

Solid solution strengthening

This mechanism is governed by the alloying elements introduced either in the substitutional or in the interstitial sites. The created strain field around the solute atoms interacts with the stress field of the dislocations which subsequently impede the dislocation motion. There are two types of strain fields: i) symmetric strain field around the substitutional elements, i.e. Cr, Ni, Si, Mn, and W depending on the size difference between the solute and solvent atoms, and ii) non-symmetric strain field around interstitial atoms, i.e. C and N. The first type interacts with the stress field of an edge dislocation only while the second type is interacting with the stress field of edge and screw dislocation which increase the strength significantly. The major contribution to the strength of the martensite came from interstitial solid solution strengthening as the tetragonality of the martensite is caused by the presence of carbon atoms in the octahedral interstitial sites [47], [54], [62], [63]. The yield strength of low carbon and low alloy martensitic steels can be calculated using equation

$$\sigma_{0.2}(\mathrm{MPa}) = 413 + 1.72 \text{ x } 10^3 \ (\mathrm{wt.\%\ C})^{1/2}. \qquad (1)$$

However, with increasing the carbon content, the dislocation density increased together with the substitutional solid solution strengthening, and the packet size is consider the main controlling factor of the yield strength rather than the solid solution strengthening by carbon [64].

Grain size strengthening

The microstructure of martensitic steels is subdivided into the following units: prior austenite grains, packets, blocks, sub-blocks, and laths, with unit size decreasing from left to right (see Fig. 3). The prior austenite grains are divided into packets which consist of blocks of laths with the same habit plane. These blocks contain sub-blocks in which the laths have similar crystal orientations. The boundaries between packets and blocks have high-angle misorientations while the boundaries between sub-blocks and laths have low-angle misorientations [18], [65], [66].

There are many controversies about the definition of the effective grain size (EGS), which is defined sometimes in terms of PAGS, martensite packet size or

martensite block size, and those are considered high-angle grain boundaries with misorientation more than 15°. However, there is a direct relationship between the PAGS and the martensite packet and block sizes. Blocks are considered the smallest microstructural unit in lath martensite with high-angle grain boundaries [67].

The relationship between the effective grain size and the yield strength of the martensitic steels can be expressed by the Hall-Petch relationship [67]:

$$\sigma_y = \sigma_0 + k_y d^{-1}, \quad (2)$$

where σ_y is the yield strength, σ_0 is the fitting constant that is not influenced by the effective grain size and it is the summation of friction stress of the iron lattice, solid solution strengthening, dislocation strengthening, and precipitation strengthening, k_y is the Hall-Petch coefficient which is related to the ability of the boundary to strengthen the steel, and d is the mean EGS.

The Hall-Petch relationship is based on the stress intensifications arising at the head of a pile up of dislocations. The first dislocation arrives at the grain boundary and faces resistance from the grain boundary and arrests this dislocation due to the discontinuity of both slip plane and slip direction. Further dislocation arrives and the elastic interaction between successive dislocations, induced by the increasing applied stress, forces the first dislocation closer to the boundary and enhances the elastic strain and stress in the neighboring grain. The stress at the head of the pile-up is dependent upon the number of dislocations in the pile-up, and the number increases as the grain size is increased [60].

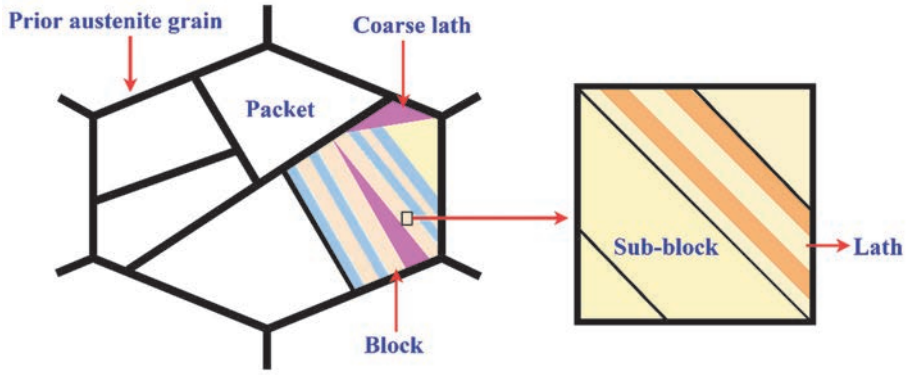

Fig. 3. Schematic structure of as-quenched lath martensite (Redrawn from [65], [68]).

Dislocation strengthening

The relationship between the dislocation density and the increment in the yield strength can be described by equation [54]

$$\Delta\sigma = \beta G b \sqrt{\rho}, \tag{3}$$

where $\Delta\sigma$ is the increase in the yield strength, β is a constant, G is shear modulus, b is burgers vector and ρ is the dislocation density.

The relationship between the dislocation density and the carbon content is well established, as increasing the carbon content leads to increasing the dislocation density. Morito et al. [69] studied the effect of carbon content in the range of 0.0026 to 0.61 wt.% on the dislocation density of Fe-C alloys and they concluded that the dislocation density increases with increasing the carbon content in the lath martensite. The dislocation density in m^{-2} can be calculated in terms of carbon content by equation [69]–[71]

$$\rho \text{ x } 10^{-15} = 0.7 + 3.5 \text{ wt.\% C.} \tag{4}$$

Takaki et al. [72] examined the strengthening mechanisms for Fe-18Ni lath martensite and concluded that the yield strength depends mainly on the dislocation strengthening, which depends on refinement of the PAGS, packets and block width.

Precipitation strengthening

Precipitation strengthening works by impeding the movement of dislocation by the dispersed precipitates. The degree of strengthening depends on several factors, i.e. the nature of the interactions between the precipitates and the dislocations, and the volume fraction and the size of the precipitates. [54], [60].

There are three different mechanisms that can explain precipitation strengthening: i) coherency strengthening, which is related to the coherency strains developed in the matrix around a coherent precipitate, ii) dispersion hardening, which arises from the looping of the dislocations between the undeformable particles, and iii) chemical hardening, which arises from the development of antiphase boundaries when a dislocation cuts through a particle [54], [60].

In the case of undeformable precipitates [60], [73], [74], dislocations bypass the precipitates by Orowan looping, or cross-slip as illustrated in Fig. 4. Under these circumstances, the bypassing operation only depends on the interparticle spacing and size of the precipitates. These strengthening effects are termed

dispersion hardening. The contribution to the total yield strength from dispersion hardening increases with increasing precipitate volume fraction and decreasing precipitate size, and is given by the Ashby-Orowan equation

$$\Delta\sigma_y\ (MPa) = \left(\frac{10.8f^{1/2}}{X}\right)(\ln(x/6.125\ \times 10^{-4})), \tag{5}$$

where f is the volume fraction of the precipitates and x is the average precipitate diameter in μm.

In the case of deformable precipitates [60], [73], [74], under stress they can be sheared such that dislocations pass through the precipitates creating antiphase boundaries, as shown in Fig. 5, and thereby raising the energy of the system. This strengthening effect is termed chemical hardening and can be given by equation [74]

$$\tau = \left(\frac{\gamma_{apb}}{2b}\right)\left[\left(\frac{4\gamma_{apb}\, rf}{\pi T}\right)^{1/2} - f\right], \tag{6}$$

where γ_{apb} is anti-phase boundary energy, b is burgers vector, r is radius of curvature to which the dislocation is bent, which is related to the particle spacing, T is the dislocation line tension, f is the volume fraction of the precipitates.

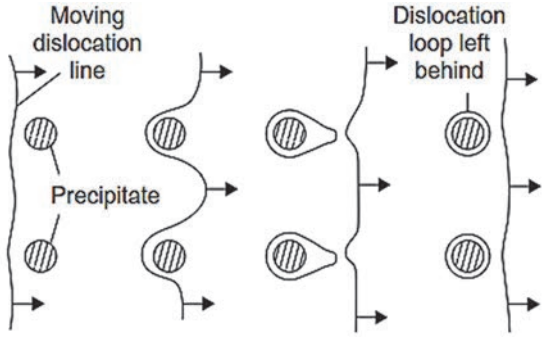

Fig. 4. Schematic illustration of a dislocation passing between widely spaced hard-undeformed precipitates (Orowan looping) (Reprinted by permission from [74] © 2014 Elsevier).

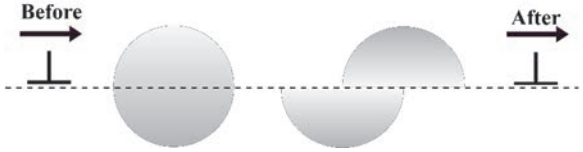

Fig. 5. Particle shearing as a result of passing the dislocation through it.

2.3.3 Factors affecting impact toughness

The main factors affecting the toughness properties of steels are: i) macrosegregation during solidification, ii) grains with high and low angle boundaries, iii) precipitates and brittle second phase particles, iv) NMIs, and v) retained austenite.

Macrosegregation during the solidification can cause deterioration and anisotropy of all mechanical properties because of the localized impurities and alloying elements. Those cannot be homogenized during the subsequent heat treatments and persist through the whole process route, affecting the hardenability, austenite recrystallization, grain growth, precipitation kinetics of carbides and formation of detrimental and large Al, Ca, Mn and Ti based NMIs. On the other hand, increasing the concentration of alloying elements can refine the austenite grain size through solid solution effect on the recrystallization kinetics, or grain boundaries pinning effect by microalloy carbides or nitrides [75].

The impact toughness and DBTT can be improved by refining the PAGS, as well as the martensite packet and block sizes [16], [17], [67]. These features represent the grains with high angle boundaries which act as a barrier to the crack propagation [54]. Kennett et al. [18] concluded that in the as-quenched and low-temperature tempered microalloyed ASTM A514 steel, lower DBTT can be obtained by refining the PAGS. On the other hand, the sub-grains or low angle grain boundaries have no direct effect on the impact toughness but can cause a strengthening effect which may reduce the toughness because of increasing the yield stress without any increase in the cleavage stress.

Generally, precipitates and second phase particles have a detrimental effect on toughness, especially those located at the grain boundaries [76]. For example, the presence of coarse brittle second phase particles in the microstructure, i.e. cementite at the grain boundaries, has a detrimental effect on the DBTT. The pile-ups of dislocations at the head of these particles results in particles cracking. The

cracked particle may remain in the structure and the crack blunted by the following plastic deformation. However, in the case of large cracks, the cracks may be propagating through the matrix [54].

Particularly large and angular NMIs with less hot deformability than the steel matrix are harmful to such properties as toughness, ductility, fatigue resistance and corrosion resistance. NMIs can be classified into two categories: indigenous and exogenous. Indigenous inclusions form in the molten steel as a result of internal sources, i.e. because of deoxidation or reoxidation or the formation of sulphides, while exogenous inclusions are formed as a result of external sources such as refractory erosion or slag entrainment [77]. Low melting temperature NMIs, which occur as spherical liquid inclusions during steel production, are removed easily from the molten metal. In addition, they have greater deformability [78]–[82]. Cleanliness of steel can be evaluated by the number density, size distribution and shape of the NMIs. Many techniques are available to decrease and control NMIs, i.e. control of the dissolved oxygen, use of a protective atmosphere [83], filtration of the melt, inert gas stirring [84], slag absorption [85] and inclusion modification [86].

The presence of RA in the microstructure can improve the toughness properties through inhibiting the fast propagation of the cleavage fracture in a number of ferrite and martensitic steels [76].

2.4 Electroslag remelting

ESR is a low-cost secondary refining process used widely for production of high-quality materials such as tool steels, wear resistance steels, corrosion and acid resistance steels, high speed steels, Ni superalloys and Ti and Zr alloys. ESR improves the quality of the produced steel ingots and improves the mechanical properties such as impact toughness, ductility and corrosion resistance by eliminating the macrosegregation, enhancing the chemical homogeneity and reducing the level of impurities and NMIs content [87]. In addition, it provides an ingot with dense structure free from inner porosity and holes and gives a smooth surface, which can be subjected to the required hot working without any prior surface treatment [88].

ESR is a continuous process (see Fig. 6) including remelting, refining and solidification of steel. The main idea of the process is an electrical current passing via the consumable electrode through the used synthetic slag, and the fused slag starts to melt as a result of its high electrical resistivity and heat generated by the joule heat effect. Once the consumable electrode is immersed in the molten slag,

the electrode starts to heat, and its tip starts to melt. Then a stream of molten steel droplets passes through the molten slag and is refined through the interactions between the slag and the molten metal droplets, i.e. removing of oxides and sulfides. After passing the slag, the molten droplets are collected below the molten slag and form a new and refined ingot. Usually, the whole process takes place in a copper mould which is cooled with water, which ensures faster and uniform solidification [87], [89].

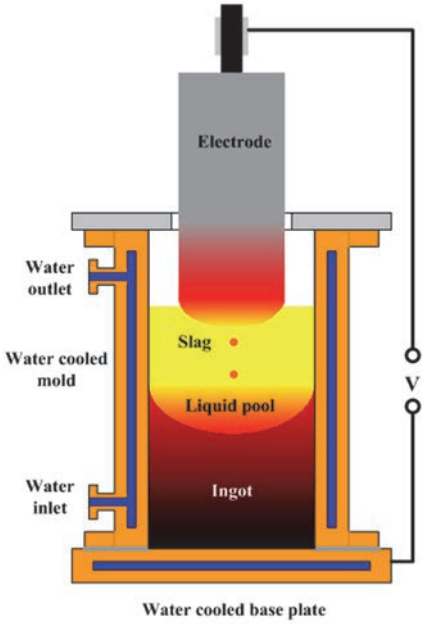

Fig. 6. Electroslag remelting (Under CC BY-NC-SA license from [90] © 2012 Author).

In the ESR, the slag plays various roles, i.e. source of heating and melting of the consumable electrode, protecting the molten metal from the oxidation which has the main powerful effect on the yield of alloying elements, and facilitating the refining reactions besides desulphurization and removal of exogenous NMIs [91], [92]. Reducing slag should be used to control the oxygen level to be minimum, which leads to a high yield of the alloying elements in the remelted ingot. NMIs are removed during ESR mainly at the tip of the consumable electrode by absorption and dissolution in the slag. The degree of cleanliness of the remelted ingots using ESR depends on several parameters like steel composition, NMIs

content of the consumable electrode, furnace atmosphere, slag composition and amount, power input and melting rate [93].

In ESR, the following steps are relevant to the oxidation of the alloying elements: since the temperature of the molten slag increases above the melting point of the metal, the metal starts to melt and form droplets at the tip of the consumable electrode, which fall through the molten slag pool. Due to the high temperature of the molten metal droplets, the oxidation of the alloying elements can occur depending on their affinity to oxygen. For the elements with high affinity to oxygen, the oxidation reactions can take place by the atmospheric oxygen and the oxidation rate depends mainly on the surface area exposure to the atmospheric oxygen, so the oxidation reaction will be increased by increasing the melting rate. For the elements with lower affinity to oxygen, the oxidation reaction occurs during the transfer of the molten metal droplet through the molten slag pool by oxygen diffusion, which depends on the physical properties of the slag. A protective layer from the molten slag can be formed on the falling droplets as a result of increasing the wetting of the falling droplets with the molten slag, i.e. reducing the interfacial tension. This layer decreases the diffusion of oxygen to the metal droplet and the rate of oxidation, thereby enhancing the yield of the alloying element. Also, increasing the viscosity of slag can reduce the oxygen transfer to the metal droplets.

At the metal/slag interface, slag can oxidize the elements in the molten metal, i.e. Mn, and form cations which are then incorporated into the slag, and these cations could be reduced through electron exchange in the slag and incorporated into the molten metal pool. These chemical reactions could be indicated [94] by the oxidation reaction

$$\mathrm{Mn}_{\,metal} + 2\mathrm{O}^{-} \leftrightarrow \mathrm{Mn}^{2+} + 2\mathrm{O}^{2-} \tag{7}$$

and by the electron exchange reaction

$$\mathrm{Mn}^{2+} + 2\mathrm{Fe}^{2+} \leftrightarrow \mathrm{Mn}_{metal} + 2\mathrm{Fe}^{3+}. \tag{8}$$

The direction of the reactions depends on the oxygen potential, which is provided by either the activity of oxidizing anions or activity of reducing cations, and the Mn activity in the molten metal pool.

Increasing the activity of oxygen, and oxidation rate, and reducing the reduction rate leads to decreasing the yield of alloying elements or formation of NMIs [95]. The oxidation, reduction and inclusion formation reactions could be indicated by

$$x[\mathrm{M}] + \frac{y}{2}\mathrm{O}_2 \rightarrow (\mathrm{M}_x\mathrm{O}_y), \tag{9}$$

$$(M_xO_y) \rightarrow x[M] + y[O], \tag{10}$$

and

$$x[R] + y[O] \rightarrow (R_xO_y). \tag{11}$$

In oxidation, reduction, and inclusion formation reactions (Eqs. (9)–(11)), M is the metal to be remelted (usually a transition metal) and R describes alloying elements characterized by their high affinity to oxygen, i.e. Al, Si or Ti.

Increasing the activity of oxygen in the molten slag oxidizes a high percentage of Si and leads to forming silica by reaction

$$[Si] + 2(FeO) \leftrightarrow (SiO_2) + 2[Fe]. \tag{12}$$

Then, CaO in the slag reacts with SiO_2 to form a high stable calcium silicate ($CaO.SiO_2$) in the produced slag, which decreases the activity of silica and yield of Si in the remelted ingot [95].

The carbon content of steel can be increased by ESR as a result of carbon in the molten slag, which increases during its fusion.

As commonly known for all UHSSs, it should have a low level of impurities, i.e. S, P and NMIs. Also, it should be without defects like cracks and voids, and have a homogeneous chemical composition [6].

The desulphurization or removal of sulphur occurs through two chemical reactions, the first one at the slag/metal interface followed by the reaction at the slag/gas interface, as given in reactions [6], [96], [97]

$$[S]_{metal} + (O^{2-})_{Slag} \leftrightarrow (S^{2-})_{Slag} + [O]_{Metal\ Drop} \tag{13}$$

and

$$\frac{3}{2}O_{2(g)} + (S^{2-})_{Slag} \leftrightarrow (O^{2-})_{Slag} + SO_{2\ (g)}. \tag{14}$$

From Eq. (13), the amount and activity of oxygen ions in the metal and slag are the controlling factors for transfer of sulphur from the molten metal to the molten slag. The desulphurization can be enhanced through reducing the activity of oxygen in the molten metal and increasing its activity in the molten slag. Another desulphurization mechanism is given by Hayashi et al. [98], in which the removal of sulphur improves by dissolution with an oxygen ion (O^-), thus supplying oxides in slag as follows

$$\frac{1}{2}S_{2(g)} + (M_xO)_{Slag} \leftrightarrow \frac{1}{2}O_{2(g)} + (M_xS)_{Slag}. \tag{15}$$

Eissa et al. [99] and Vaish et al. [6] stated that most of the sulphur transfers from the molten slag to the atmospheric air, but that depends on the transfer of sulphur from the molten metal to the molten slag, as illustrated by Eq. (13).

The dephosphorization or removal of phosphorus occurs through oxidation followed by absorption by the molten slag, as given by reaction

$$2[\mathrm{P}]_{Metal} + 5[\mathrm{O}]_{Metal} + 3(\mathrm{O}^{2-})_{Slag} \leftrightarrow 2(\mathrm{PO}_4^{3-})_{Slag}. \quad (16)$$

This process depends mainly on the activity and partial pressure of oxygen.

The denitrification or removal of nitrogen may occur by two means: removal of nitride inclusions physically by the molten slag, or by dissolutions depending on the slag capacity, carbon content of the system and existence or non-existence of strong nitride forming elements. This take place at the molten slag/metal interface according to the chemical reactions

$$[\mathrm{N}]_{Metal} + \frac{3}{2}(\mathrm{O}^{2-})_{Slag} \leftrightarrow (\mathrm{N}^{3-})_{Slag} + \frac{3}{2}[\mathrm{O}]_{Metal\ drop} \quad (17)$$

or

$$\mathrm{N}_{2(\mathrm{g})} + (\mathrm{C}^{2-})_{Slag} \leftrightarrow (CN_2^{2-})_{Slag}. \quad (18)$$

The denitrification can be enhanced by decreasing the oxygen activity in the molten metal while increasing it in the molten slag.

Nowadays, there are different versions of ESR [87], [88] which have been developed to be used for specific purposes, i.e. pressure electroslag remelting (P-ESR), ESR operated under protective inert gas (I-ESR) and ESR operated under vacuum (VAC-ESR).

In P-ESR, the steel is melted and solidifies under nitrogen pressure. So, the nitrogen can be introduced to the molten steel and the used pressure depends mainly on the required nitrogen level in the refined ingots and the targeted steel composition. This process is used in the production of corrosion resistant austenitic steels.

In I-ESR, the steel is melted under an inert gas, i.e. argon, at the atmospheric pressure which protects the molten slag and molten metals from the absorption of hydrogen or nitrogen from the atmospheric air; in addition, the oxidation is prevented during the process, which reduces the possibility of the formation of oxides inclusions and improves the cleanliness of the produced steel ingots. But the drawback of this process is its inefficiency to reduce the level of sulphur due to the absence of oxygen during the process. This process can be used in the remelting of steels containing a low level of Si, Al or Ti.

In VAC-ESR, the dissolved gases, i.e. nitrogen and hydrogen, are removed from the molten metal by vacuum degassing. Also, the molten metal is protected from the atmospheric oxygen. This process is used in the remelting of superalloys and Ti alloys.

Usually, ingots processed using ESR contains some segregation. Sometimes VAR is added to the process chain to reduce the segregation in the remelted ingots. Generally, the degree of segregation depends on the solidification time (mushy zone depth/ rate of advance of solidification front). So, longer solidification time or a deep mushy zone can lead to a high degree of segregation. The differences in heat generation and heat transfer characteristics in ESR and VAR remelted ingots affect the mushy zone shapes resulting in a large difference in the degree of segregation obtained. The U-shaped pool profile in VAR with a shorter and more uniformly distributed mushy zone leads to a lower degree of segregation than that obtained in ESR with a V-shaped pool profile with a longer mushy zone. However, using VAR may be a source of other problems: i) the formation of inclusions in the liquid pool disturbs the arc gap control, ii) evaporation losses of alloying elements, iii) lack of possibility to exchange the consumable electrode to produce bigger ingots like in ESR, and iv) the formation of white spots containing nitride and oxide inclusions [100], [101].

2.5 Double quenching and tempering process

The double quenching and tempering process is used to improve the strength and toughness combination. Most of the previous studies [22]–[26] about the double quenching and tempering process were performed on low to medium strength steels with the aim of improving the toughness-strength combination. Khani Sanij et al. [22] studied the effect of single and double quenching followed by tempering on the final microstructure and mechanical properties of hot-rolled 4140 type steel and concluded that the impact toughness improved by about 23% by the double quenching and tempering over the single quenching and tempering, while it has no effect on the hardness and strength. They attributed the enhancement in the impact toughness to the reduction in the PAG and the martensitic packet sizes, in addition to the lower level of impurity elements near prior austenite grain boundaries, compared to the single quenching and tempering process. Liu et al. [23] studied the microstructure and mechanical properties of a low-carbon 5Cr as-cast steel subjected to the double quenching and tempering process and showed a slight enhancement in the yield strength associated with a significant improvement in the

impact toughness. They attributed the enhancement in the yield strength to the precipitation strengthening in addition to the refinement of the PAGS and the martensitic block size, while the main reason for the significant improvement in the toughness is the overall microstructural refinement, including the precipitates formed at the PAG boundaries. Rao and Thomas [24] concluded that the double austenitization of Cr and Mn modified Fe-4Cr-C structural steels and improved the toughness, which was attributed to the increment in the volume fraction of the RA in addition to the refinement of the grains. Sarikaya et al. [25] concluded that the impact toughness of Fe–Cr–C–based structural steels improved after they were subjected to double austenitization treatment, while the strength decreased slightly, because of the increment in the volume fraction of RA with the refinement of the PAGS. Chang et al. [26] concluded that the toughness of Ni–Cr–Mo–V steels increased by the double quenching and tempering process as a result of decreasing the aspect ratio of carbides. So, the previous studies [22]–[26] show that the influence of the double quenching and tempering process on the microstructure and mechanical properties is based on the steel composition.

3 Experimental

The current project was performed in four different stages: i) designing, production and forging, ii) characterization of the produced steels without and with ESR, iii) simulation, and iv) heat treatment, as illustrated in Fig. 7.

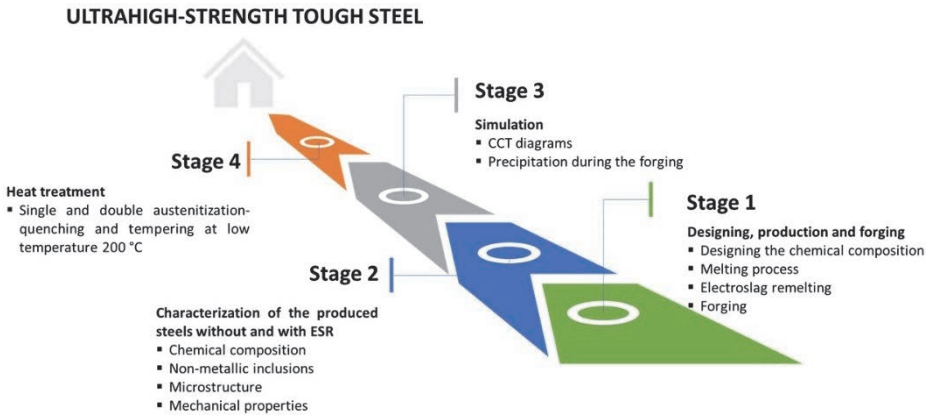

Fig. 7. Stages toward ultrahigh-strength tough steel.

3.1 Materials and production methods

As illustrated in Paper I, six experimental heats of steels were designed and produced by melting of steel scrap, ferroalloys and nickel alloy given in Table 3 in an air induction furnace. The molten metal was tapped at about 1570 °C into a 70-mm diameter and 250-mm long steel mould. The chemical composition of the steels was determined using 10-mm thick samples which were cut from the bottom of the produced ingots after removing 20-mm thick from the bottom. The produced ingots were reheated to 1100 °C and held for one hour, then subjected to the forging in the temperature range of 1100–950 °C to produce steel bars with cross section 28x30 mm. Half of the produced forged bars were used as a consumable electrode and refined using ESR, and then the refined ingots were forged using the same forging parameters used for the base ingots. The chemical composition of the synthetic fused slag used in the remelting process is given in Table 4, while the chemical compositions of the produced steels without and with ESR are given in Table 5.

Table 3. Chemical composition of charged materials (Under CC BY license from Paper I © 2017 Authors and Scientific Research Publishing Inc.).

Charging	Chemical composition, wt.%												
Materials	C	Si	Mn	Cr	Ni	V	W	Mo	Al	P	S	Ca	Fe
Scrap 1	0.30	0.30	1.08	-	-	0.01	-	-	-	0.030	0.022	-	Bal.
Scrap 2	0.10	0. 17	0.35	-	-	0.01	-	-	-	0.028	0.021	-	Bal.
LC Fe-Mn	0.30	2.30	80.60	-	-	0.04	-	-	-	-	-	0.31	16.10
Fe-Si	-	72.10	0.39	-	-	0.04	-	-	1.50	-	-	1.40	24.00
Fe-V	-	2.50	0.26	-	-	77.50	-	-	3.03	-	-	0.20	16.00
LC Fe-Cr	-	2.90	0.50	65	-	0.20	-	-	0.65	-	-	-	30.00
Fe-Mo	-	2.00	0.21	-	0.36	0.15	-	55.55	-	-	-	-	41.50
Fe-W	-	-	1.00	-	-	0.12	69.00	0.90	-	-	-	2.50	26.00
Ni alloy	-	0.90	0.02	-	97.60	0.01	-	-	-	-	-	0.40	0.07

Table 4. Chemical composition of synthetic pre-fused slag (wt. %) [Paper I].

CaF_2	CaO	Al_2O_3	SiO_2	TiO_2	P_2O_5	SO_3	Fe_2O_3
62-70	12-15	15-20	1.85	0.14	0.01	0.15	0.12

The used ESR machine (see Fig. 8) comprises a water-cooled crystallizer for melting and solidifying the steel and a power supply with regulation parts to control the current and voltage. The process parameters were 1200–1500 A for current, 30–40 V for voltage and 4.63 g/s for melting rate. During the ESR, a small amount of aluminium (about 0.1% of the total weight of the consumable electrode) was used as deoxidant.

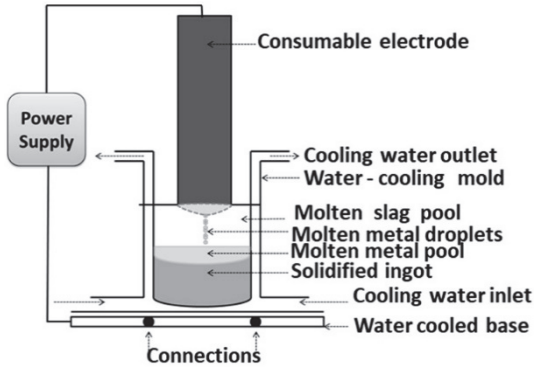

Fig. 8. A schematic diagram of the ESR machine (Under CC BY-SA license from Paper III © 2019 Authors).

The production and analysis of steels #1–#6 without and with ESR are given in Paper I. Steel #2 without and with ESR is examined in Paper II and steels #1, #3 and #4 without and with ESR are investigated in Papers III and IV. Further investigation is performed on steel #3 in Paper V, on steel #1 and #2 in Paper VI and on steel #1 and #4 in Paper VII.

3.2 Methods and characterization techniques

Table 6 gives all characterization techniques and the simulation instrument used in the current study in addition to the actual uses for each of them.

3.2.1 Characterization techniques

Various characterization techniques (given in Table 6) have been used in the current work, which include: i) chemical analytical techniques used for analysis of the chemical composition of the charging materials, fused synthetic slag and the produced steels without and with ESR, ii) simulation technique, iii) microstructural characterization techniques, and iv) mechanical properties characterization techniques. For more details about the characterization techniques and the parameters used, see the original publications.

Table 5. Chemical composition of steels without and with ESR (wt. %).

Steel	Process	C	Cr	Ni	Mo	W	Mn	Si	V	Ti	Nb	Cu	Al	P	S	N	O	Paper
#1	IF	0.30	2.32	2.34	0.32	1.21	0.70	0.71	0.08	0.001	0.001	0.017	0.009	0.019	0.024	0.013	0.014	I,III,IV
	ESR	0.32	2.18	2.31	0.31	1.14	0.64	0.64	0.07	0.001	0.001	0.020	0.060	0.018	0.013	0.011	0.004	I,III,IV,VI,VII
#2	IF	0.25	1.57	3.27	0.30	1.46	0.60	0.78	0.07	0.001	0.002	0.015	0.016	0.020	0.019	0.020	0.017	I,II
	ESR	0.31	1.57	3.13	0.30	1.26	0.57	0.65	0.07	0.002	0.002	0.013	0.043	0.020	0.012	0.016	0.013	I,II,VI
#3	IF	0.25	2.40	2.49	0.32	1.34	0.57	0.89	0.09	0.002	0.001	0.018	0.009	0.019	0.025	0.020	0.011	I,III,IV
	ESR	0.29	2.37	2.45	0.33	1.23	0.53	0.81	0.09	0.003	0.001	0.020	0.058	0.019	0.014	0.018	0.007	I,III,IV,V
#4	IF	0.15	1.73	4.44	0.31	1.33	0.41	0.51	0.07	0.002	0.002	0.016	0.009	0.018	0.022	0.022	0.012	I,III,IV
	ESR	0.18	1.65	4.35	0.32	1.24	0.35	0.31	0.06	0.001	0.001	0.020	0.043	0.018	0.017	0.015	0.006	I,III,IV,VII
#5	IF	0.09	2.07	3.11	0.30	1.07	0.69	0.47	0.05	0.001	0.001	0.011	0.008	0.017	0.019	0.020	0.024	I
	ESR	0.14	2.06	3.09	0.31	1.00	0.61	0.34	0.05	0.001	0.001	0.010	0.044	0.017	0.013	0.008	0.009	I
#6	IF	0.06	3.50	1.01	0.45	1.79	0.33	0.88	0.08	0.001	0.001	0.016	0.013	0.022	0.023	0.033	0.006	I
	ESR	0.07	3.21	1.01	0.46	1.62	0.32	0.43	0.08	0.001	0.001	0.017	0.029	0.022	0.014	0.021	0.011	I

IF: Induction Furnace Ingots

ESR: Electroslag Remelting Ingots

Table 6. List of different instruments and characterization techniques.

Techniques	Instrumental model	Uses
Chemical analytical techniques		
X-ray fluorescence (XRF)	XRF Philips PW 1410 X-Ray Spectrometer with PW 1390 channel control	Analysis of chemical composition of ferroalloys, nickel alloy and synthetic fused slag (Paper I)
Optical emission spectrometry	SPECTRO analytical instrument	Analysis of chemical composition of steel scrap, produced steel without and with ESR (Paper I)
C S analyzer	LECO CS444 (C.S–Mat 650)	Determination of C content in slag before and after ESR (Paper I)
ONH analyzer	ELTRA ONH 2000	Determination of N content in steel (Paper I)

Techniques	Instrumental model	Uses
Nitrogen analyzer	KJELDAHL method	Determination of N in slag before and after ESR (Paper I)
Oxygen analyzer	LECO combustion analysis	Determination of O in steels before and after ESR (Paper I)
Simulation technique		
Gleeble thermomechanical simulator	Gleeble 3800 thermomechanical simulator	Obtain the dilatation curves for construction of CCT diagrams and study the effect of steel composition and CR on the microstructural features and mechanical properties. (Paper VI) Study the effect of forging parameters on the strain induced precipitation and final microstructural features. (Paper V)
Microstructural characterization techniques		
Laser scanning confocal microscopy (LSCM)	3D Laser Scanning Microscope VK-X100K/X200K	Different microstructure features (Papers II, IV, VI and VII) NMIs (Paper III)
Field emission scanning electron microscopy (FESEM) and EDAX electron backscatter diffraction (EBSD) system on the FESEM	Zeiss Sigma FESEM	Different microstructure features (Papers II, IV, V, VI and VII)
Field emission scanning electron microscopy (FESEM)	Zeiss ULTRA Plus FESEM	NMIs investigation (Papers II and III)
Transmission electron microscopy (TEM)	JEOL JEM-2200FS EFTEM/STEM	Carbides investigation (Papers V and VII)
Electron probe microanalysis (EPMA)	Jeol JXA-8200 EPMA	Degree of homogenization of the steel matrix before and after ESR (Papers II and IV) Carbide formed at the grain boundaries (Paper VI)
X-ray diffraction (XRD)	Rigaku SmartLab X-Ray diffractometer with Co Kα radiation	Retained austenite volume fraction (Papers II, IV, VI and VII)

Techniques	Instrumental model	Uses
PAG reconstruction	MATLAB software 2018a, MTEX 5.1.1 and MTEX texture and crystallographic analysis toolbox.	Using EBSD data, the original prior austenite grains were reconstructed using MATLAB software with the aid of the MTEX texture and crystallographic analysis toolbox [102], as described by Javaheri et al.[103] and Nyyssönen et al.[104], [105] (Papers V,VI and VII)
Mechanical characterization techniques		
Microhardness test	CSM microindentation tester	Microhardness of different phases (Paper VI)
Macrohardness test	Duramin-A300(Struers) macrohardness tester	Bulk hardness measurement (Papers II, IV, VI and VII)
Tensile test machine	Zwick/Roell machine with a maximum load capacity of 100 kN	Tensile properties (papers II, IV, VI and VII)
Impact test machine	Calibrated Charpy impact test hammer with a capacity of 350 J	Impact toughness (Papers II, IV, VI and VII)

3.2.2 Gleeble simulation tests

CCT diagrams

A Gleeble 3800 thermomechanical simulator was employed to get the dilatation curves to construct the CCT diagrams of steels #1 and #2 presented in Paper VI. Cylindrical specimens with 6-mm diameter and 20-mm length were machined from the forged bar with cylindrical axis which is parallel to the forging direction. The dilatation curves for the critical transformation temperatures A_{c1} and A_{c3} were obtained during heating of the specimens at 5 °C/s to 1100 °C, while the dilatation curves for the transformation temperatures on cooling were obtained after heating the specimens to 1100 °C at 5 °C/s, held for 3 min, cooled at 2 °C/s to 950 °C, held for 3 min and then cooled to room temperature with a wide range of CRs of 0.01–60 °C/s, as shown in Fig. 9. The tangent method on dilatation curves was used to determine all transformation temperatures.

The thermal treatment with CRs of 60, 1 and 0.01°C/s shown in Fig. 9 was used in order to study the influence of CR and composition on the final microstructural features and the mechanical properties of steels #1 and #2.

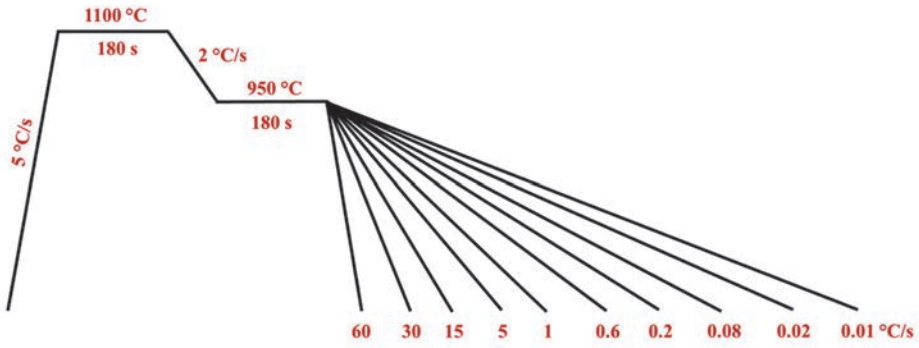

Fig. 9. Thermal cycles to construct CCT diagrams (Reprinted [adapted] under CC BY license from Paper VI © 2019 Authors).

Simulation of the forging process

Cylindrical samples were machined with 5-mm diameter and 7.5-mm length with axis parallel to the forging direction of the forged bar. The influence of forging parameters, i.e. TAS and FFT, on the precipitation kinetics and final microstructural

features of steel #3 were studied according to the simulation procedures shown in Fig. 10 and the conditions given in Table 7.

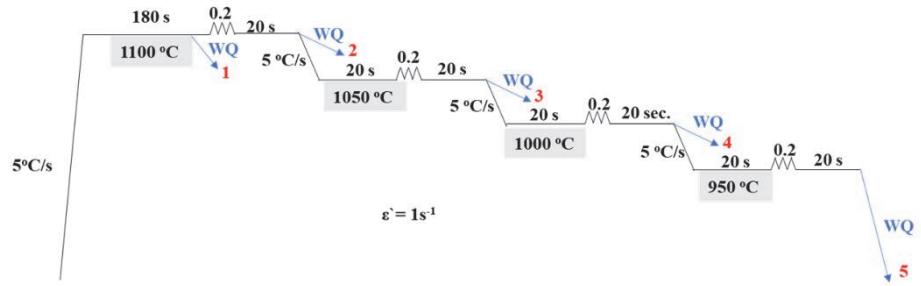

Fig. 10. Gleeble simulation procedure for the forging process (Reprinted by permission from Paper V © 2020 WILEY-VCH).

Table 7. Conditions and samples codes (Reprinted [adapted] by permission from Paper V © 2020 WILEY-VCH).

Thermomechanical treatment	Sample code	Total applied strain (TAS)	Finish forging temperature (FFT), °C
1	1100-0	0	1100
2	1100-0.2	0.2	1100
3	1050-0.4	0.4	1050
4	1000-0.6	0.6	1000
5	950-0.8	0.8	950

3.2.3 Heat treatment

Single and double austenitization and quenching followed by tempering were applied to steels #1 and #4 in order to evaluate their effect on their microstructure and mechanical properties (presented in Paper VII). Different specimens were cut parallel to the forging direction from the refined-forged bars of steels. For the single austenitization and quenching followed by tempering (SAQT), the specimens were heated at 0.03 °C/s to 930 °C, held for 1 h, and quenched to room temperature in oil in the case of steel #1 and in water in the case of steel #4. Then the specimens were heated at 0.03 °C/s to 200 °C, held for 2 h and then air-cooled (see Fig. 11).

For the double austenitization and quenching followed by tempering (DAQT), the same treatment above was used after the specimens were heated to 1100 °C at 0.03 °C/s, and held for 1 h quenched to room temperature in oil in the case of steel #1 and in water in the case of steel #4 (see Fig. 11).

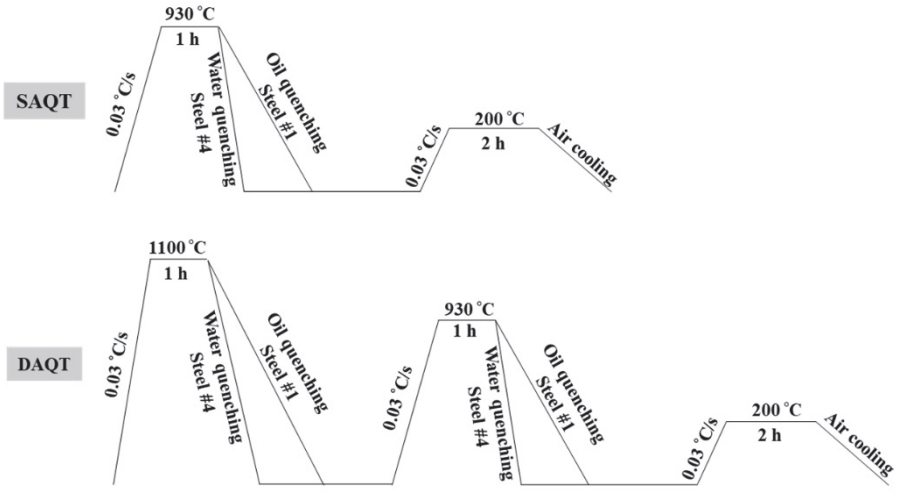

Fig. 11. Thermal cycles for single and double austenitization and quenching followed by tempering for steels #1 and #4. SAQT: single austenitization and quenching followed by tempering, DAQT: double austenitization and quenching followed by tempering (Under CC BY-NC-ND license from Paper VII © 2020 Authors).

4 Results and discussion

4.1 Effect of ESR on the yield of alloying elements and impurities

In Paper I, the influence of ESR with a slag consists of 70% CaF_2, 15% CaO and 15% Al_2O_3 on the yield of alloying elements C, Cr, Ni, Mo, W, Mn, Si and V, and the level of impurities S, P, N and O were explained in terms of their activities using the chemical composition of the produced steels without and with ESR.

4.1.1 Effect of ESR on the yield of alloying elements

Using the chemical composition of the investigated steels without and with ESR given in Table 5, the changes in the alloying elements C, Cr, Ni, Mo, W, Mn, Si and V were calculated and shown in Fig. 12. High yields of the alloying elements Cr, Ni, Mo, W, Mn, and V were attained after ESR. This was attributed to the protection of the molten metal provided by the used slag, which provides a protective layer preventing the transfer of oxygen from the atmospheric air to the molten metal. Also, the addition of Al as deoxidant decreases the activity of oxygen and oxidation kinetics of the alloying element in the molten slag. In steels #3, #4, #5 and #6, Mo wt.% is increased because of its low interaction coefficient with the oxygen and its less negative free energy of oxidation, combined with the slight change in the chemical composition due to the small losses in the alloying elements like Si, Mn, V and Cr and the losses in the impurities S, N and P.

The current results are in line with those obtained by Birol et al. [106], who concluded that the losses in Cr, W and Mo alloying elements were not more than 10%, and also those observed by Mattar [107], who concluded that the increase in non-oxidizable elements such as Mo and W in the remelted ingot could be because of the losses of the oxidizable elements like Cr, Mn, Si and V.

The elemental concentration changes in percentage are calculated using the equation

$$\text{Net percentage change or loss } = ([x_i] - [x_e]/[x_e]) \times 100, \quad (19)$$

where $[x_i]$ is elemental concentration in the remelted ingot and $[x_e]$ is elemental concentration in the consumable electrode.

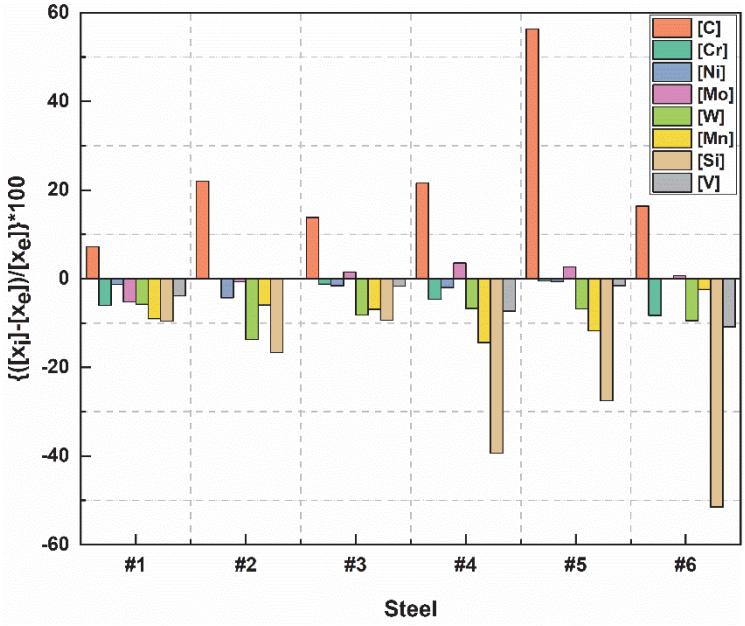

Fig. 12. Elemental concentration changes in percentage as a result of ESR. [X] = [C], [Cr], [Ni], [Mo], [W], [Mn], [Si], and [V] (Reprinted [adapted] under CC BY license from Paper I © 2017 Authors and Scientific Research Publishing Inc.).

In the current study, since all ESR process parameters, i.e. the slag composition, melting rate, and power are fixed, the only variable is the initial chemical composition of the consumable electrode. In ESR, the molten steel pool contains lots of elements, including C, Cr, Ni, W, Si, Mn, Mo, V, Al, Cu, S, P and N, and the combined influence of all these elements should be considered. So, using the initial chemical composition, the interaction parameters between all of these elements in the molten state are considered and used to study the change in the yield of the alloying elements. The activity coefficient of each alloying element was calculated using the equation [108]

$$\log f_i = \sum_{j=2}^{k} e_i^j \,[\%j], \tag{20}$$

where i and j are the solute atoms in melt, f_i is the activity coefficient of the solute atom i, e_i^j is the interaction coefficient between solutes (i and j) and [%j] is the concentration in % of solute atom j in the melt.

The activity of each element in the molten steel (a_i) is calculated using equation

$$a_i = f_i . x_i, \quad (21)$$

where x_i is the mass % of the element i in steel.

Table 8 gives the interaction coefficient between the elements in the molten metal pool, which is used in order to calculate the elemental activity coefficient used in the current study. The calculated activity coefficient and the activities for all elements in the molten metal are provided in Table 9.

The yield of alloying elements Cr, Ni, W, Mn and V (see Fig. 13(a)–(e)) decreased in the remelted ingots as a result of increasing their activities in the molten state during ESR, because the higher activity promotes the oxidation reactions for these elements and then moves to the molten slag, thereby decreasing their yields in the remelted ingots.

Mo shows different behavior from the other elements (see Fig. 13(f)), as it increases in some cases as percentage due to the small losses in the other elements like Cr, Mn, Si, V, S, P and N. But it is difficult to get such conclusions about the influence of Mo activity because it is almost similar, about 0.29, with only one steel having a little higher Mo activity of about 0.44.

Ni shows high yield in all investigated UHSSs and is little affected by the activity of Ni. This may be attributed to the low affinity between Ni and O.

Mn has high affinity to S and O, which is observed from the high negative interaction coefficients, and this decreases the Mn activity in the molten metal. The low activity of Mn in the molten metal and the high activity of MnO in the molten slag, decrease the losses of Mn and provide high yield in the remelted ingot as illustrated by reaction

$$(\mathrm{MnO}) + [\mathrm{Fe}] \rightarrow [\mathrm{Mn}] + (\mathrm{FeO}), \quad (22)$$

which has the equilibrium constant of $K=a_{[\mathrm{Mn}]}a_{(\mathrm{FeO})}/a_{[\mathrm{Fe}]}a_{(\mathrm{MnO})}$. The losses of Mn in the investigated UHSSs range from 2% to 14%. These results are in a good agreement with those obtained by Bandyopadhyay et al. [109], who studied the behaviors of alloying elements during ESR of AFNOR 15CDV6 and the modified 15CDV6 steels with about 0.29 wt.% C and 1.5 to 4.4 wt.% Cr using slag with the composition of 70% CaF_2–30% Al_2O_3, Ti ferroalloys (FeTi:Ti 35%, Al 5%) powder used as inoculants, high-carbon ferrochrome powder used to reimburse the losses of Cr and C, and Al added continuously during ESR, and they concluded that Mn losses are only in the range of 2–13%.

Table 8. Interaction coefficient e_i^j of all elements in the molten steel (Reprinted [adapted] under CC BY license from Paper I © 2017 Authors and Scientific Research Publishing Inc.).

e_i^j	C	Cr	Ni	Mo	W	Mn	Si	V	Cu	Al	P	S	N	O
C	0.1240	-0.0240	0.0120	-0.0080	-0.0056	-0.0120	0.0800	-0.0770	0.0160	0.0430	0.0510	0.0460	0.0900	-0.3400
Cr	-0.1200	-	0.0002	-0.0020	-	-	-0.0043		0.0200	-	-0.0530	-0.0200	-0.1800	-0.1400
Ni	0.0420	-0.0003	0.0009	-	-	-	0.0057	-	-	-	-0.0035	-0.0037	0.0130	0.0000
Mo	-0.1000	-0.0003	-	-	-	-	-	-	-	-	-	-0.0005	-0.1000	-
W	-0.1500	-	-	-	-	-	-	-	-	-	-	0.0350	-0.0700	-0.0520
Mn	-0.0700	-	-	-	-	-	-	-	-	-	-0.0035	-0.0480	-0.1500	-0.0830
Si	0.1800	-0.0003	0.0050	-	-	-	0.1100	0.0250	0.0140	0.0580	0.1100	0.0580	0.0900	-0.2300
V	-0.3400	-	-	-	-	-	0.4200	0.0150	-	-	-	-0.0280	-0.3500	-0.9700
Al	0.0910	-	-	-	-	-	0.0056	-	-	0.0450	-	0.0300	-0.0580	-6.6000
P	0.1300	-0.0300	0.0002	-	-	-	0.1200	-	0.0240	-	0.0620	0.0280	0.0002	0.1300
S	0.1100	-0.0110	-	0.0030	0.0100	-0.0260	0.0630	-0.0160	-0.0080	0.0350	0.2900	-0.0280	0.0100	-0.2700
N	0.1030	-0.0460	0.0063	-0.0110	-0.0015	-0.0400	0.0470	-0.0930	0.0090	-0.0300	0.0450	0.0070	-	0.0500

Table 9. The calculated activity coefficient (f_i) and activity (a_i) of elements in the molten steel (Reprinted [adapted] under CC BY license from Paper I © 2017 Authors and Scientific Research Publishing Inc.).

Steel	f_i & a_i	Cr	Ni	Mo	W	Mn	Si	V	P	S	N
#1	fi	0.902	1.042	0.929	0.893	0.943	1.405	1.509	1.146	1.121	0.859
	ai	2.092	2.439	0.301	1.080	0.659	0.996	0.113	0.031	0.027	0.011
#2	fi	0.910	1.041	0.939	0.902	0.949	1.418	1.661	1.215	1.152	0.947
	ai	1.429	3.405	0.283	1.317	0.572	1.109	0.120	0.033	0.022	0.019
#3	fi	0.910	1.040	0.938	0.903	0.949	1.451	1.874	1.182	1.148	0.868
	ai	2.185	2.591	0.304	1.210	0.537	1.296	0.163	0.031	0.029	0.017
#4	fi	0.941	1.029	0.961	0.935	0.965	1.287	1.402	1.079	1.085	0.914
	ai	1.628	4.571	0.300	1.243	0.395	0.658	0.094	0.026	0.024	0.020
#5	fi	0.952	1.021	0.973	0.952	0.972	1.218	1.373	1.029	1.024	0.834
	ai	1.971	3.174	0.295	1.019	0.669	0.576	0.071	0.025	0.019	0.017
#6	fi	0.939	1.017	0.977	0.950	0.966	1.281	1.905	1.043	1.059	0.738
	ai	3.287	1.028	0.443	1.700	0.316	1.122	0.160	0.031	0.024	0.024

Si shows a low yield in the remelted ingot due to its high affinity to oxygen. As FeO formed in the molten slag by diffusion of the atmospheric oxygen, it led to oxidize Si in the consumable electrode according to the reaction

$$2(\mathrm{FeO}) + [\mathrm{Si}] \rightarrow 2[\mathrm{Fe}] + (\mathrm{SiO_2}). \quad (23)$$

The large increment of Al_2O_3 in the molten slag can cause more losses in the yield of Si in the remelted ingot. As at high concentration of Al_2O_3 in the slag, Si begins to reduce Al_2O_3 and it oxidized to SiO_2 and transferred to the molten slag according to the reaction

$$3[\mathrm{Si}]_{metal} + 2(\mathrm{Al_2O_3})_{slag} \leftrightarrow 4[\mathrm{Al}]_{metal} + 3(\mathrm{SiO_2})_{slag}. \quad (24)$$

Then CaO in the molten slag reacts with SiO_2 and forms very stable calcium silicate in the molten slag, which reduces the activity of silica and the yield of Si in the remelted ingot. The losses of Si in all investigated UHSSs range from 9% to 51% (see Fig. 12). This result is in a good agreement with those obtained by Bandyopadhyay et al. [109], who concluded that ESR leads to some losses in the content of Si ranged from 0 to 55%, and Birol et al. [106], who used slags with different chemical composition which consist mainly of CaF_2–Al_2O_3– CaO ternary systems with a small percentage of MnO, SiO_2, MgO and FeO, and concluded that the losses in the Si content are up to 60% as a result of ESR.

The losses in Si content as a result of ESR seem to decrease with the increases in the Si activity (see Fig. 13(g)). This may be attributed to the lower content of

oxygen resulting from the addition of Al deoxidant during ESR. Fig. 14 illustrates clearly that the losses of oxygen increased with increasing the Al pick up in the remelted ingots, while the losses of Si are decreased.

The increment in the Al content in all remelted steel ingots ranges from 0.016 to 0.051 wt.% as given in Table 5, due to the Al addition as a deoxidant during ESR. The pickup mechanism of Al is not clear. Since Al is added in order to reduce the FeO formed in the molten slag, the excess amount of Al will form an Al-floating layer on the molten slag surface due to the molten Al being of lower density than the molten slag. Then, this layer will be oxidized to Al_2O_3, which indicates that it is very hard for the Al added to enter the molten metal directly.

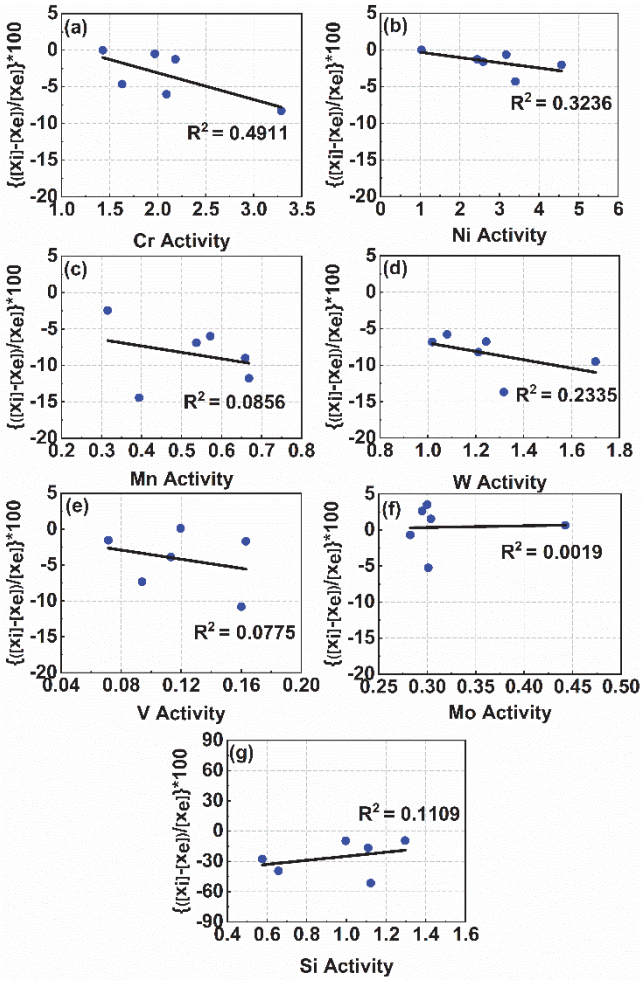

Fig. 13. Influence of the elemental activity on the net change in [Cr], [Ni], [Mn], [W], [V], [Mo] and [Si] (Reprinted [adapted] under CC BY license from Paper I © 2017 Authors and Scientific Research Publishing Inc.).

However, at the slag/metal interface, the presence of elements like Si perhaps reduces some Al_2O_3, which causes a higher amount of Al in the remelted ingot, as illustrated in Fig. 15 and according to the chemical reaction of Eq. (24). The high scattering shown in Fig. 15 and the lower Al content at Si activity 1.12 and 1.11 may be the result of increasing the Al content and its activity in the molten slag, which leads to the chemical reaction of Eq. (24) going backward.

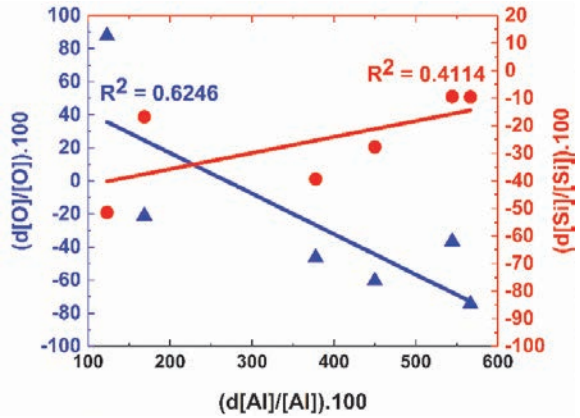

Fig. 14. Influence of Al change, % on the change, % of O and Si (Reprinted [adapted] under CC BY license from Paper I © 2017 Authors and Scientific Research Publishing Inc.).

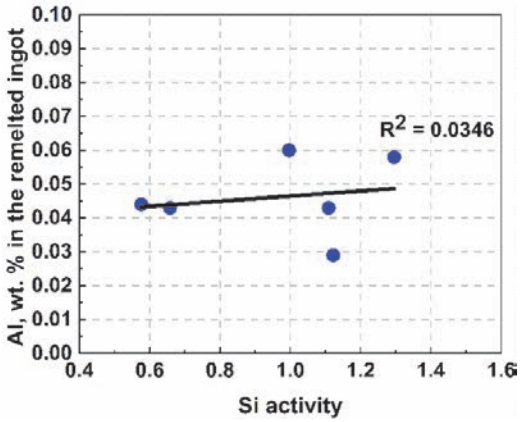

Fig. 15. Influence of Si activity on the Al content, % in the remelted ingot (Reprinted [adapted] under CC BY license from Paper I © 2017 Authors and Scientific Research Publishing Inc.).

The carbon content of the slag is increased by the pre-fusion process, partly because of the carbon paste layer on the bottom and wall of the furnace, and partly because of the graphite electrode used in the submerged EAF. This leads to an increase in the C content of the remelted steel ingots slightly and a corresponding decrease in the C content of the slag during ESR, as can be seen in Table 10.

Table 10. Carbon content in slag before and after ESR (Reprinted [adapted] under CC BY license from Paper I © 2017 Authors and Scientific Research Publishing Inc.).

Slag	C% in fused slag	C% in slag after ESR
#1	0.026	0.012
#2		0.021
#3		0.001
#4		0.001
#5		0.025
#6		0.001

4.1.2 Effect of ESR on the S, P and N contents

In this section, the desulphurization, dephosphorization, and denitrification as a result of ESR will be discussed in detail. The net change, % in the S, P and N contents as a result of ESR, are presented in Fig. 16.

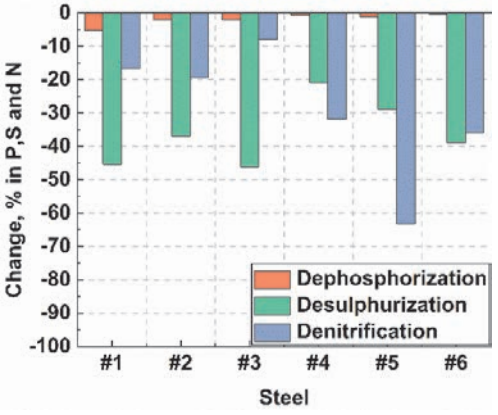

Fig. 16. Change, % in X: S, P and N as a result of ESR (Reprinted [adapted] under CC BY license from Paper I © 2017 Authors and Scientific Research Publishing Inc.).

Desulphurization

It depends on the sulphur activity in the consumable electrode. As shown in Fig. 16, ESR with a slag consisting of 70% CaF_2, 15% CaO and 15% Al_2O_3 has a good desulphurizing power range from 21% to 46% for all investigated UHSSs. These results show good agreement with those obtained by Bandyopadhyay et al. [109],

who concluded that the S content in the metal decreased by up to 30–50% as a result of ESR.

The variation in the degree of desulphurization between the investigated steels may be attributed to the variation in the starting chemical composition of the steels. Based on the interaction coefficient between elements in ternary iron-based alloys, some elements have a positive interaction coefficient, i.e. C, Al, Si, Mo and W, which leads to a decrease in the S activity to move from the molten metal to the molten slag. In contrast, Al and Si have O affinity, which reduces the O partial pressure in the molten metal and leads to improving the S activity to react with the cations forming elements like Ca^{+}, Mn^{+}, etc. These transfer S from the molten metal droplet to the molten slag in the form of CaS, MnS, etc. The desulphurization is improved by increasing the S activity in the molten steel pool, as clearly shown in Fig. 17.

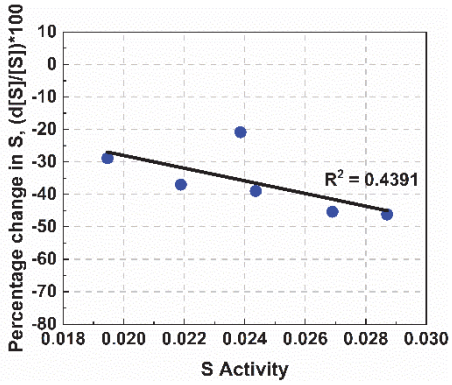

Fig. 17. Influence of S activity on the desulphurization (Reprinted [adapted] under CC BY license from Paper I © 2017 Authors and Scientific Research Publishing Inc.).

Also, the sulphur activity depends on the oxygen activity in the molten steel, as increasing the oxygen activity leads to reducing the sulphur activity and thereby reduces the degree of desulphurization. This can be illustrated by the reaction of Eq. (13).

Table 11 provides the percentage of S removed to the slag and to the atmospheric air and those calculated based on the concentration of S in the remelted ingots and their related slags after ESR. From Table 11, most of the removed S, about 97–99%, was removed as gas by metal-gas and slag-gas interactions and this represents the main desulphurization mechanism. These results are in a good

agreement with those obtained by Mattar [92], who concluded that about 80% of sulphur removal takes place by metal-gas and slag-gas reactions.

Table 11. Removal of S from steel to slag and air (Reprinted [adapted] under CC BY license from Paper I © 2017 Authors and Scientific Research Publishing Inc.).

Steel	S removal from steel [% from total removal]	
	To slag	To air
#1	3.04	96.96
#2	2.86	97.14
#3	2.20	97.80
#4	1.86	98.76
#5	3.75	96.25
#6	1.32	98.68

Dephosphorization

Only up to 5% of P was removed as a result of ESR in all investigated steels. The level of P in the remelted ingots slightly decreased as the activity of P increased, as shown in Fig. 18. The dephosphorization is based on the high partial pressure and activity of oxygen to form phosphorus pentoxide P_2O_5 which can then be moved to the molten slag, but this condition cannot be achieved in the current case. Thus, ESR has a little effect on the dephosphorization for the investigated UHSSs.

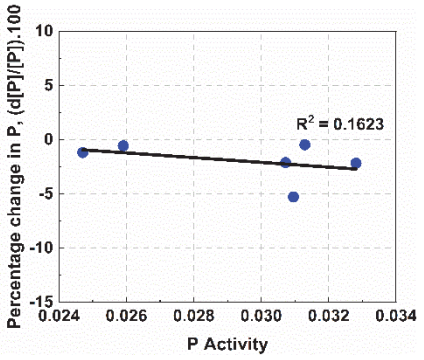

Fig. 18. Influence of P activity on the dephosphorization (Reprinted [adapted] under CC BY license from Paper I © 2017 Authors and Scientific Research Publishing Inc.).

Denitrification

The nitrogen content of the remelted ESR ingot is influenced by many parameters, but the main parameters are the chemical composition of the starting slag and the consumable electrode. In order to understand the denitrification phenomenon, the nitrogen content was determined in the metal and slag before and after ESR (see Table 5 and Table 12).

The nitrogen was removed from the investigated steel by about 8% to 63%, which illustrates clearly that the denitrification can occur during ESR (see Fig. 16). These results are in a good agreement with those obtained by Eissa et al. [110], who investigate the behavior of nitrogen during ESR of Ti-free tool steels and concluded that about 15–67% of the nitrogen content of the consumable electrode was removed by ESR. Ahmed et al. [111] studied the denitrification of AISI M41 tool steel using different slag systems containing the following percentages of CaF_2, CaO and Al_2O_3: 65-15-20, 75-15-10, and 55-30-15. The nitrogen content was decreased by about 82%, 20%, and 31% respectively, which are at the same level as the current results.

The presence of CaO in the slag may be one of the reasons for the denitrification effect of the slag, as it depolymerizes the Al_2O_3 network and increases the concentration of free oxygen ions (O^{2-}) and non-bridging oxygen ions (O^{-}). This increases the transfer of nitrogen to the molten slag in the form of free nitrides (N^{3-}, Eqs. (25) and (26)) and also as non-bridging nitrides (N^{-}, Eq. (27)) according to reactions [112]

$$\frac{1}{2}N_{2\,(g)} + \frac{3}{2}(O^{2-})_{Slag} \leftrightarrow (N^{3-})_{Slag} + \frac{3}{4}O_{2(g)}, \tag{25}$$

$$[N]_{Metal} + \frac{3}{2}(O^{2-})_{Slag} \leftrightarrow (N^{3-})_{Slag} + \frac{3}{2}[O]_{Metal}, \tag{26}$$

and

$$\frac{1}{2}N_{2\,(g)} + 2(O^{-})_{Slag} \leftrightarrow (N^{-})_{Slag} + \frac{1}{2}(O^{2-})_{Slag} + \frac{3}{4}O_{2\,(g)}. \tag{27}$$

The depolymerization effect is assisted by the presence of CaF_2 and this increases the solubility of nitrogen in the molten slag, because fluorine has the ability to liberate both oxygen ions and incorporated nitrides from the Al_2O_3 network [111], [113]–[116].

The removal of nitrogen is influenced by many factors, such as the removal of nitride inclusions by physical removal, floatation, and dissociation, or by the

chemical reaction with the slag phases as illustrated in Eq. (26), or by the chemical reaction with carbon as follows

$$N_{2\,(g)} + (C^{2-})_{Slag} \rightarrow (CN_2^{2-})_{Slag}. \quad (28)$$

The solubility of N can be increased by the presence of traces of TiO_2 where the nitrogen will incorporate into titanate networks. Increasing the Al_2O_3 in the slag during the ESR leads to increasing the slag viscosity and N removal. However, all of these parameters are fixed in this study because they are related to the single slag that was used in this study. However, the difference in the degree of denitrification exists and it varies with the change in steel composition, so the chemical composition of the consumable electrode is also an important parameter. Shuang et al. [116] stated that the denitrification is affected by the alloying elements and impurities contained in the consumable electrode.

The solubility of nitrogen in steel varies by changing the elemental composition of steel, as some elements like C, Si, Ni, Al, Cu and O have negative effect on the nitrogen solubility, while other elements like Cr, W, Mn, Mo and V have a positive effect on the solubility of nitrogen, which reduces the denitrification. The main factors controlling the absorption site fraction in the molten metal are the content of the impurities sulphur and oxygen, both of which are more strongly surface active than nitrogen. Both elements are expected to alter the energy of nitrogen adsorption by increasing the activity of vacant sites at the surface of metal [114].

Table 12. Nitrogen content in slag before and after ESR and sources of increment [Paper I].

Heat No.	N content [wt.%]		Source of increment [% from total increment]	
	In fused slag	In slag after ESR	From steel	From air
#1	0.017	0.034	77.50	22.50
#2		0.043	68.67	31.33
#3		0.040	54.95	45.05
#4		0.057	85.71	13.94
#5		0.071	90.19	9.81
#6		0.053	98.32	1.68

Fig. 19 shows that the denitrification degree for the investigated UHSSs as a result of ESR increases with increasing the activity of nitrogen in the molten metal.

Based on the content of N of the investigated steels and slag before and after ESR, the N sources were calculated and given in Table 12. These results illustrate

that the lower solubility of the atmospheric N in the slag protects the molten metal against N pick-up significantly.

Fig. 20 illustrates the presence of a strong correlation between the denitrification and the activity of S of the current investigated steels. This is based on the effect of S on the denitrification kinetics through its tendency to segregate to surfaces.

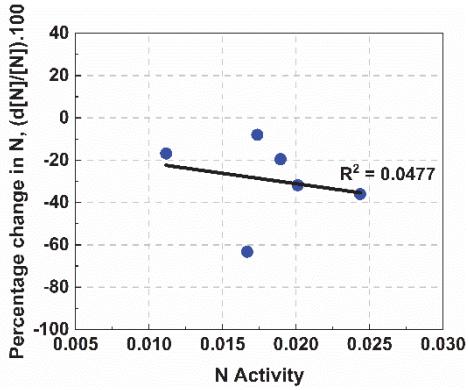

Fig. 19. Influence of N activity on the denitrification (Reprinted [adapted] under CC BY license from Paper I © 2017 Authors and Scientific Research Publishing Inc.).

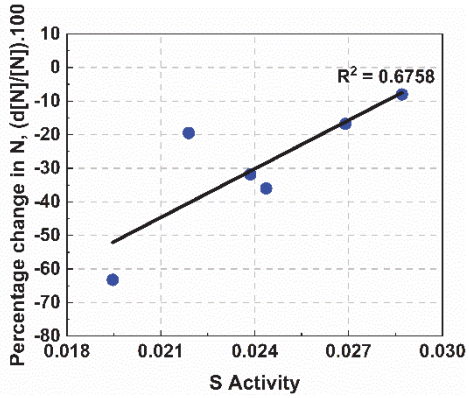

Fig. 20. Relationship between S activity and denitrification (Reprinted [adapted] under CC BY license from Paper I © 2017 Authors and Scientific Research Publishing Inc.).

4.2 Effect of ESR on NMIs

In Papers II and III, the influence of ESR on the NMIs in terms of their types, sizes, numbers and area fractions was investigated in detail, and the main results are provided in this section.

4.2.1 Size and frequency of NMIs

SEM micrographs shown in Fig. 21 give a general impression about the degree of cleanliness of steels #1, #2, #3 and #4 processed without and with ESR. For the quantitative analysis of NMIs using LSCM, thirty LSCM images per steel covering a total area of 44 mm^2 were used. In the case of quantitative analysis of NMIs using SEM, 122 fields covering a total area 7.3 mm^2 were investigated. Fig. 22 and Fig. 23 show the number per mm^2 and area percentages of NMIs in steels #1, #2, #3 and #4 without and with ESR.

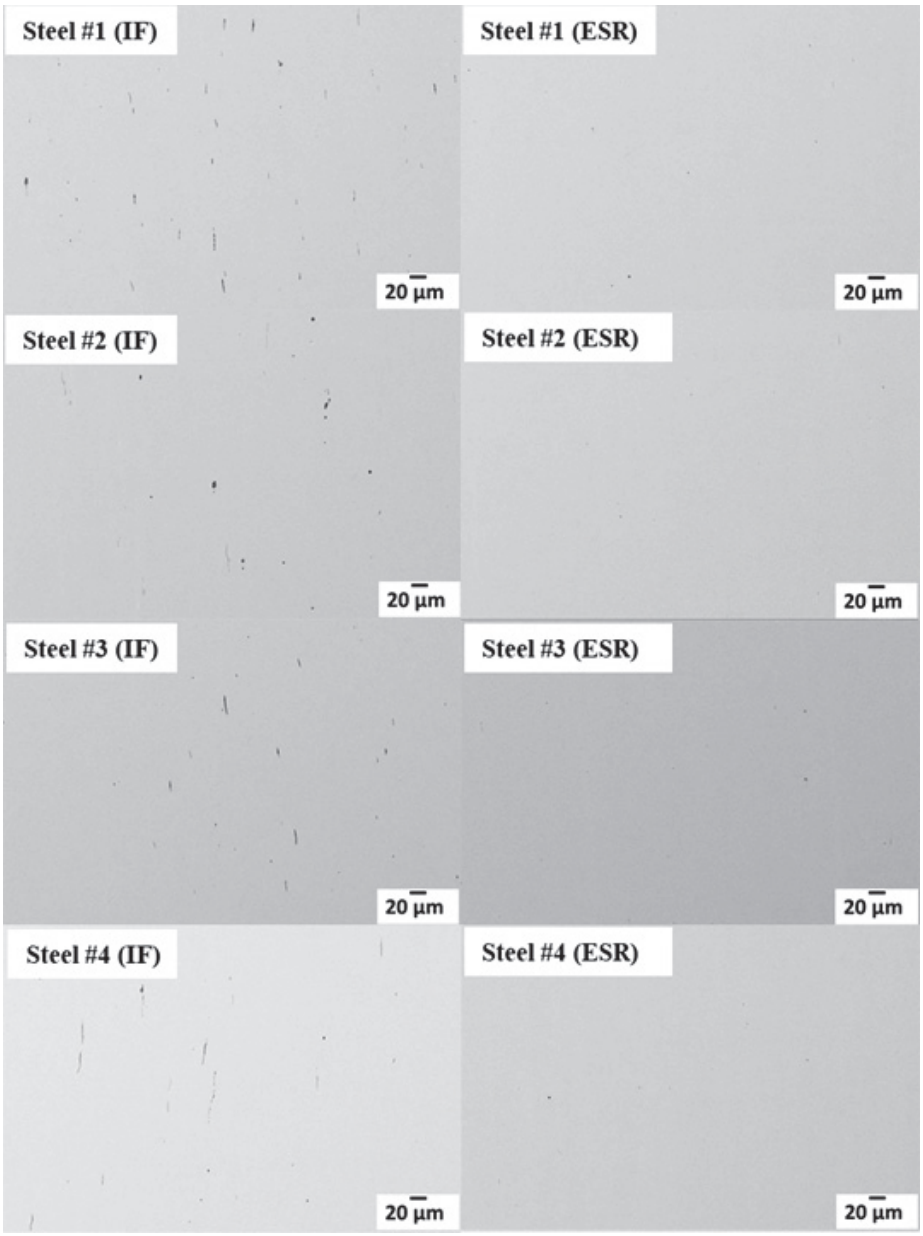

Fig. 21. SEM micrograph of NMIs in steels #1, #2, #3 and #4 without and with ESR (Reprinted [adapted] by permission from Paper II © 2018 Trans Tech Publications and from Paper III © 2019 Authors).

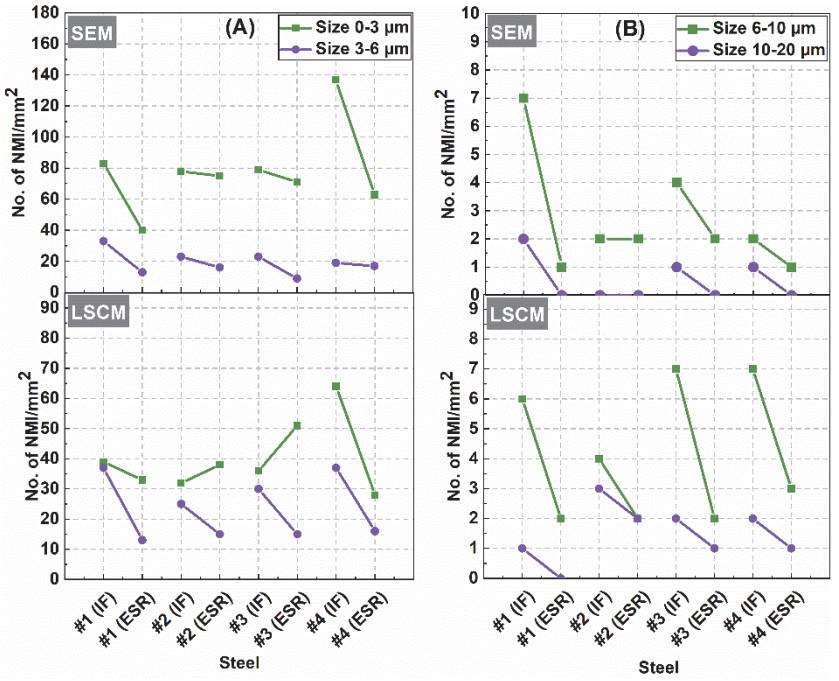

Fig. 22. Number of NMIs per mm^2 in steels #1, #2, #3 and #4 without and with ESR. Results from SEM and LSCM investigations; (A): size ranges 0–3 µm and 3–6 µm; (B): size ranges 6–10 µm and 10–20 µm (Reprinted [adapted] by permission from Paper II © 2018 Trans Tech Publications and Paper III © 2019 Authors).

From the LSCM results, ESR decreased the total number of NMIs in the steels #1, #2, #3 and #4 by 43%, 13%, 6% and 57% respectively. About 94% of the NMIs in the remelted ingots, compared with about 90% in the consumable electrode, have ECD smaller than 6 µm, which have a small effect on the properties of steel and can be avoided in compliance with the standard DIN 50 602 [117]. In Fig. 22, for steels #1, #2, #3 and #4, ESR decreased the number of NMIs per mm^2 in all size ranges except the number of NMIs per mm^2 in size range 0–3 µm in steels #2 and #3. The latter case is attributed to the dissociation and erosion of larger NMIs and the re-generation of new smaller ones, in addition to the slight changes in the level of impurities and alloying elements that form the inclusions, as discussed below. The area percentage of NMIs in all size ranges decreased as a result of ESR in steels #1, #2, #3 and #4, except in the size range 0–3 µm in steels #1, #2 and #3 (see Fig. 23).

From the FESEM results, ESR decreased the total number of NMIs in steels #1, #2, #3 and #4 by 55%, 7%, 19% and 62% respectively. About 98% of the NMIs in the remelted ingots, compared with about 96% in the consumable electrode, have ECD smaller than 6 µm. As shown in Fig. 22, in steels #1, #2, #3 and #4, ESR decreased the number of NMIs per mm^2 in all size ranges except in the size range of 6-10 µm in steel #2. Fig. 23 illustrates the reduction of the area % of NMIs in steels #1, #2, #3 and #4 in all size ranges as a result of ESR, except in the size range 0–3 µm in steel #2.

Comparing the results obtained from LSCM and FESEM, there are slight differences between the two analytical techniques, which is attributed to the variation in the total investigated area (44 vs. 7 mm^2): it was much easier to study large areas with LSCM but, due to its better resolution, the FESEM was better at revealing small inclusions.

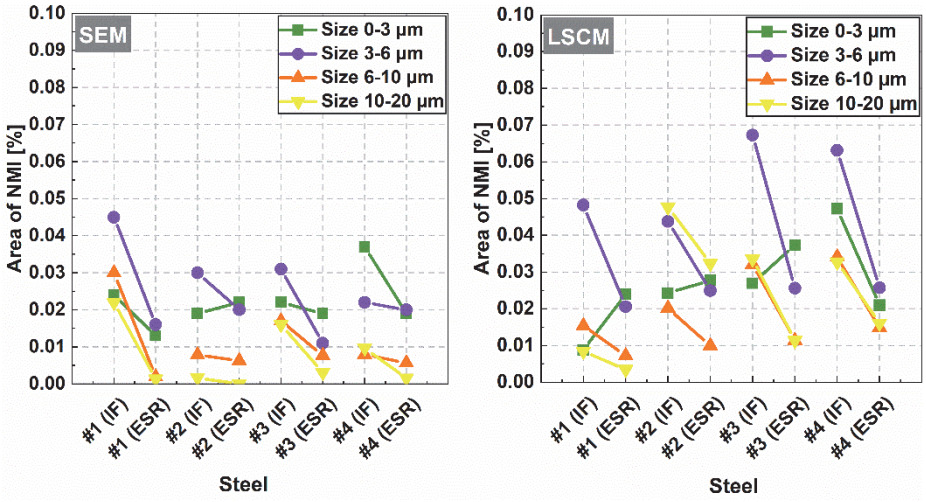

Fig. 23. FESEM and LSCM data on area percentages of NMIs without and with ESR (Reprinted [adapted] by permission from Paper II © 2018 Trans Tech Publications and Paper III © 2019 Authors).

From the total impurity level (TIL% = S% + N% + O%), NMI area percentages and number densities, the degree of refining as a result of ESR changed slightly by the steel composition, as illustrated from Fig. 24. Based on the number density and area fraction of NMIs, it can be concluded from Fig. 24 that steels #1 and #4 have the best degree of refining, followed by steel #3, and then steel #2. Fig. 24 shows

clearly that removing a small number of NMIs by ESR led to a large reduction in the area fraction of NMIs, which means that the removed NMIs were large ones.

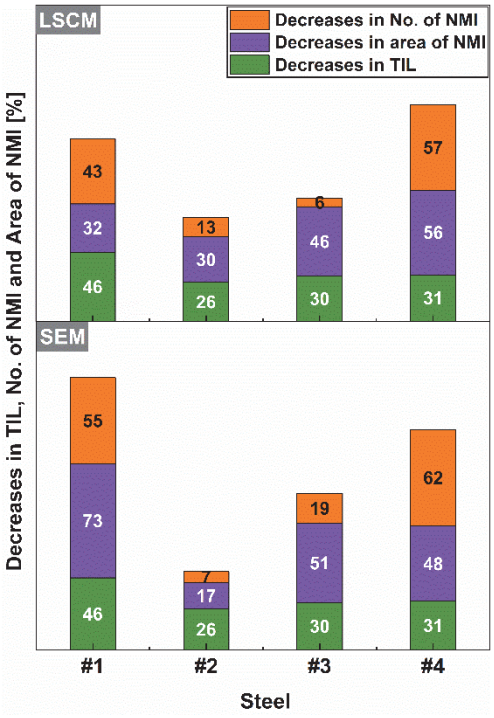

Fig. 24. Reductions, % in total impurity level, No. of NMIs and area percentage of NMIs as a result of ESR [Paper II], [Paper III] (Reprinted [adapted] by permission from Paper III © 2019 Authors).

4.2.2 Chemical composition of NMIs

In steels #1, #2, #3 and #4, the NMIs can be divided into four major categories: oxides, sulphides, nitrides and complex multiphase inclusions. Their number densities, maximum ECDs and area % are given in Fig. 25 and Fig. 26. There is a large variation in the distribution of the NMIs among the four categories as a result of ESR (see Fig. 25). This is attributed to the chemical reactions between the molten slag and the steels with different chemical compositions and level of impurities.

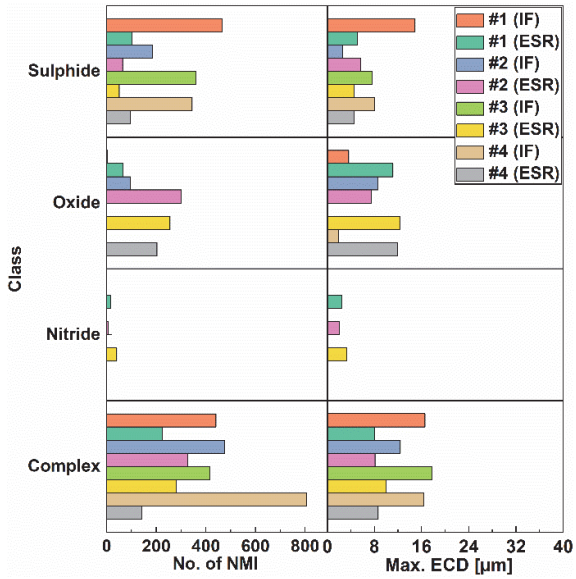

Fig. 25. Number of NMIs and maximum ECD of each class of NMI without and with ESR [Paper II], [Paper III] (Reprinted [adapted] by permission from Paper III © 2019 Authors).

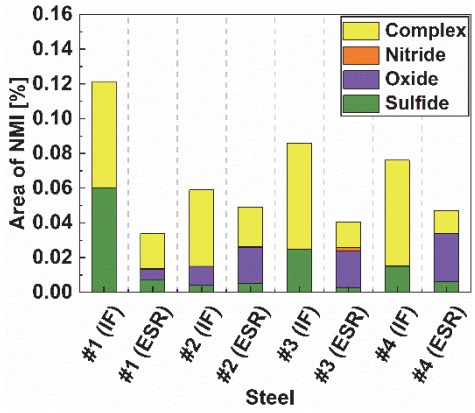

Fig. 26. Area fractions of each class of NMIs without and with ESR [Paper II], [Paper III] (Reprinted [adapted] by permission from Paper III © 2019 Authors).

As illustrated from Fig. 25 and Fig. 26, in steels #1, #2, #3 and #4, ESR led to a decrease in the total area %, number densities and maximum sizes of all complex inclusions by dissolution of all NMIs and re-generation of new smaller ones. In addition, the area %, numbers, and maximum sizes of all sulphides are decreased

significantly in steels #1, #2, #3 and #4. During ESR, some nitrides with small area %, number densities and maximum ECDs are precipitated in steels #1, #2 and #3. The dissolution possibility of NMIs increased with increasing the temperature of the molten slag [117]. So, as a result of ESR, the number densities and area % of oxides are increased due to the dissociation and dissolution of complex inclusions and the precipitation of fine oxides as a result of Al addition as deoxidant during ESR.

The NMIs behavior during ESR is governed by different interfaces existing during the process, like the slag-air, slag-electrode, slag-droplet, and slag-metal pool interfaces as shown in Fig. 27(a). The most important position during the ESR is the slag-electrode interface, with most of the NMIs removed there [118]. Details about the chemical compositions of the NMIs and their number densities, area %, and maximum sizes without and with ESR are given in Figs. 28, 30, 32 and 34.

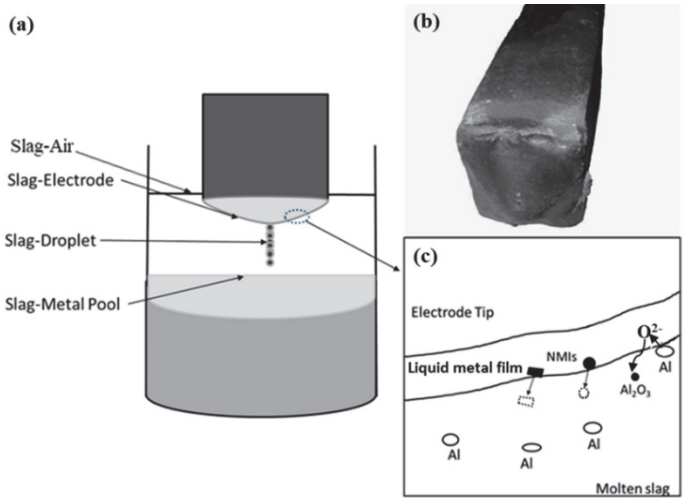

Fig. 27. a) Schematic diagram showing the interfaces in the ESR. b) Actual electrode tip and liquid metal film formed during ESR for one of the investigated steels. c) Dissolution of NMIs (rectangles and circles) and Al deoxidation at the liquid metal film formed on the tip of the electrode (Under CC BY-SA license from Paper III © 2019 Authors).

In the case of steel #1, without ESR, the NMIs are sulphides, i.e. MnS and (Mn,Ti)S; pure oxides, i.e. Al_2O_3 and complex NMIs, i.e. (Al_2O_3.SiO_2), (MnO.Al_2O_3.SiO_2), (MnO.SiO_2), (CaO.MnO.Al_2O_3.SiO_2), (MnS.Al_2O_3.SiO_2), (MnS.Al_2O_3), (MnOS), (MnS. CaO. Al_2O_3.SiO_2); and (MnS.SiO_2). Most of MnS, which is harmful on the ductility and toughness properties of steel, are dissolved during the ESR at the slag-

electrode interface during the formation of metal droplets from the liquid metal film. Then S is removed according to Eqs. (13) and (14). The number and area % of MnS are decreased as a result of ESR by about 78% and 88% respectively, while the maximum ECD is decreased from 15 to 5 µm.

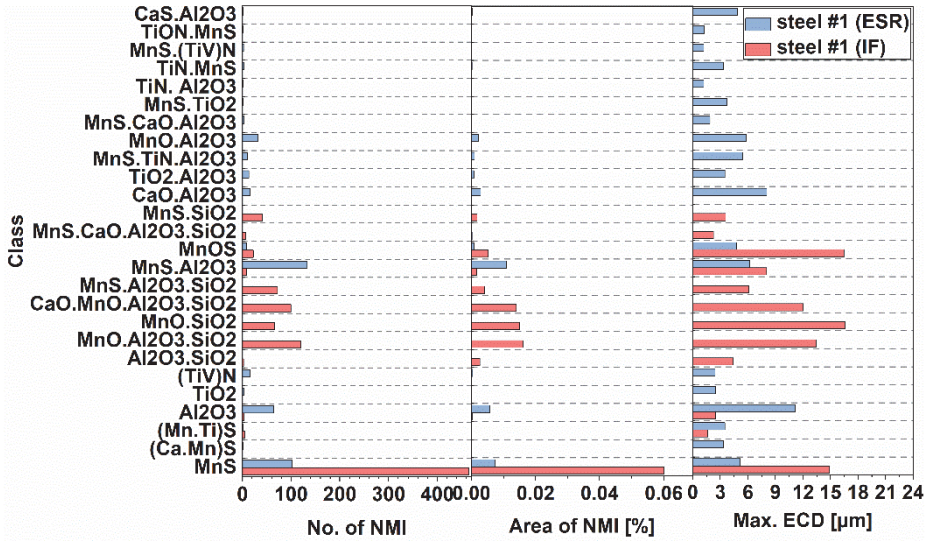

Fig. 28. Chemical compositions, numbers, area %, and maximum sizes of NMIs without and with ESR for steel #1 (Reprinted [adapted] by permission from Paper III © 2019 Authors).

Sulphides start to nucleate and grow during the solidification on some of the existing oxide or nitride inclusions, forming multiphase inclusions with an oxide or nitride core surrounded by a shell of sulphide, i.e. ($MnS.Al_2O_3$), ($MnS.TiN.Al_2O_3$) as shown in Fig. 29(a) and (b). Other complex NMIs that were observed in small number, area % and maximum ECDs are ($MnS.CaO.Al_2O_3$), ($MnS.TiO_2$), (MnS. TiN), (MnS. (TiV)N) and (MnS.TiON). Several studies [119]–[121] reported about the precipitation of sulphide inclusions on oxides. Kim et al. [122] reported that raising the CR decreases the occurrence of MnS precipitation on oxides. Some MnOS inclusions were re-precipitated during ESR with small number, diameter, and area %. In addition, some sulphides were modified by Ca, i.e. forming (Ca. Mn) S and ($CaS.Al_2O_3$).

During ESR, CaO formed as a result of the chemical reactions between CaF_2 and Al_2O_3 as shown by reaction

$$3CaF_2 + Al_2O_3 \rightarrow 3CaO + 2AlF_{3\,(g)}. \quad (29)$$

Then it reacted with Al_2O_3, forming xCaO.$y$$Al_2O_3$ inclusions according to reaction

$$x\mathrm{CaO} + y\mathrm{Al_2O_3} \rightarrow x\mathrm{CaO}.\,y\mathrm{Al_2O_3}. \quad (30)$$

The later inclusions are softer and have a lower melting temperature than Al_2O_3 [89], [93].

During ESR, the traces of Ti in the consumable electrode and the small amount of TiO_2 in the range of 0.13–0.15 wt.% in the molten slag led to the formation of TiO_2.Al_2O_3.MnS. Furthermore, the strong affinity of Ti and V to N led to the precipitation of (TiV)N inclusions. At high temperature of slag (1700–2000 °C) [123], addition of Al led to the reduction of TiO_2 through an exothermic aluminothermic reduction reaction [124], [125]

$$4[Al] + 3(TiO_2) \leftrightarrow 3[Ti] + 2(Al_2O_3). \quad (31)$$

Subsequently, once the Ti enters the molten metal pool, some Ti containing inclusions are formed, i.e. TiO_2, TiN and (TiV)N, and this clarifies the existence of these inclusions in the ESR materials and absence from the IF materials.

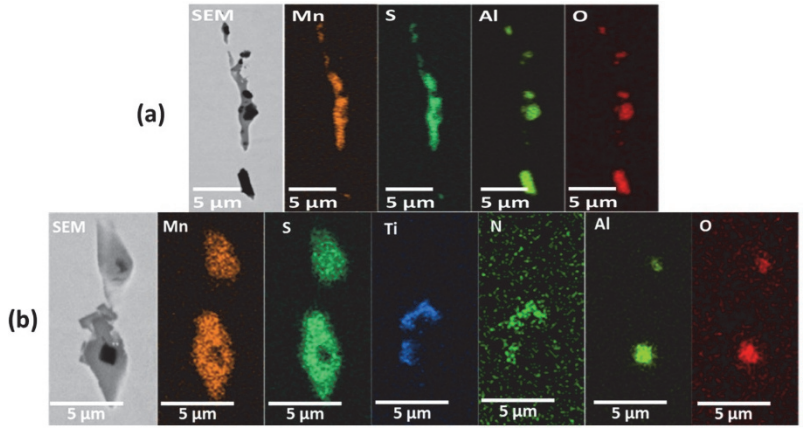

Fig. 29. EDS maps of deformed inclusions in steel #1: (a) MnS.Al_2O_3 (b) MnS.TiN. Al_2O_3 (Reprinted [adapted] by permission from Paper III © 2019 Authors).

The hard and large oxides inclusions with large area fractions in the consumable electrode of steel #1, such as (Al_2O_3.SiO_2), (MnO.Al_2O_3.SiO_2), (MnO.SiO_2),

($CaO.MnO.Al_2O_3.SiO_2$), ($MnS.Al_2O_3.SiO_2$), and ($MnS.SiO_2$), were removed completely by dissolution [87], [117], [126], [127] during the formation of the molten metal droplet at the tip of the electrode, due to the high temperature. Then, the dissolved elements transformed to other modified inclusions during cooling and solidification, characterized by their lower melting point, such as $xCaO.yAl_2O_3$. This is in a good agreement with those obtained by several other studies [128]–[133] that have illustrated that most of the oxide inclusions in the consumable electrode are removed before the molten metal droplets reach the molten metal pool. The chemical composition of the NMIs in the remelted ingots, that are totally different from the NMIs in the consumable electrode, verify this dissolution mechanism. During the ESR, a continuous chemical reaction between slag and oxygen in the air occurs at the slag-air interface. Oxidation also occurs at the liquid molten film that forms on the electrode tip. During ESR, to protect the molten steel from the atmospheric oxygen and decrease the formation of iron oxide, Al deoxidant was added to the molten slag to combine with oxygen according to the following chemical reactions.

Reaction of added aluminium metal with atmospheric oxygen is described by

$$2[\mathrm{Al}]_{in\ slag} + 3[\mathrm{O}] \rightarrow (\mathrm{Al_2O_3}). \quad (32)$$

Reduction of iron oxide in the liquid metal film is described by

$$2[\mathrm{Al}]_{in\ slag} + 3(\mathrm{FeO}) \rightarrow (\mathrm{Al_2O_3}) + 3[\mathrm{Fe}]. \quad (33)$$

Table 5 reveals that ESR increased Al concentrations. Wang et al. [134] found that after addition of Al during P-ESR, the cleanliness of H13 ingots enhanced as a result of reducing the number and size of NMIs. Complex $CaO.MnO.Al_2O_3.SiO_2$ inclusions in the consumable electrode were transformed into Al_2O_3 particles in the produced P-ESR ingot. The results are in a good agreement with those obtained by Zuzek et al. [135], who reported that ESR of 51CrV4 spring steel made by traditional continuous casting reduced the concentration of impurities such as S and P and some alloying elements, but it led to an increase in the concentration of Al from 0.006% to 0.025% and the formation of some Al_2O_3 inclusions in the remelted ingot. Also, Shi et al. [136] concluded that in the consumable electrode of die steel, the NMIs divided into large (MnCr)S and complex inclusions with Al_2O_3 cores surrounded by (MnCr)S. ESR removed all these inclusions except pure Al_2O_3 particles, approximately 1 μm in size. Such results are consistent with those of Dong et al. [93], who concluded that Al_2O_3 is the main NMI found in die steel after ESR using slag with the composition of 70% CaF_2 and 30% Al_2O_3.

During ESR, some newly formed NMIs are removed through flotation to the metal-slag interface, and then absorbed by the molten slag, but this depends mainly on the size of NMI and the flotation velocity, which should be higher than the speed of the solidification front [128]. As discussed in the current study, not all the large NMIs are extracted by flotation, despite their higher flotation velocities.

In the case of steel #2 (Fig. 30), it can be seen that ESR led to removing some NMIs types completely, such as (Cr_2O_3), (CaO), ($CaO.MnO.Al_2O_3.SiO_2$), ($MnS.Al_2O_3.SiO_2$), ($MnS.CaO.Al_2O_3.SiO_2$), ($CaO.Al_2O_3.SiO_2$), and ($CaO.MnO.Al_2O_3$). One possibility is the conversion of these inclusions to other modified inclusions with lower melting points, like xCaO.$y$$Al_2O_3$. Also, some inclusions are decreased, like MnS, and others are modified, like ((Ca,Mn)S), ($CaS.Al_2O_3$) and ((Mn,Ti)S), while other inclusions are increased slightly, like ($MnO.Al_2O_3$), ($CaO.Al_2O_3$) and ($MnS.Al_2O_3$), as a result of the dissolution of the complex NMIs. Different types of inclusions with small fractions are formed as a result of ESR, like (TiO_2), ((TiV)N), ($MnS.TiN.Al_2O_3$), ($Al_2O_3.TiO_2$), ($Al_2O_3.TiN$), (MnS.(TiV)N) and (TiON.MnS). An EDS mapping of ($CaO.Al_2O_3$) and ($MnS.Al_2O_3$) inclusions is given in Fig. 31.

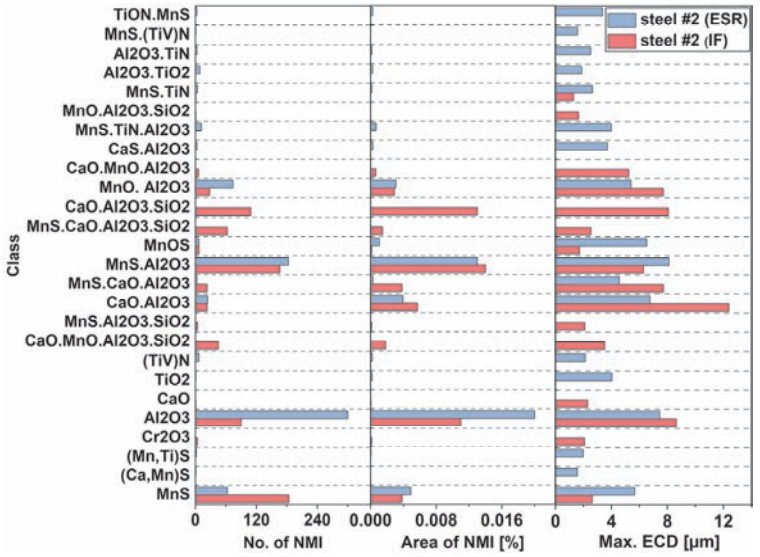

Fig. 30. Chemical compositions, numbers, area %, and maximum sizes of NMIs without and with ESR for 1100901steel #2 (Reprinted [adapted] by permission from Paper II © 2018 Trans Tech Publications).

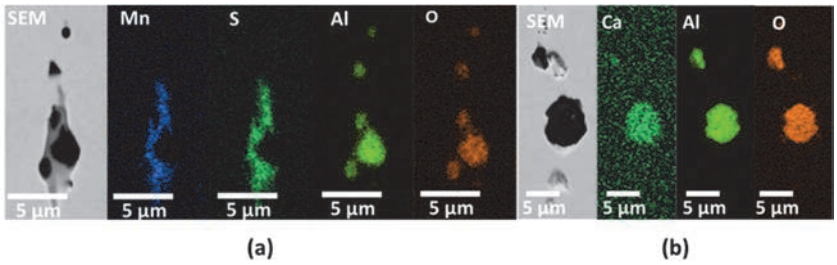

Fig. 31. EDS mapping of (a) deformed $MnS.Al_2O_3$ inclusion (b) $xCaO.yAl_2O_3$ inclusion (Reprinted by permission from Paper II © 2018 Trans Tech Publications).

In steel #3 (Fig. 32), ESR led to removing the following NMIs completely: ($MnO.Al_2O_3.SiO_2$), ($CaO.MnO.Al_2O_3.SiO_2$), ($MnS.Al_2O_3.SiO_2$) and ($MnS.SiO_2$). Also, the number, area fraction and maximum diameter of MnS inclusions decreased sharply as a result of ESR. However, some of the MnS inclusions are modified to (CaMn)S, (MnTi)S and some are reprecipitated on oxides or nitrides as ($MnS.Al_2O_3$), (MnS.CaO), (MnS.TiN), (MnS.TiVN) and (MnS.TiON). Fig. 33 shows EDS mapping of the largest Al_2O_3 and ($MnS.Al_2O_3$) encountered.

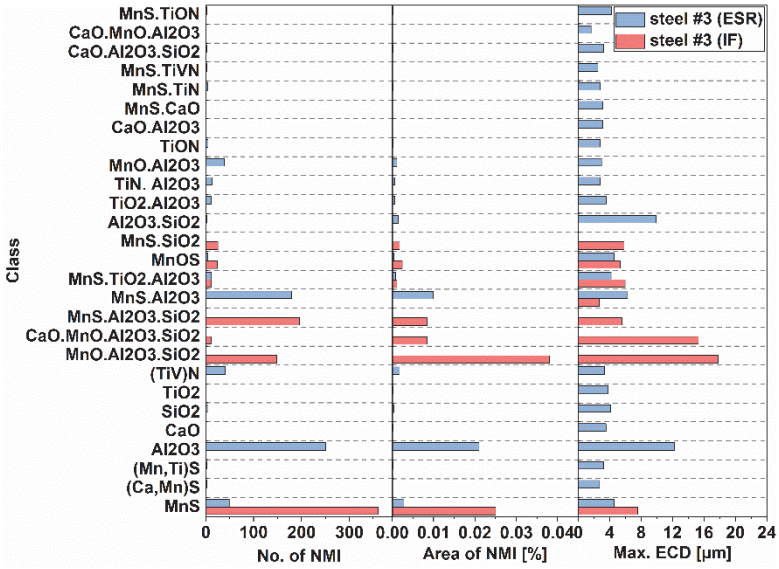

Fig. 32. Chemical compositions, numbers, area percentages, and maximum sizes of NMIs without and with ESR for steel #3 (Reprinted [adapted] by permission from Paper III © 2019 Authors).

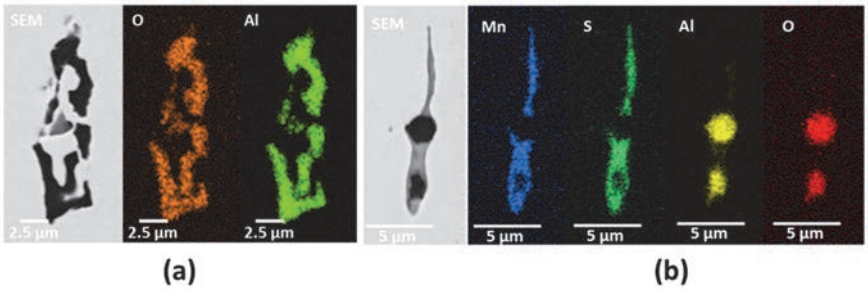

Fig. 33. EDS maps of deformed inclusions: (a) Al_2O_3 (b) $MnS.Al_2O_3$ (Under CC BY-SA license from Paper III © 2019 Authors).

In addition, ESR led to generating other NMIs in small numbers and area fractions like (CaO), (SiO_2), (TiO_2), (TiV)N, ($Al_2O_3.SiO_2$), ($TiO_2.Al_2O_3$), ($TiV.Al_2O_3$), ($MnO.Al_2O_3$), (TiON) and modifying other NMIs like ($CaO.Al_2O_3$), ($CaO.Al_2O_3.SiO_2$) and ($CaO.MnO.Al_2O_3$).

In steel #4 (Fig. 34), ESR led to removing most of the complex NMIs completely, like ($Al_2O_3.SiO_2$), ($MnO.Al_2O_3.SiO_2$), ($MnO.SiO_2$), ($MnS.Al_2O_3.SiO_2$), ($MnS.TiO_2.Al_2O_3$), ($MnS.SiO_2$), while it decreased the number, area fraction and maximum diameter of MnS sharply. Other NMIs are generated as a result of ESR in very small number and area fractions like ((MnTi)S), (NiO), (CaO), ($CaO.Al_2O_3$), (MnS. $CaO.Al_2O_3$), ($MnS.Al_2O_3$), ($MnO.Al_2O_3$), (TiN.MnS), (CaOS), ($MnS.TiO_2$), (MnS.CaO), ($TiO_2.Al_2O_3$), and ($MnS.CaO.Al_2O_3.SiO_2$).

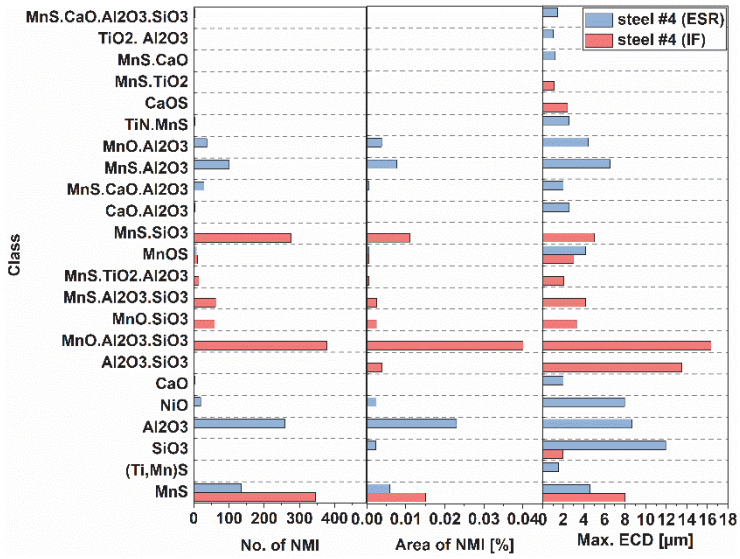

Fig. 34. Chemical compositions, numbers, area percentages, and maximum sizes of NMIs without and with ESR for steel #4 (Reprinted [adapted] by permission from Paper III © 2019 Authors).

4.2.3 Thermodynamic calculations for NMIs

Thermodynamic calculations were used to study the spontaneous behavior of the chemical reaction given in Eq. (31) for steels #1, #3 and #4. Fig. 35 illustrates the influence of Al and Ti activities at 1800 °C, in which the used value of the standard Gibbs free energy of the reaction, ΔG^0 (31), was −305335 J/mol, which was given by the software HSC Chemistry [137] version 9.6.1.

In Fig. 35, the black line represents the boundary in which the chemical reactions given in Eq. (31) are in equilibrium at 1800 °C. It is calculated based on the assumptions that TiO_2 and Al_2O_3 are pure substances, i.e. their activities are unity. This is the case where Al_2O_3 and TiO_2 exist in their own stoichiometric phases within the steel system, e.g. as inclusions. On the left side of this line, the chemical reaction in Eq. (31) is spontaneous from left to right, i.e. Al reacts with TiO_2 to produce Ti and Al_2O_3, and vice versa to the right side of the line.

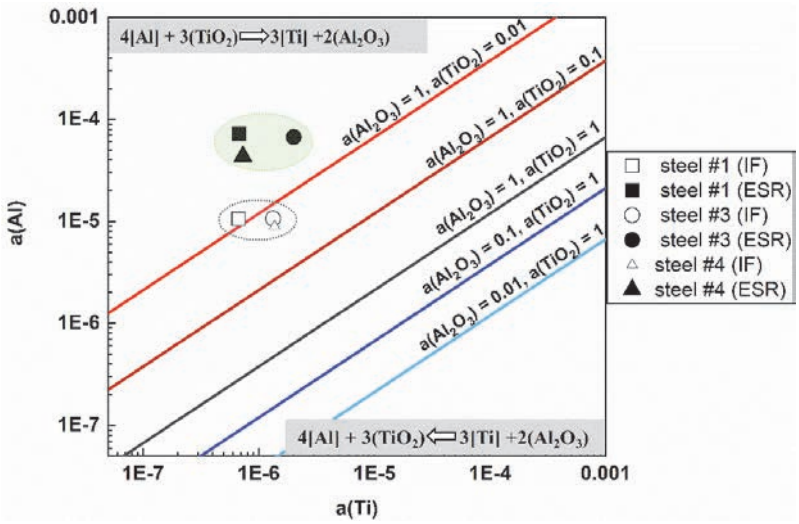

Fig. 35. Equilibrium of reaction (31) at 1800 °C as a function of the activities of aluminium and titanium and their oxides. In the top left-hand corner, reaction presented by Eq. (31) goes left to right, while in the bottom right-hand corner it goes from right to left (Reprinted [adapted] by permission from Paper III © 2019 Authors).

Decreasing the activity of TiO_2 (red lines in Fig. 35) transfers the boundary to the left. In comparison, reducing the activity of Al_2O_3 (blue lines in Fig. 35) transfers the boundary more to the right. Also, the activities of Al and Ti in the molten steel at 1800 °C for steels #1, #3 and #4 without and with ESR are given in Fig. 35. They were calculated using FactSage version 7.2 and its FSstel database. In Fig. 35, the activities of Al and Ti are in the region in which the chemical reaction in Eq. (31) must happen spontaneously from left to right. The available software did not allow to calculate the slag-steel equilibria because the software could not be used for slags with high CaF_2 contents. However, using FactSage 7.2 [138] with various databases (FSstel, FToxid and FactPS), it was possible to calculate the expected NMI compositions based on the chemical compositions of the steels #1, #3 and #4 without and with ESR, as shown in Fig. 36.

The thermodynamic calculation results in all cases presented in Fig. 36 show a good agreement with the experimental results given above. As a result of ESR, the predicted quantity and types of NMIs should be reduced due to small change in the chemical composition discussed above.

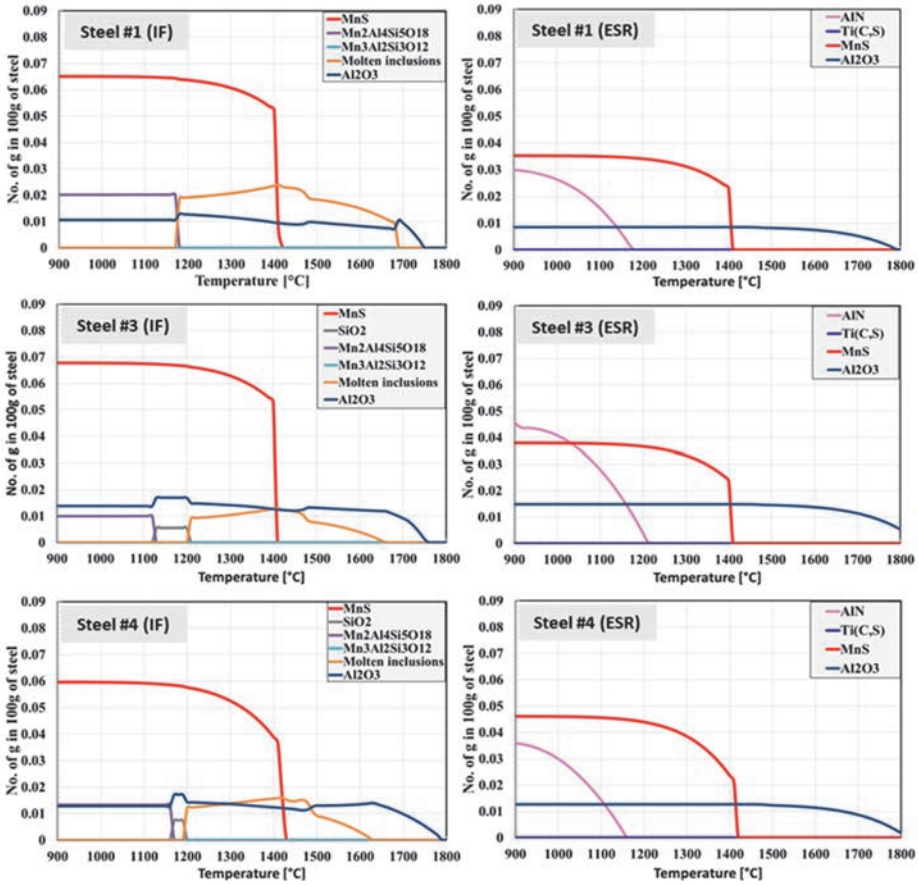

Fig. 36. Thermodynamic calculations of the expected NMIs in steels #1, #3 and #4 without and with ESR (Reprinted [adapted] by permission from Paper III © 2019 Authors).

However, after ESR, there is a slight difference in the chemical composition of some of the predicted NMIs from the observed NMIs, e.g. AlN and Ti(CS), which were predicted thermodynamically but are not observed experimentally. This is because of omitting the slag from the calculations. During the ESR, because of the high affinity of Al to oxygen, most of the added Al is consumed by the oxygen found in the molten slag to form Al_2O_3 in the molten steel. Therefore, TiN was formed due to high availability of N. During solidification, some MnS were precipitates on the existing oxides or nitrides inclusions, e.g. Al_2O_3 and TiN forming multiphase inclusions like MnS.Al_2O_3 and TiN.MnS. Fig. 36 illustrates the large reduction in the mass fraction of MnS inclusions, which represent the main

NMIs in the consumable electrode as a result of ESR. Some predicted NMIs like (TiO_2), ($MnO.Al_2O_3$), ($MnO.Al_2O_3.SiO_2$) and molten inclusions are removed completely as a result of ESR. The term of molten inclusions refers to inclusions found in the molten state at the temperatures of calculation. They have a high percentage of Mn, Al, Si and O with other impurities, e.g. S and light element e.g. Ti. Their chemical compositions changed considerably with temperature. Therefore, it is best to call them molten inclusions without exact stochiometric chemical compositions.

4.3 Construction of CCT diagrams

From Paper VI, this section is concerned with construction of CCT diagrams for two selected steel compositions with ESR (steels #1 and #2), and, also, studying the effect of steel compositions on the CCT diagram. The construction of CCT diagrams (given in Fig. 37) was based on the dilatation curves, final microstructure, and micro- and macro-hardness values.

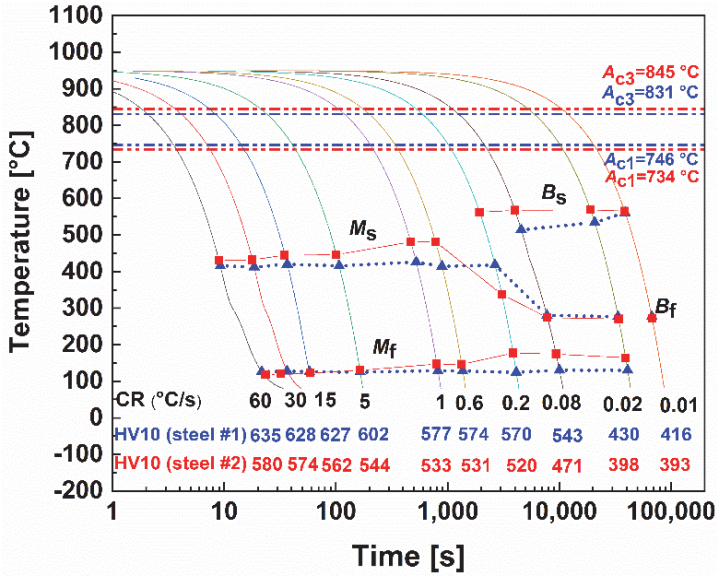

Fig. 37. CCT diagram for steels #1 and #2. A_{c1} and A_{c3}: critical transformation temperatures; M_s and M_f: martensite start and finish transformation temperatures; B_s and B_f: bainite start and finish transformation temperatures (Reprinted [adapted] under CC BY license from Paper VI © 2019 Authors).

Increasing Cr/Ni ratio and the slight increase in the C content in the case of steel #1 compared to steel #2 led to an increase in A_{c1} while A_{c3}, M_s and B_s are decreased (see Fig. 37). These also increase the hardenability of steel #1, which provides higher hardness values for steel #1 (635–416 HV) as compared to those of steel #2 (580–393 HV). The higher hardenability is associated with a decrease in the transformation temperatures, which resulted in microstructure refinement. Fig. 38 and Fig. 39 show the final microstructures after phase transformation for steels #1 and #2 at various CRs ranges from 60 to 0.01 °C/s.

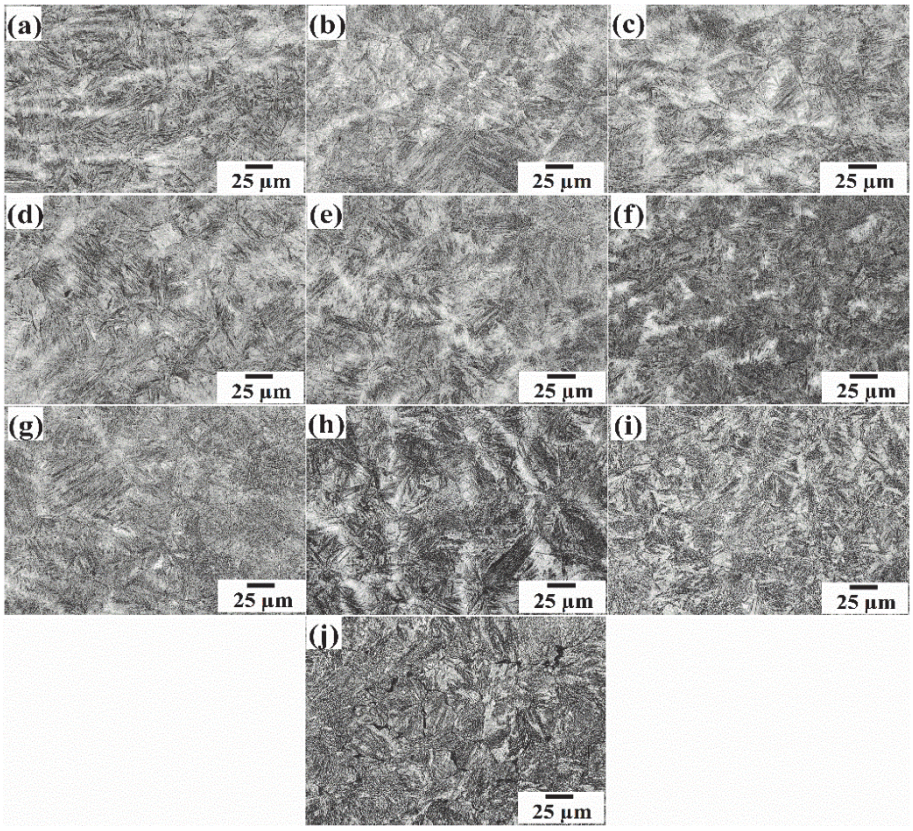

Fig. 38. LSCM micrographs of steel #1 with cooling rates of 60 (a), 30 (b), 15 (c), 5 (d), 1 (e), 0.6 (f), 0.2 (g), 0.08 (h), 0.02 (i) and 0.01 °C/s (j), respectively (Under CC BY license from Paper VI © 2019 Authors).

In the case of steel #1, over a wide range of CRs from 60 to 0.2 °C/s, the microstructure consists of martensite with hardness values ranging from 635 to 570

HV, while the CRs ranging from 0.08 to 0.02 °C/s provide a mixture of martensite and bainite with hardness ranging from 543 to 430 HV. However, at 0.01 °C/s, the microstructure consists mainly of granular bainite with hardness value 416 HV in addition to some carbides formed at the prior austenite grain boundaries, as shown in Fig. 38(j). Steel #2 provided the same transformation products but with some variation, as bainite started to form at the CR of 0.2 °C/s instead of 0.08 °C/s in steel #1 as a result of its lower C and Cr/Ni ratio, which lowered the hardenability and shifted the bainite transformation curve to a higher CR.

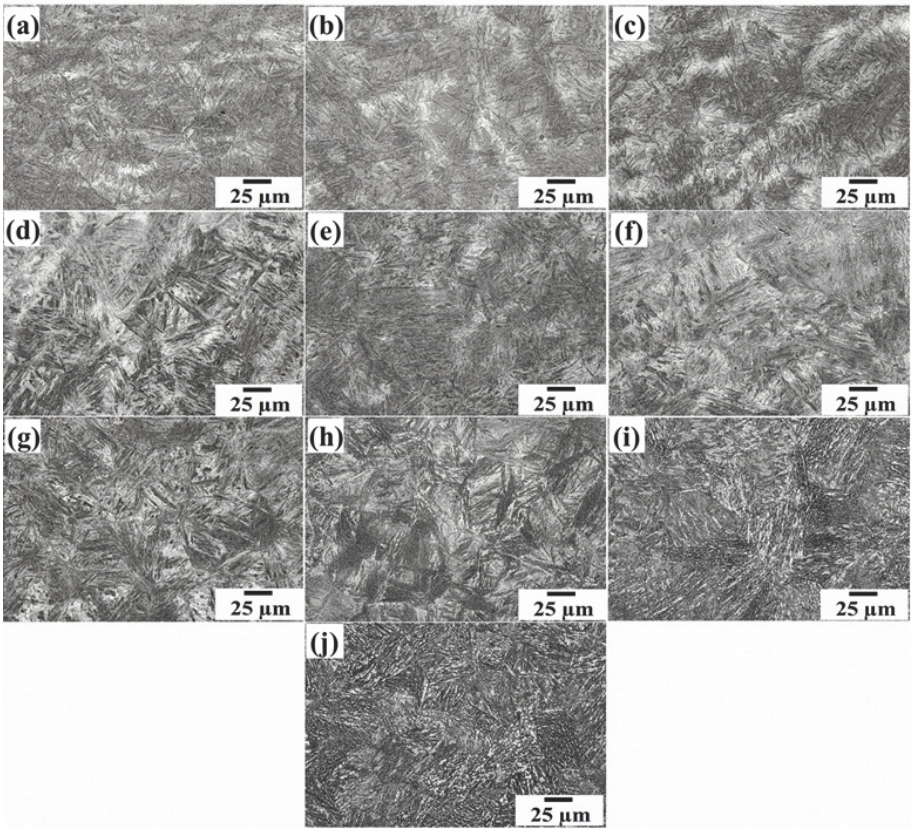

Fig. 39. LSCM micrographs of steel #2 with cooling rates of 60 (a), 30 (b), 15 (c), 5 (d), 1 (e), 0.6 (f), 0.2 (g), 0.08 (h), 0.02 (i) and 0.01 °C/s (j), respectively (Under CC BY license from Paper VI © 2019 Authors).

Fig. 40 shows the microhardness values of the transformation products, i.e. martensite and bainite. In the case of steel #1 (see Fig. 40(a)), the microhardness

values for the martensite increased from the CR of 0.01 up to 15 °C/s, after which the hardness is constant. This may be due to increasing the transfer of carbon from the martensite to the increasing volume fraction of RA, as illustrated below in section 4.4.3 [139]. As illustrated in Fig. 40(a), the microhardness of the bainite is constant in the range of CRs of 0.01–0.08 °C/s. For steel #2, a similar trend for the microhardness of the martensite was noticed (see Fig. 40(b)). However, the microhardness value of bainite increased with increasing the CR from 0.01 to 0.08 °C/s and after this CR, there was no further increment. The obvious difference in the trend of the microhardness of bainite in steel #1 and steel #2 in the range of CR 0.01–0.08 °C/s was attributed to the formation of higher volume fraction of proeutectoid carbides at the PAG boundaries in the case of steel #1. This led to an increase in the consumption of C, Cr, W and Mo and Cr with decreased CRs, which cause a drop in the hardness of the bainite. This effect can also be observed in the martensite's hardness as well. However, this effect is less noticeable in the case of steel #2 because of the lower frequency of proeutectoid carbide.

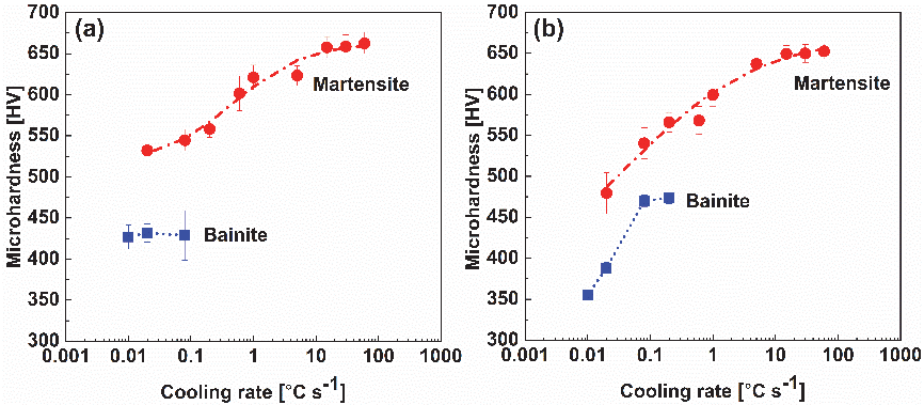

Fig. 40. Effect of cooling rate on microhardness of martensite and bainite in steel #1 (a) and steel #2 (b), respectively (Under CC BY license from Paper VI © 2019 Authors).

4.4 Microstructure characterization

Paper II and IV investigated the microstructure features of steels #1, #2, #3 and #4 without and with ESR. Paper V examined the variation in the microstructure features and precipitates during the forging for steel #3 with ESR. Paper VI examined the variation in the microstructure features as a result of changing the CR

and steel composition using steels #1 and #2. Paper VII investigated the effect of different heat treatments on the microstructure features.

4.4.1 Effect of ESR on the microstructure features, precipitates and segregations

Microstructure of steels without and with ESR

Figs. 41, 42, 43 and 44 illustrate the final microstructure of the forged steels #1, #2, #3 and #4 without and with ESR. The microstructure of steels #1, #2 and #3 consists mainly of martensite in addition to a very small fraction of precipitates and RA. Similar constituents are observed in steel #4 in addition to a large fraction of lower bainite. ESR led to an increment in the bainite volume fraction from 54 ± 3% to 66 ± 2% with similar microhardness values, while it led to a slight increase in the microhardness values of the martensite from 506 ± 5 HV to 518 ± 5 HV.

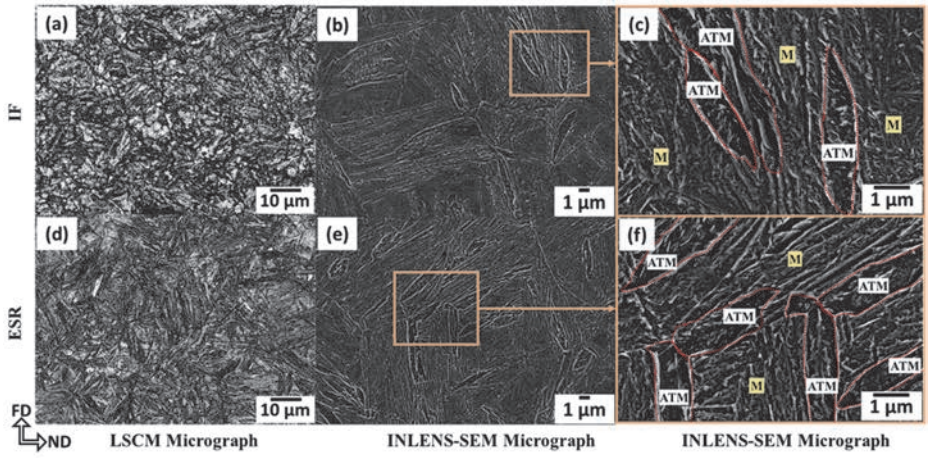

Fig. 41. Laser and INLENS-SEM micrographs of steel #1 without ESR (a, b and c) and with ESR (d, e and f). M: martensite and ATM: autotempered martensite (Under CC BY license from Paper IV © 2020 Authors).

Using XRD results, Rietveld refinement analysis was employed to determine the volume fractions of RA which are given in Table 13. As a result of ESR, the volume fractions of RA in steels #1 and #2 increased, but they decreased in the case of steels #3 and #4. This may be due to the slight change in the steel compositions, as

discussed above. The wt.% of carbon in the RA ($C\gamma$) was estimated from the lattice parameter using equation [140]

$$a = 0.3578 + 0.0033C\gamma, \tag{34}$$

where a (nm) refers to the lattice parameters of the RA.

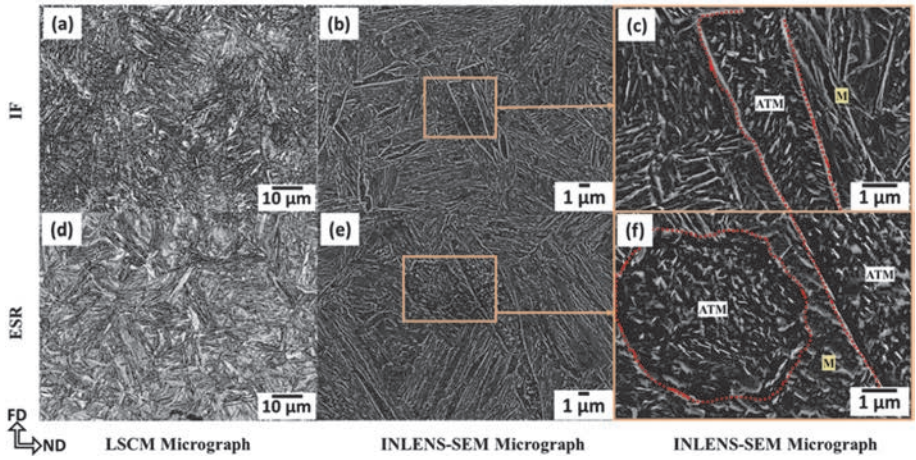

Fig. 42. Laser and INLENS-SEM micrographs of steel #2 without ESR (a, b and c) and with ESR (d, e and f). M: martensite and ATM: autotempered martensite (Reprinted [adapted] by permission from Paper II © 2018 Trans Tech Publications).

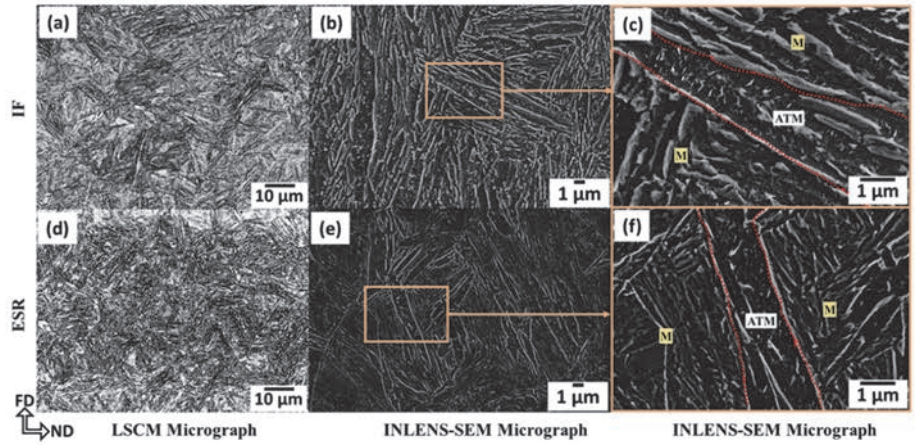

Fig. 43. Laser and INLENS-SEM micrographs of steel #3 without ESR (a, b and c) and with ESR (d, e and f). M: martensite and ATM: autotempered martensite (Under CC BY license from Paper IV © 2020 Authors).

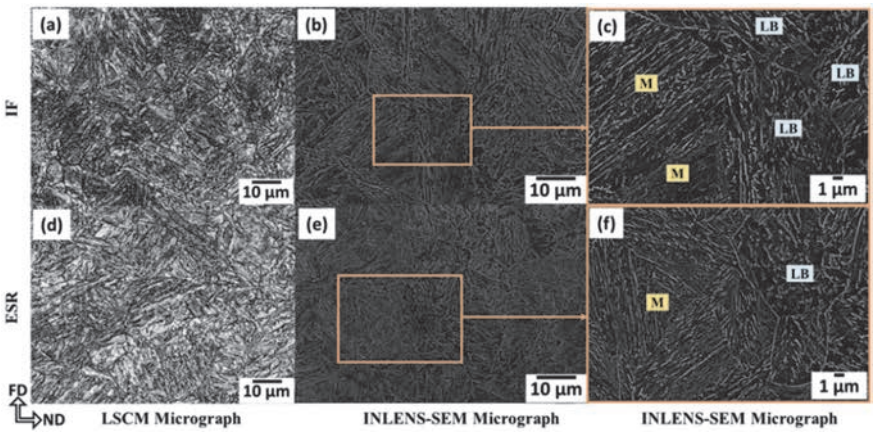

Fig. 44. Laser and INLENS-SEM micrographs of steel #4 without ESR (a, b and c) and with ESR (d, e and f). M: martensite and ATM: autotempered martensite (Under CC BY license from Paper IV © 2020 Authors).

ESR led to a decrease in $C\gamma$ in the fully martensitic steels #1, #2 and #3, while it had no effect on the $C\gamma$ in the mixed martensitic - bainitic steel, #4.

Fig. 45 shows the structure of the PAG of steels #1, #2, #3 and #4 without and with ESR, and the PAGS are given in Table 13. ESR decreased the mean PAGS to half in the case of steels #1 and #3 and slightly in the case of steel #2. However, it has no effect on the PAGS of steel #4 with the mixed martensitic-bainitic microstructure.

Table 13. Volume and carbon percentage of RA and PAGS in steels #1, #2, #3, #4 without and with ESR [Paper II], [Paper IV].

Steel	Process	Vol. fraction of RA [1] [%]	Mean C in RA (Cγ) [%]	Mean PAGS [2] [µm]
#1	IF	5.2 ± 0.3	0.7	25 ± 2.8
	ESR	6.5 ± 0.1	0.4	13 ± 1.7
#2	IF	3.3 ± 0.2	0.8	24 ± 2.8
	ESR	6.7 ± 0.2	0.6	19 ± 2.8
#3	IF	8.1 ± 0.2	1.2	27 ± 3.2
	ESR	6.6 ± 0.1	0.4	13 ± 2.1
#4	IF	7.1 ± 0.2	0.8	23 ± 2.7
	ESR	5.6 ± 0.8	0.8	22 ± 3.1

[1]Error bars are the standard deviation of the population.

[2]Error bars are 95% confidence intervals for the mean.

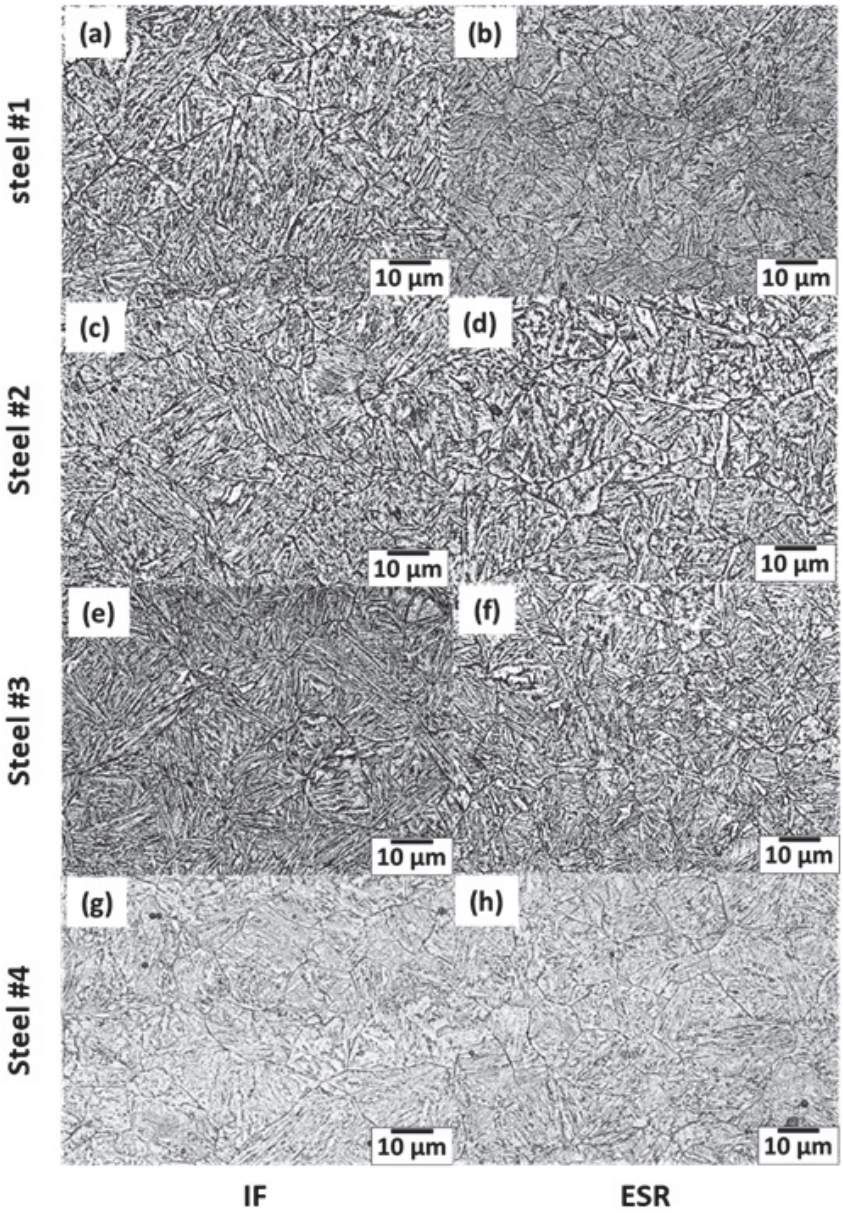

Fig. 45. LSCM micrograph of PAG of forged and air-cooled bars of steels #1, #2, #3 and #4 without ESR (a, c, e and g) and with ESR (b, d, f and h) (Reprinted [adapted] by permission from Paper II © 2018 Trans Tech Publications and under CC BY license from Paper IV © 2020 Authors).

The slight change in the steels' composition as a result ESR led to the variation in the microstructures, and these are in a good agreement with the predictions obtained by JMatPro software [141] given in Table 14 using the measured PAGS and CR of 0.3 °C/s. For steels #1 and #3 without ESR, the program predicted that the microstructure consists of 99% martensite and 1% RA. However, the predicted microstructure for steels #1 and #3 with ESR consists of 95% and 98% martensite, 4% and 1% bainite and 1% RA respectively. For steel #2 without ESR, the predicted microstructure constituents are 97% martensite, 2% bainite and 1% RA, while the predicted constituents for these steels with ESR consist of 96% martensite, 4% bainite and 1% RA.

In steel #4, the predicted constituents of the microstructure without ESR were 91% martensite, 8% bainite and 1% RA, while with ESR they consisted of 75% martensite, 24% bainite and 1% RA. ESR is predicted to lead to an increment in the bainite fraction, as was experimentally seen despite significantly higher than the actual observed bainite fractions.

Using the chemical compositions without and with ESR for steels #1, #2, #3 and #4, the transformation temperatures were predicted using JMatPro software and the results are given in Table 14. The predicted transformation temperatures for the steel compositions without and with ESR are very similar except B_s in steel #4, which increased by 12 °C.

Table 14. Results from simulations of the CCT behavior of the composition of steels #1, #2, #3 and #4 without and with ESR using JMatPro software [Paper II], [Paper IV].

Steel	Process	Vol. fraction of bainite [%]	Vol. fraction of martensite [%]	Vol. fraction of RA [%]	Bainite start temperature (B_s) [°C]	Martensite start temperature (M_s) [°C]
#1	IF	0	99	1	388	280
	ESR	4	95	1	397	279
#2	IF	2	97	1	410	290
	ESR	4	96	1	411	280
#3	IF	0	99	1	384	292
	ESR	1	98	1	382	284
#4	IF	8	91	1	426	313
	ESR	24	75	1	438	314

As is well known, the majority of alloy elements decrease B_s as, for example, indicated by the following empirical formula [142]

$$B_S = 630 - 45\mathrm{Mn} - 40\mathrm{V} - 35\mathrm{Si} - 30\mathrm{Cr} - 25\mathrm{Mo} - 20\mathrm{Ni} - 15. \quad (35)$$

The losses in some alloying elements during ESR, as discussed above, lead to a slight increase in B_s and the bainite volume fractions in the forged ingots with ESR compared to those without ESR. On the other hand, several studies [143]–[146] showed that the rise in Al content resulting from ESR accelerates the bainite transformation, thereby increasing the volume fraction of bainite and reducing the volume fraction of RA.

Comparison of the information provided in Table 13 and Table 14 illustrates that the JMatPro software failed to predict the volume fractions of RA that were significantly higher than expected.

EBSD results of steels #1, #2, #3 and #4 without and with ESR are presented in Figs. 46, 47, 48 and 49, respectively.

In steels #1 and #3, as shown in Figs. 46(a)–(d) and 48(a)–(d), halving the PAGS as a result of ESR through the increased pinning effects of precipitates formed during ESR, as discussed below, led to a change in the microstructural features significantly [147], [148], as ESR reduced the lath size, the average effective grain size, which is determined by high-angle grain boundaries and mean effective grain size, and the effective grain sizes at 90% in the cumulative ECD distribution ($D90\%_{GN}$).

However, in the case of steel #2 (see Fig. 47), although there was the slight decrease in the mean PAGS from 24 μm to 19 μm, the microstructural features such as lath size, effective grain size, $D90\%_{GN}$ and the grain boundary misorientation distribution remain unchanged after ESR.

In steel #4 (see Table 13 and Fig. 49), ESR has no effect on the PAGS, which results in no change in the distribution of grain boundary misorientations and $D90\%_{GN}$, while it caused a very slight change in the average lath and effective grain sizes.

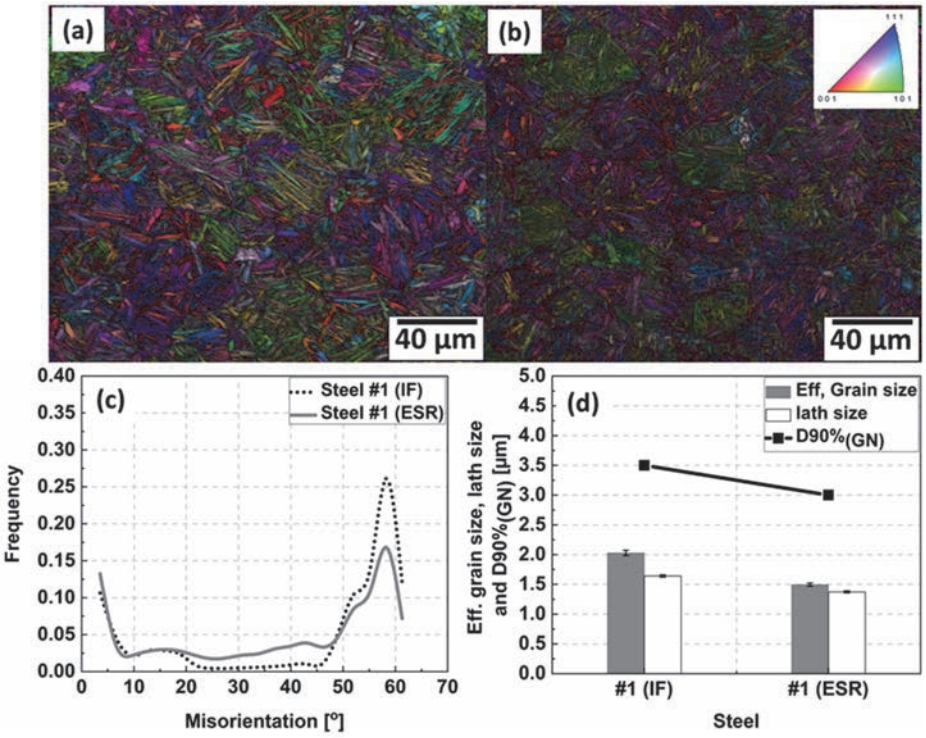

Fig. 46. Inverse pole figure (IPF) with superimposed image quality (IQ) map of forged and air-cooled bar of steel #1 without ESR (a) and with ESR (b), grain boundary misorientations (c), mean lath size, $D90\%_{GN}$ (d) (Reprinted [adapted] under CC BY license from Paper IV © 2020 Authors) .

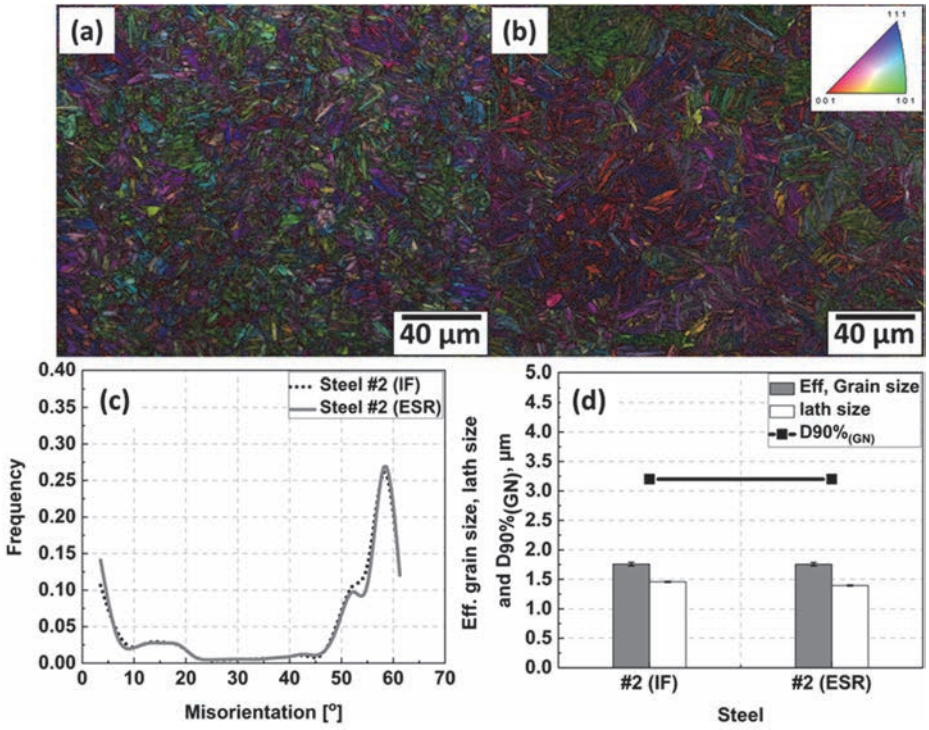

Fig. 47. Inverse pole figure (IPF) with superimposed Image quality (IQ) map of forged and air-cooled bar of steel #2 without ESR (a) and with ESR (b), grain boundary misorientations (c), mean lath size, D90%$_{GN}$ (d) (Reprinted [adapted] by permission from Paper II © 2018 Trans Tech Publications).

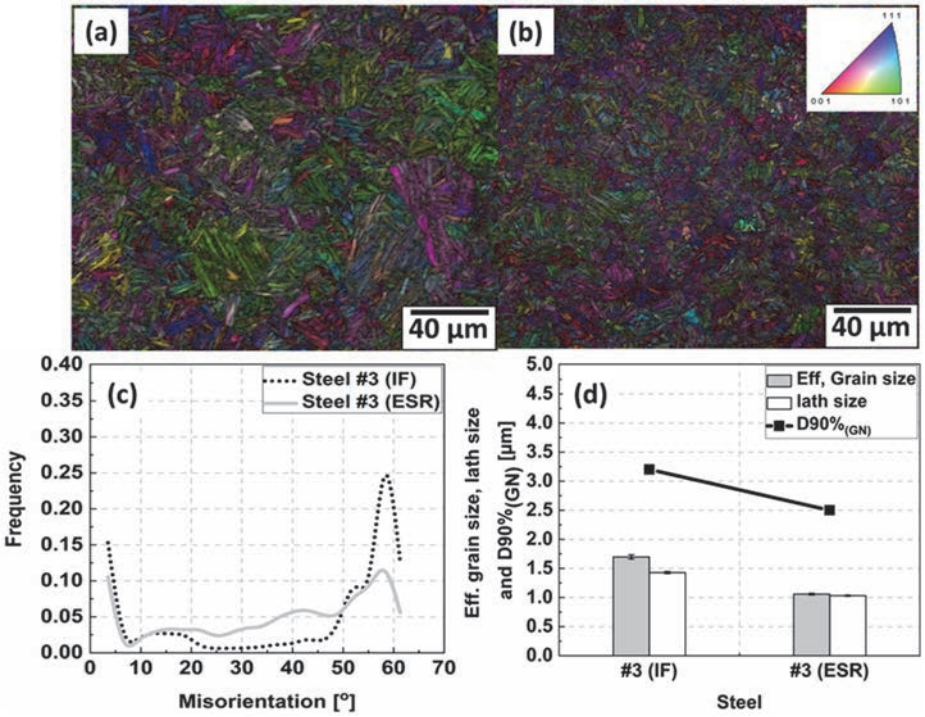

Fig. 48. Inverse pole figure (IPF) with superimposed image quality (IQ) map of forged and air-cooled bar of steel #3 without ESR (a) and with ESR (b), grain boundary misorientations (c), mean lath size, $D90\%_{GN}$ (d) (Reprinted [adapted] under CC BY license from Paper IV © 2020 Authors).

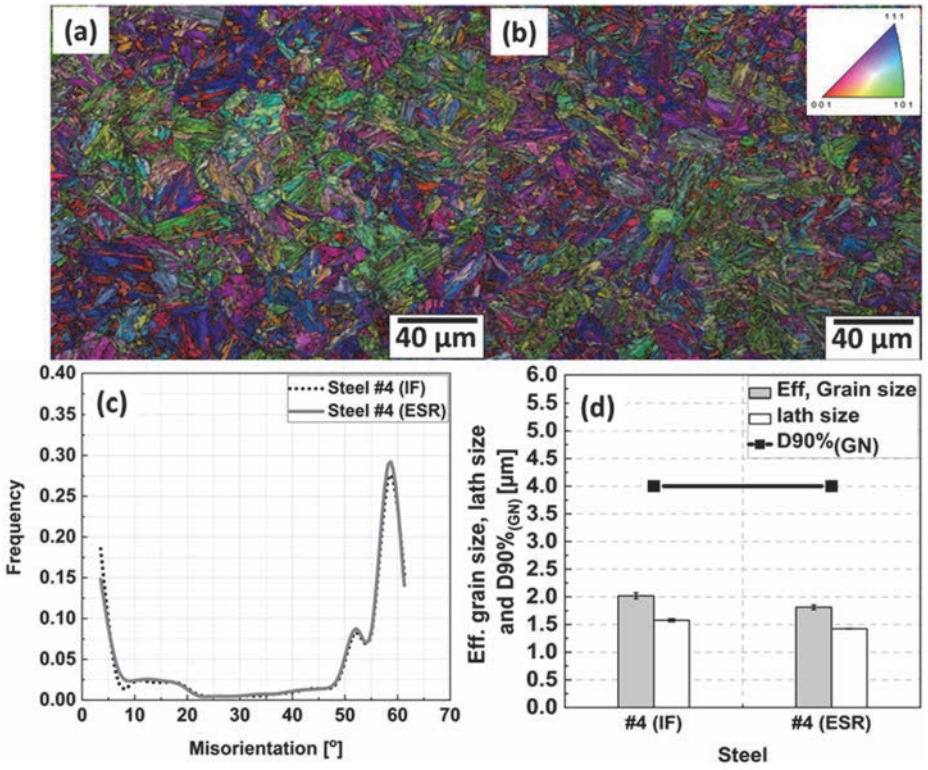

Fig. 49. Inverse pole figure (IPF) with superimposed image quality (IQ) map of forged and air-cooled bar of steel #4 without ESR (a) and with ESR (b), grain boundary misorientations (c), mean lath size, $D90\%_{GN}$ (d) (Reprinted [adapted] under CC BY license from Paper IV © 2020 Authors).

Volume fractions, size and frequency of precipitates in steels #1, #2, #3 and #4 without and with ESR.

Typical INLENS-SEM micrographs for the precipitates in steels #1, #2, #3 and #4 are shown in Fig. 50. For quantitative analysis including volume fraction, size, and frequency of the precipitates, 20 INLENS-SEM micrographs with total investigated area of about 588 μm^2 were investigated for each steel without and with ESR. The precipitates size in ECD and numbers were determined using ImageJ software. Then the precipitates volume fractions were calculated using equation [149]

$$f = \frac{N\frac{4\pi}{3}(D_p/2)^3}{S_0 D_p} = \frac{N\pi D_p^2}{6S_0} = \frac{2NS}{3S_0}, \quad (36)$$

where N is the number of particles per investigated area, D_p is the mean equivalent circle diameter of the particles, S_o the total area analyzed, and S the particle area.

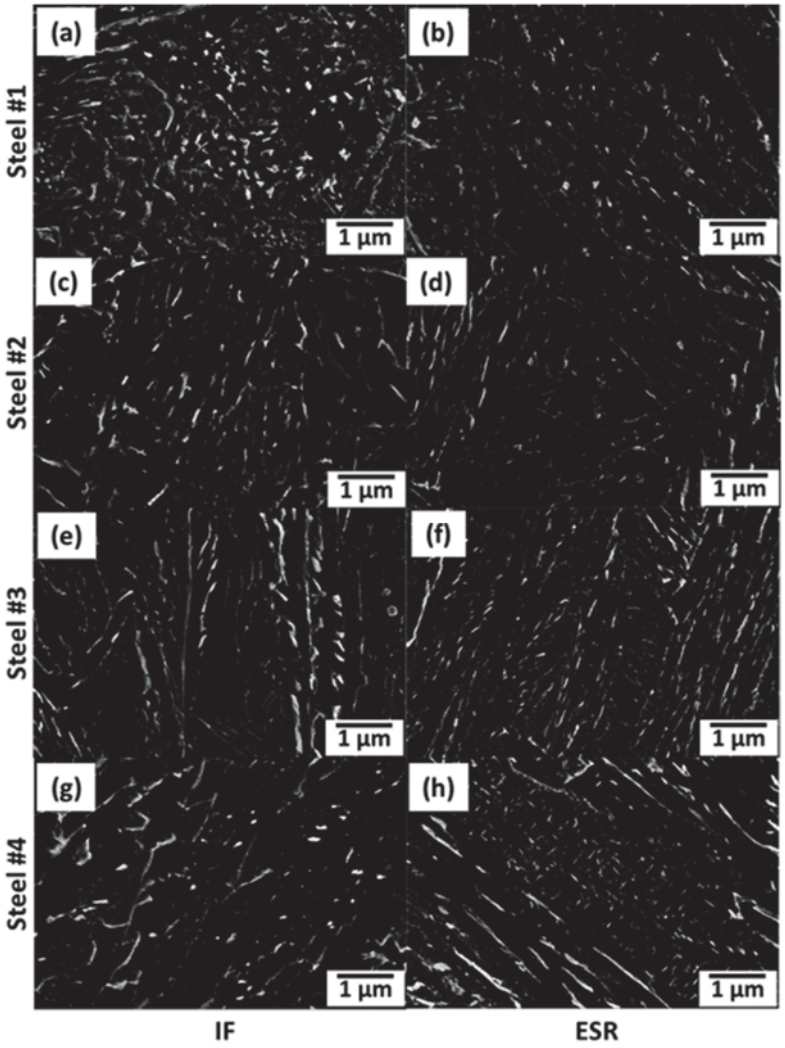

Fig. 50. INLENS-SEM micrographs for precipitates of steels #1, #2, #3 and #4 without ESR (a, c, e and g) and with ESR (b, d, f and h) (Reprinted by permission from Paper II © 2018 Trans Tech Publications and under CC BY license from Paper IV © 2020 Authors).

The variation as a result of ESR in the precipitates characteristics, i.e. the number density, the maximum size, the average size, the volume fractions and the 95th percentiles in the cumulative ECD distribution ($D95\%_{ppt}$) are given in Table 15. ESR increased the number of the precipitates in steels #1, #2, #3 and #4 by about 29%, 19%, 56% and 40% respectively. Also, ESR led to an increase in the volume fraction of the precipitates by about 5%, 16%, 41% and 45%. This may be attributed to the slight increment in the carbon content of steel as a result of ESR, as discussed in Section 4.1.1. However, ESR led to a decrease in the mean size, maximum size and $D95\%_{ppt}$ in steels #1, #2, #3 and #4.

Table 15. Characteristics of precipitates in steels #1, #2, #3 and #4 without and with ESR [Paper II], [Paper IV].

Steel	Process	Volume fraction of precipitates (*f*) [%]	Number of precipitates per total investigated area, 588 μm^2	Average size [nm]	$D95\%_{ppt}$, [nm]	Max. Size [nm]
#1	IF	0.37	1742 (2.96/ μm^2)	49 ± 0.53	120	381
	ESR	0.39	2239 (3.81/ μm^2)	44 ± 0.41	110	321
#2	IF	0.37	1195 (2.03/ μm^2)	59 ± 0.80	150	427
	ESR	0.43	1426 (2.43/ μm^2)	58. ± 0.78	149	386
#3	IF	0.41	1333 (2.27/ μm^2)	59 ± 0.94	170	532
	ESR	0.58	2078 (3.53/ μm^2)	56 ± 0.61	140	498
#4	IF	0.31	1108 (1.88/ μm^2)	56 ± 1.00	150	565
	ESR	0.45	1555 (2.64/ μm^2)	54 ± 0.82	140	541

The size, shape and volume fraction of the precipitates are consistent with their precipitation through the austenite transformation to bainite and the autotempering of martensite. As discussed below, there are very small volume fractions of precipitates that can form directly from the austenite, e.g. AlN, TiN and VN.

In Paper IV, Thermo-Calc 2017b software with the TCFE7 database was used to predict the volume fraction of the precipitates in equilibrium at 950 °C and 750 °C and their solvus temperatures for steels #1, #3 and #4 (see Table 16).

The variation in the steels' composition as a result of ESR, especially the large increment in the content of Al, led to an obvious difference in the types and volume fractions of the precipitates at 950 and 750 °C.

Also, the change in the steels' composition caused by ESR resulted in a large increase in the solvus temperatures of AlN, TiN and VN, which become higher than the forging temperatures range (1100–950 °C) and increase the volume fractions of these precipitates at 950 and 750 °C (see Table 16).

Table 16. Characteristics of precipitates in steels #1, #3 and #4 without and with ESR (calculated using ThermoCalc software) (Reprinted [adapted] under CC BY license from Paper IV © 2020 Authors).

Steel	Process	Temperature, [°C]	Precipitates	Solvus temperature, [°C]	Volume fractions of each precipitate at given temperature, [%]	Total Volume fractions at given temperature, [%]
#1	IF	950	AlN	1022	0.0100	0.064
			VN	1064	0.0539	
		750	AlN	1022	0.0250	2.417
			Ti(N,C)	793	0.0003	
			VN	1064	0.1100	
			$M_{23}C_6$ $[(Cr,Fe)_{20}$ $(Mo,W)_3$ $(C)_6]$	803	2.2820	
	ESR	950	AlN	1186	0.0703	0.072
			TiN	1270	0.0020	
		750	AlN	1186	0.0750	2.373
			VC	900	0.1240	
			$M_{23}C_6$ $[(Cr,Fe)_{20}$ $(Mo,W)_3$ $(C)_6]$	800	2.1744	
#3	IF	950	AlN	1048	0.0140	0.106
			VN	1120	0.0920	
		750	AlN	1048	0.0280	2.196
			V(N,C)	1120	0.1350	
			Ti(N,C)	804	0.0006	
			$M_{23}C_6$ $[(Cr,Fe)_{20}$ $(Mo,W)_3$ $(C)_6]$	781	2.0320	
	ESR	950	AlN	1224	0.1130	0.119
			TiN	1396	0.0060	
		750	AlN	1224	0.1180	2.732
			TiN	1396	0.0040	
			VC	915	0.1400	
			$M_{23}C_6$ $[(Cr,Fe)_{20}$ $(Mo,W)_3$ $(C)_6]$	797	2.4700	
#4	IF	950	AlN	1069	0.0190	0.092
			TiN	1396	0.0730	
		750	AlN	1069	0.0310	0.143
			TiN	1396	0.1120	
	ESR	950	AlN	1178	0.0910	0.093
			TiN	1305	0.0020	
		750	AlN	1178	0.1000	0.170
			TiN	1305	0.0010	
			V(C,N)	853	0.0690	

Also, precipitation of AlN, TiN and VN should be increased due to the driving force available during the forging at the temperatures range 1100–950 °C. In addition, after forging, at 750 °C there will be a driving force for the formation of different types of precipitates, as illustrated in Table 16.

Fig. 51 illustrates that the slight rise in the expected equilibrium volume fraction of the precipitates, e.g. AlN, TiN and VN formed during solidifications of the ingots and cooling through the forging temperature range 1100–950 °C, seems to be correlated with the decrease in the PAGS, which is the main reason behind the refining of the other microstructure features.

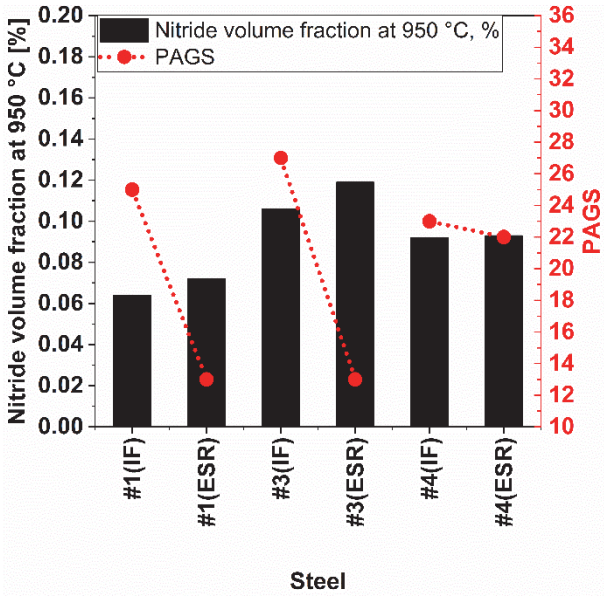

Fig. 51. Correlation between the predicted equilibrium volume fraction of nitrides at the forging finish temperature (950 °C) and the PAGS (Reprinted [adapted] under CC BY license from Paper IV © 2020 Authors).

Influence of ESR on microsegregation

Usually, in ESR ingots, there is some segregation of the alloying elements as a result of the inter-dendritic elemental enrichment, which has a harmful effect on the final mechanical properties of the cast and forged products [150]. Arh et al. [147] assumed that the higher temperature gradients and CRs in ESR resulted in finer

secondary dendrite arm spacings and less micro-segregation than those in normally cast steel, but this did not happen in steels #1, #2, #3 and #4, as illustrated below.

In order to evaluate the influence of ESR on the microsegregation of the alloying elements, EPMA was employed to measure the distribution of Cr, Ni, Mn, Si, W, Mo and V. The elemental segregation degree was determined by calculating the nominal segregation index (ζ_i) [151], [152] using equation

$$\zeta_i = C_o^i / C_{interdendritic}^i, \tag{37}$$

where C_o^i is the concentration of the alloying elements given in Table (5) and $C_{interdendritic}^i$ is the concentration of the alloying elements measured in the interdendritic area. The results are given in Table 17. Also, the segregation degree was predicted using IDS software [153] by determination of the nominal segregation index and the results are given in Table 17. But, unfortunately, the nominal segregation index for W is not calculated because W is not included in the database of the IDS software. The results given in Table 17 prove that there is no significant effect of ESR on the microsegregation of the alloying elements. Perhaps, the smaller diffusion distances resulting from smaller secondary dendrite arm spacings are neutralized by the shorter diffusion times that result from the higher CRs encountered in ESR. Table 17 also indicates that, in many cases, the IDS software is able to predict segregation indices that are close to the experimentally measured values.

Table 17. Theoretical and experimental segregation indices (ζ_i) for the alloying elements (Reprinted [adapted] under CC BY license from Paper IV © 2020 Authors).

Steel	Process	Si	Cr	W	Mo	Ni	Mn	V
#1	IDS Calc.	0.8	0.7	NA	0.3	1.0	0.8	0.4
	IF	0.8	0.6	1.0	0.4	0.9	0.8	0.4
	ESR	0.8	0.6	0.8	0.4	1.0	0.7	0.5
#3	IDS Calc.	1.1	0.6	NA	0.2	0.9	1.4	0.2
	IF	0.7	0.6	1.0	0.4	0.9	0.8	0.3
	ESR	0.7	0.7	0.8	0.5	1.0	0.7	0.5
#4	IDS Calc.	0.8	0.7	NA	0.3	0.9	0.8	0.4
	IF	0.7	0.6	1.0	0.5	1.0	0.8	0.5
	ESR	0.7	0.7	1.0	0.6	1.0	0.8	0.4

4.4.2 Microstructure and precipitates variation during the forging

In order to understand the variation in the precipitates and microstructure of the investigated steels during the forging, in Paper V, steel #3 with ESR was selected and the effect of hot forging parameters, i.e. FFT and TAS, on the microstructure and precipitates formation was studied. In addition, the results were supported by thermodynamic calculations as discussed below.

Thermodynamic calculations of the Precipitates

Thermo-Calc software version 2018a was used to perform the thermodynamic calculation. AlN and TiN represent the equilibrium precipitates in austenite of steel #3 in the temperature range 950–1400 °C (see Fig. 52). As illustrated in Table 18, by decreasing the temperature, the precipitates volume fraction increased while the chemical composition of the precipitates is not changed over the temperature range 1100–950 °C, which was used in the calculations. The calculated solubility temperatures of AlN and TiN of steel #3 are 1224 °C and 1396 °C, respectively. This means that there are some undissolved precipitates remaining in the steel even after holding at 1100 °C, which, in fact, was observed experimentally in the non-strained specimens (1100–0), as explained below.

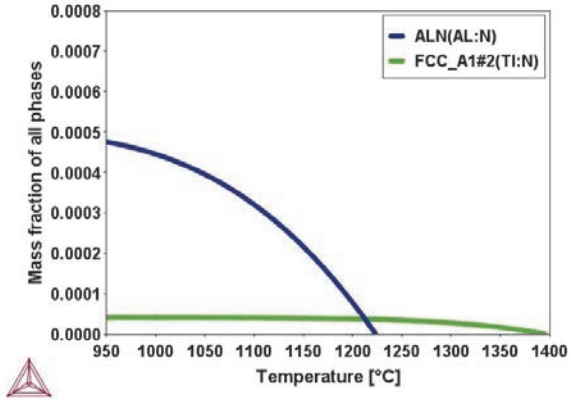

Fig. 52. Thermodynamic calculations for precipitates types formed at high temperatures in steel #3 (Reprinted by permission from Paper V © 2020 WILEY-VCH).

Table 18. Predicted equilibrium precipitate volume fractions and compositions in steel #3 (Reprinted by permission from Paper V © 2020 WILEY-VCH).

Temperature	Precipitate	Vol.	Total Vol.	Chemical composition [wt.%]							
[°C]	type	[%]	[%]	C	N	Al	Ti	V	Cr	Nb	W
1100	AlN	0.075	0.081	-	34	66	-	-	-	-	-
	TiN	0.006		2	21	-	72	4	1	1	-
1050	AlN	0.093	0.099	-	34	66	-	-	-	-	-
	TiN	0.006		2	20	-	72	4	1	1	-
1000	AlN	0.105	0.111	-	34	66	-	-	-	-	-
	TiN	0.006		3	19	-	72	4	1	1	1
950	AlN	0.113	0.119	-	34	66	-	-	-	-	-
	TiN	0.006		4	18	-	72	4	1	1	1

Chemical composition and structure of the precipitates

The precipitates formed before and during the forging can be subdivided into two principal categories based on the morphology, EDS analysis and diffraction analysis (see Table 19 and Fig. 53): i) aluminium nitride AlN, and ii) titanium nitride TiN with traces of V, Nb, Mo and W, which substitute Ti without a change in the lattice structure. Sometimes, AlN seems to be nucleated and grown on TiN to form composite precipitates referred to as TiN-AlN (see Figs. 53 and 54). In the composite precipitates, the AlN nucleates on pre-existing TiN precipitates to form a shell or cap. In EDS spectra, the peaks of Cu and C must be neglected because they are partly or completely as a result of the copper grid and the carbon replica, respectively. Also, the EDS peaks of O, S and Fe which are resulting from the preparation of the carbon extraction replica must also be neglected [154].

Table 19. Chemical compositions of the precipitates measured with EDS in steel #3 (Reprinted by permission from Paper V © 2020 WILEY-VCH).

Precipitate	Unit	N	O	Al	S	Ti	V	Fe	Nb	Mo	W
AlN	wt.%	35 ± 1	3 ± 1	60 ± 0	1 ± 0	1 ± 0	-	-	-	-	-
	at. %	51 ± 1	3 ± 1	44 ± 1	1 ± 0	1 ± 0	-	-	-	-	-
TiN	wt.%	33 ± 2	2 ± 1	-	-	49 ± 1	7 ± 0	1 ± 0	2 ± 1	2 ± 1	4 ± 1
	at. %	61 ± 2	3 ± 1	-	-	28 ± 2	4 ± 0	1 ± 0	1 ± 0	1 ± 0	1 ± 0
AlN-TiN	wt.%	34 ± 1	1 ± 0	35 ± 3	-	21 ± 2	3 ± 0	1 ± 0	-	-	-
	at. %	57 ± 2	1 ± 0	26 ± 3	-	13 ± 1	2 ± 0	1 ± 0	-	-	-

It is now clear that only nitrides form during the forging and that the carbides observed in Papers II and IV, and discussed in Section 4.4.1, must have formed during air cooling after the forging through a martensite autotempering process.

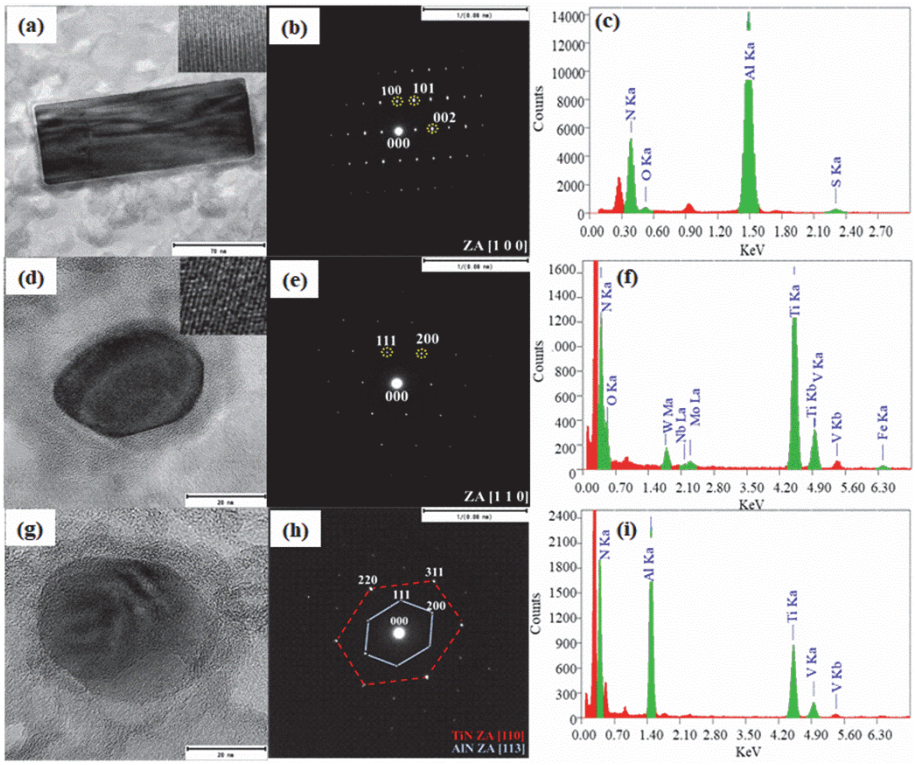

Fig. 53. Typical TEM micrographs, corresponding SAD patterns and corresponding EDS analysis of large hcp plate-like AlN precipitate with an enlarged HRTEM micrograph (a, b, c), TiN precipitate with enlarged HRTEM micrograph (d, e, f) and AlN-TiN composite (g, h, i) in steel #3 (Reprinted by permission from Paper V © 2020 WILEY-VCH).

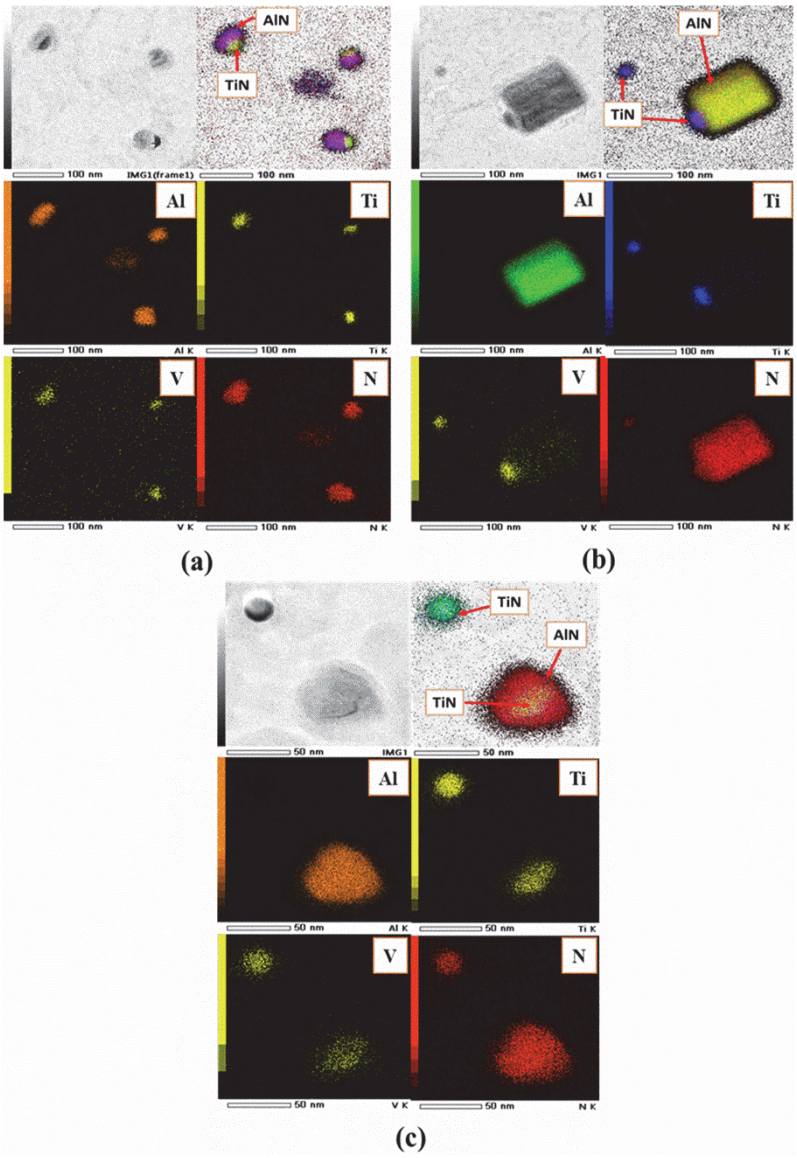

Fig. 54. Elemental EDS mapping of composite TiN-AlN precipitates with a cap of spherical morphology of AlN on the pre-existing TiN precipitate (a), TiN and composite TiN-AlN precipitates with a cap of plate-like morphology of AlN on the pre-existed TiN (b), precipitate and TiN and composite TiN-AlN precipitates with a shell of spherical morphology of AlN and core of TiN precipitates (c) in steel #3 (Reprinted by permission from Paper V © 2020 WILEY-VCH).

Size and frequency of precipitates

Fig. 55 shows the morphology of the extracted precipitates formed at various TAS and FFT, while their size distribution and statistics are given in Fig. 56 and Table 20, respectively. As described in the accompanying papers, the size and frequency distributions of the precipitates were determined using carbon extraction replicas. While this has the advantage over thin-foil techniques of providing high contrast between the precipitates and their background, and a good statistical basis for accurate size determinations, it does suffer from the possible loss of very small precipitates < 5 nm in diameter. This has to be born in mind when interpreting the results.

By comparing the results for the 1100-0 and the 1100-0.2 specimens, it is clear that there is no effect of 0.2 strain on the size distribution of the precipitates. This could be attributed to the following reasons: i) in the 1100-0 samples, precipitates can be rather similar to what is predicted in equilibrium, which means a slight driving force for further precipitation at this temperature, ii) small strain magnitude (0.2) and related substructural changes and iii) the short time at the same temperature. It is well known that the amount of introduced dislocations and sub-grains, which represent the main sites for nucleating of the strain induced precipitates, depend mainly on different parameters, such as FFT, TAS and strain rate.

Compared to 1100-0 and 1100-0.2 specimens, the decrease of the FFT and increase of the TAS in the case of 1050-0.4 have a great effect of the formation of new and finely distributed precipitates, as can be observed from Fig. 55(c) compared to Fig. 55(a) and (b). This resulted in a decrease in the frequency of the largest precipitates and a rise in the frequency of the smallest precipitates with ECD below 40 nm, as shown in Fig. 56. These can indicate the slow growth kinetics at this stage of the forging process, in spite of the large number of the small precipitates [155]. Also, these have a large effect on the mean ECD and $D90\%_{ppt}$ of the extracted precipitates (see Table 20 and Fig. 57). This is due to the high storage energy generated by the deformation, and decreasing the FFT led to a decrease in the activation energy for nucleation and increased the driving force for precipitation, in addition to the increased diffusion rate of the microalloying elements in the strained austenite [156]. Furthermore, besides the prior austenite grain boundaries, the new introduced sub-grain boundaries and dislocations as a result of deformation led to increasing the nucleation sites and the kinetics of precipitation [156] through the pipe diffusion, along with dislocation core [157]. These results are in a good

agreement with those obtained by Okaguchi and Hashimoto [158], who reported that in the Nb-Ti bearing HSLA steel, the precipitation kinetics is accelerated in deformed austenite compared to undeformed austenite and becomes more significant at 900 °C than at 1000 °C. The precipitates formed in the deformed austenite were also finer than those formed in the undeformed austenite.

Compared to 1050-0.4 specimens, the lower temperature and higher total strain used in the case of 1000-0.6 specimens, and with the aid of bulk diffusion and pipe diffusion along dislocation core, led to growth and coarsening of the large precipitates or the new-formed strain induced precipitates at the expense of smaller precipitates, which was clearly observed from the reduction of the frequency of the small precipitates of less than 40 nm and increase in the frequency of large precipitates (see Fig. 56). The lower supersaturation of the solution as well as the nucleation rate may be the main reason for this behavior [159]. At this stage, the precipitates with a radius larger than the critical radius will grow up continuously, while those with a radius smaller than the critical radius will dissolve. These changes caused a sharp increase in the mean ECD and $D90\%_{ppt}$ of the extracted precipitates (see Table 20 and Fig. 57).

Compared to 1000-0.6, the lower temperature and higher total strain used in the case of 950-0.8 specimens caused a small increase in the frequency of the newly formed small precipitates (less than 40 nm) without any change in the frequency of the largest precipitates. These caused a slight decrease in the mean ECD and $D90\%_{ppt}$ of the precipitates, as can be seen from Table 20 and Fig. 57.

In general, the experimental results for the precipitate types show a good agreement with the thermodynamic calculation results, even without considering the applied strain in the thermodynamic calculations.

Table 20. Statistics of the extracted precipitates including number of precipitates, Mean ECD and $D90\%_{ppt}$ in steel #3 [Paper V].

Statistics	1100-0	1100-0.2	1050-0.4	1000-0.6	950-0.8
No. of precipitates	696	342	1108	360	510
Mean ECD[1]	54 ± 2	53 ± 3	41 ± 2	63 ± 3	61 ± 3
$D90\%_{ppt}$	94	94	84	110	105

[1] Error bar are 95% confidence intervals for the mean.

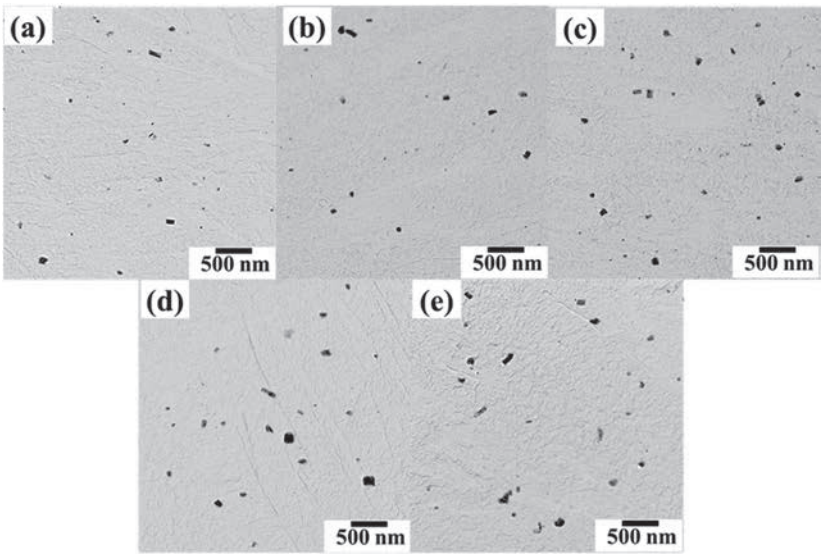

Fig. 55. Typical STEM micrographs of carbon extraction replica for the morphology and distribution of the extracted precipitates from steel #3 at different TAS and FFT, 1100-0 (a); 1100-0.2 (b); 1050-0.4 (c); 1000-0.6 (d) and 950-0.8 (e) (Reprinted [adapted] by permission from Paper V © 2020 WILEY-VCH).

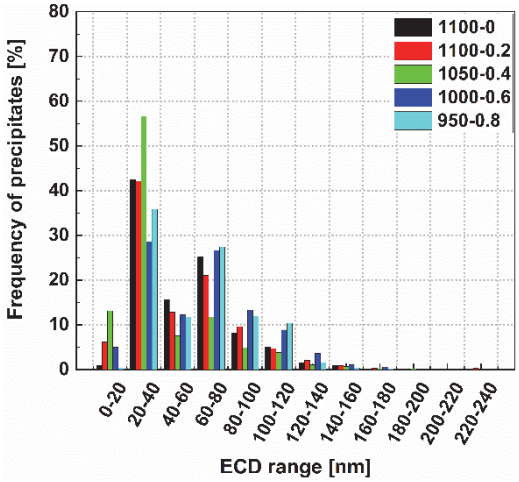

Fig. 56. Size distribution of the precipitates in steel #3 at different FFT and applied TAS (Reprinted [adapted] by permission from Paper V © 2020 WILEY-VCH).

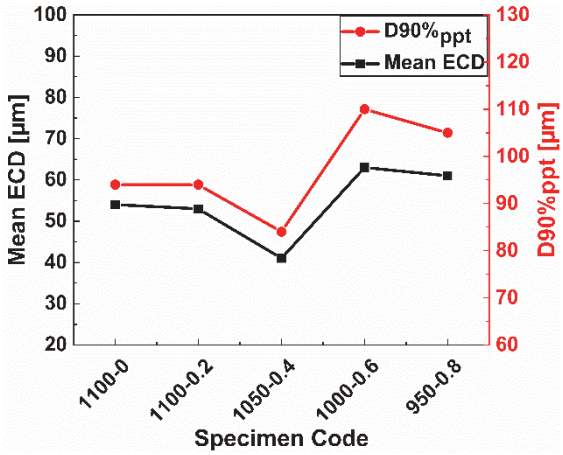

Fig. 57. Effect of TAS and FFT on the mean ECD and D90%$_{ppt}$ of the extracted precipitates from steel #3 (Reprinted [adapted] by permission from Paper V © 2020 WILEY-VCH).

Variation in the grain structure during the forging

It can be seen from Fig. 58, for the whole range of TAS, i.e. from 0 to 0.8, and FFT, i.e. 1100 to 950 °C, that the final microstructure consists of lath martensite with small volume fraction of fine precipitates. The precipitates can be seen on grain boundaries, sub-grain boundaries and within the martensitic laths. The change in the precipitate characteristics discussed above has a clear impact on the grain structure, as discussed below. The reconstructed PAG structure, the PAGS expressed as a mean ECD and their size distributions after removal of all edge grains are given in Fig. 59. Fig. 60 shows inverse pole figures (IPF) with superimposed image quality (IQ) maps, ECD mapping of each grain and ECD grain size distributions after removal of all edge grains. Fig. 61 shows grain boundary misorientation distributions for the as-quenched microstructures.

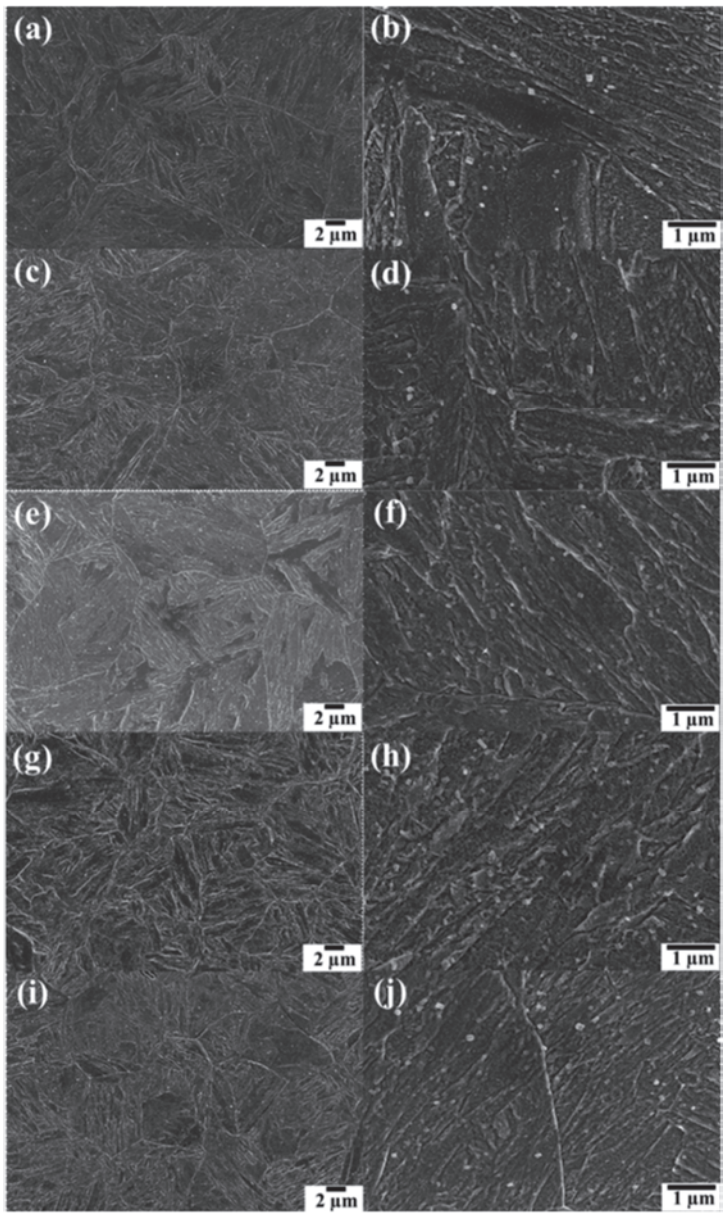

Fig. 58. Inlens SEM micrographs of steel #3 with ESR for the samples 1100-0 (a, b); 1100-0.2 (c, d); 1050-0.4 (e, f); 1000-0.6 (g, h) and 950-0.8 (i, j) (Reprinted [adapted] by permission from Paper V © 2020 WILEY-VCH).

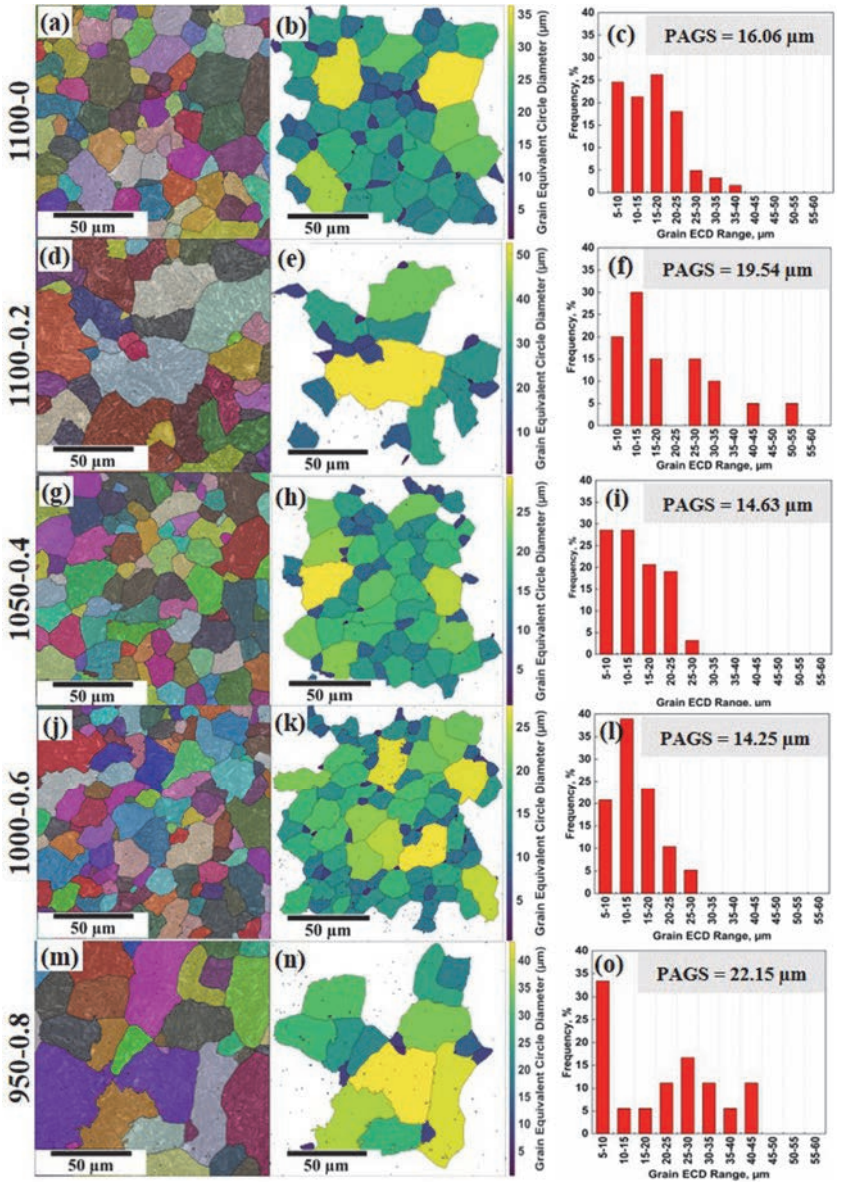

Fig. 59. PAG structures, ECD mapping of each PAG, size distribution and mean PAGS obtained by analyzing EBSD data with MTEX and MATLAB software for the samples 1100-0 (a, b, c); 1100-0.2 (d, e, f); 1050-0.4 (g, h, i); 1000-0.6 (j, k, l) and 950-0.8 (m, n, o). The images (a, d, g, j, m) are combinations of austenite orientation with image quality (Reprinted by permission from Paper V © 2020 WILEY-VCH).

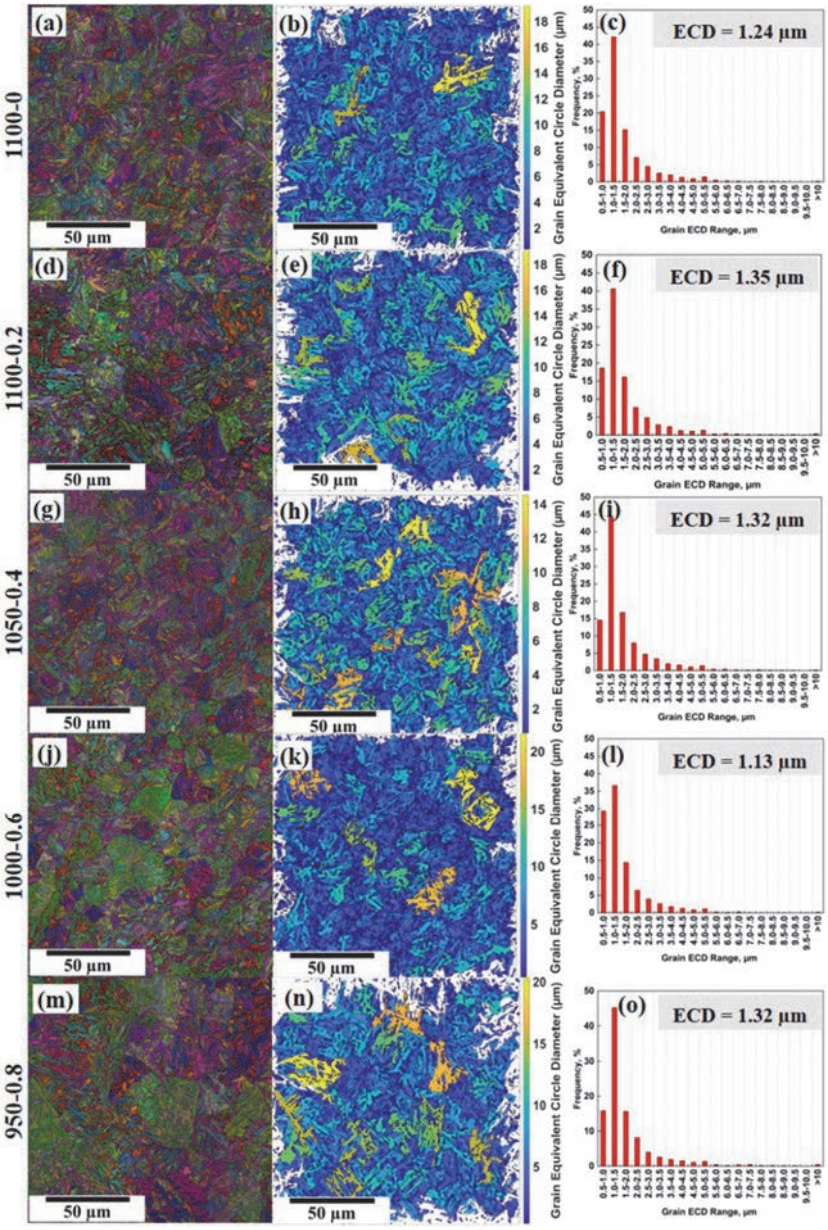

Fig. 60. IPF with superimposed IQ maps, ECD mapping of each grain, ECD grain size distribution and mean EGS for the samples 1100-0 (a, b, c); 1100-0.2 (d, e, f); 1050-0.4 (g, h, i); 1000-0.6 (j, k, l) and 950-0.8 (m, n, o) (Reprinted by permission from Paper V © 2020 WILEY-VCH).

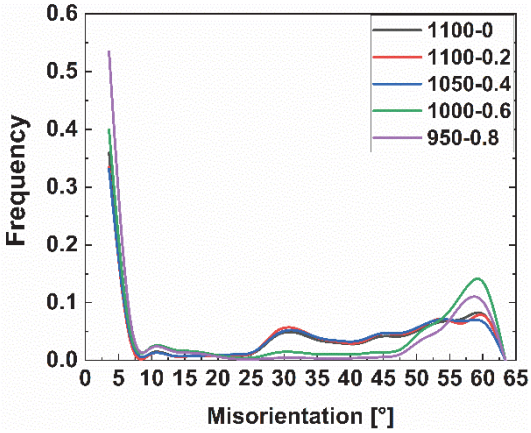

Fig. 61. Grain boundary misorientation distributions for the samples 1100-0; 1100-0.2; 1050-0.4; 1000-0.6 and 950-0.8 (Reprinted by permission from Paper V © 2020 WILEY-VCH).

At the beginning of the forging, the high solubility of the nitrogen at this high temperature in the case of 1100-0.2 specimens leads to the dissolution of some of the precipitates still present in the 1100-0 specimens. This leads to a decrease in the grain boundary pinning effect of the precipitates. The observed grain growth seen as an increase in the PAGS may result from a decrease in the grain boundary pinning effect of the precipitates or, maybe, it is just a coarse recrystallized grain size resulting from the high temperature and small applied strain. The increase in the PAGS is seen in an increase in the EGS and the effective grain size at 90% in the cumulative grain area distribution ($D90\%_{GA}$). However, with a further decrease in the forging temperature and the additional strain in the case of specimen 1050-0.4, there is an increase in the formation of small strain induced precipitates, as shown above. This increases the grain boundary pinning effect, retaining a finer recrystallized austenite grain size at this stage of the forging. In the case of the specimen 1000-0.6, there is no difference in the PAGS compared to the 1050-0.4 specimens. At the end of the forging, i.e. specimen 950-0.8, precipitate coarsening, which started at 1000 °C, reduces the pinning effect of the grain boundary, leading to grain growth and an increase in the PAGS. Also, this coarsening in the microstructural features may result from incomplete recrystallization, recrystallization to a coarser grain size or recrystallization followed by grain growth. Further investigations are needed to identify the mechanisms leading to the observed changes in the PAGS.

The PAGS has a clear impact on the sub-structures of the quenched microstructures. This can be seen in Fig. 60 and Fig. 62, which show the dependence of D90%$_{GA}$ on the PAGS.

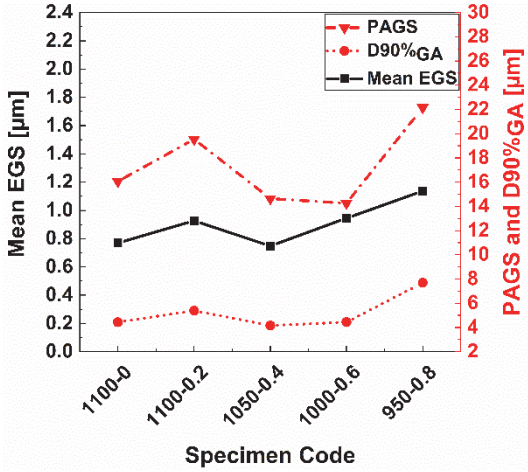

Fig. 62. Influence of the forging parameters on the PAGS, D90%$_{GA}$ and mean EGS (Reprinted [adapted] by permission from Paper V © 2020 WILEY-VCH).

4.4.3 Microstructure changes with the variation in the chemical composition and cooling rate

Fig. 63 shows a typical SEM micrograph of steels #1 and #2 with the CRs of 60, 1 and 0.01 °C/s. They confirm the results obtained from the LSCM and microhardness testing that the final microstructure comprises mainly of martensite at the CRs of 60 and 1°C/s, and mainly of granular bainite at CR of 0.01 °C/s. The significant increase in PAGS, as shown below, and the slowest CR enhance the possibility of the formation of granular bainite (see Fig. 63(c) and (f)) [160]. The results of EPMA line analysis across the grain boundaries in the samples with CR of 0.01 °C/s are given in Fig. 64. These illustrated the detection of high levels of Cr, W and Mo in the case of steel #1 (see Fig. 64(c)) and W in the case of steel #2 (see Fig. 64(d)). The FESEM-EDS results shown in Fig. 65 illustrate that the increased levels of Cr, W and Mo are attributed to the precipitation of proeutectoid alloy-rich carbides at PAG boundaries due to the slow CR. In the case of steel #1, two kinds of proeutectoid carbides are detected: iron carbides containing some Cr and complex carbides containing a high percentage of Fe, W and Mo.

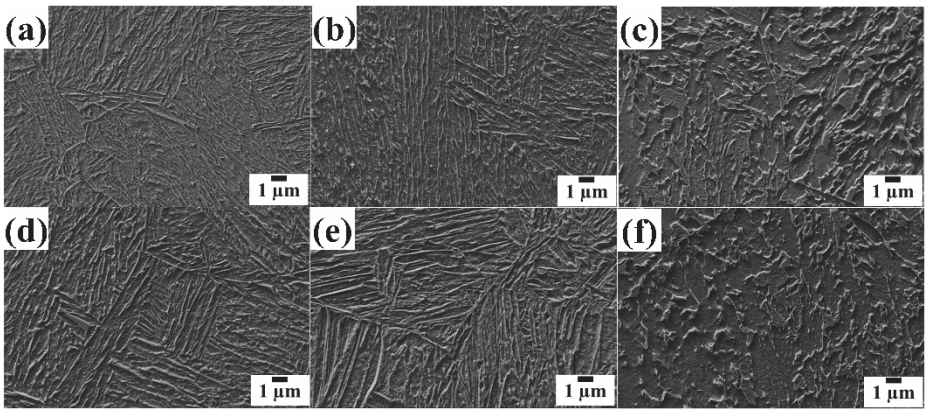

Fig. 63. Typical SEM micrographs of steel #1 (a, b, c) and steel #2 (d, e, f) with cooling rates of 60 (a, d), 1 (b, e) and 0.01 °C/s (c, f) respectively. Plane of micrographs is parallel to forged bar axis (Under CC BY license from Paper VI © 2019 Authors).

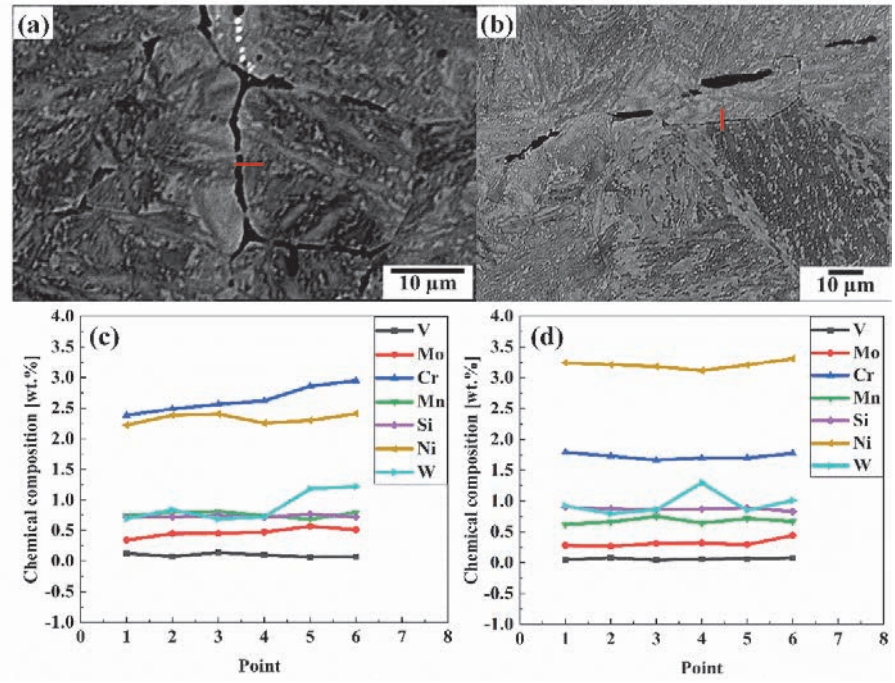

Fig. 64. EPMA micrograph and line analysis across grain boundaries of steel #1 (a, c) and steel #2 (b, d) with cooling rate of 0.01 °C/s (Under CC BY license from Paper VI © 2019 Authors).

Comparing to steel #1, the detected carbides at the PAG boundaries are substantially less frequent, as can be seen by comparing Fig. 65(a) and (b). This may result from the lower C and Cr contents of steel #2 compared to steel #1. Some of the observed carbides consist mainly of iron, in addition to very small amounts of Cr, W and Mo.

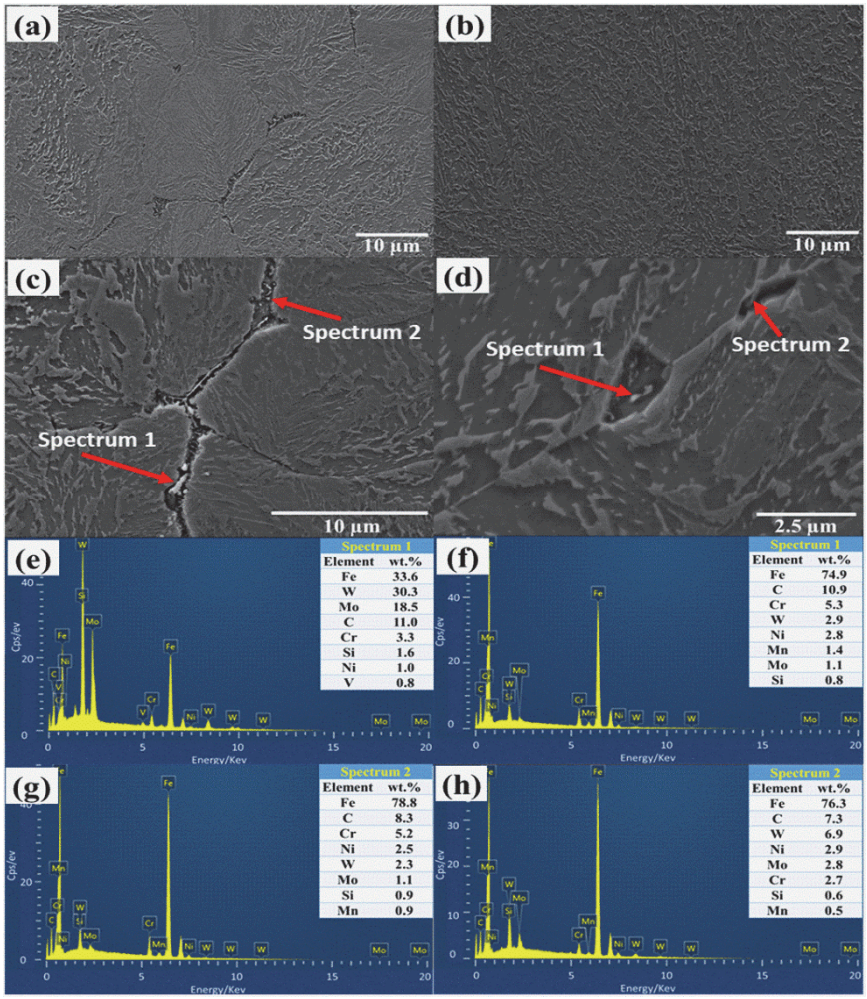

Fig. 65. Morphology and EDS analysis of carbides formed at prior austenite grain boundaries in steel #1 (a, c, e, g) and in steel #2 (b, d, f, h) at cooling rate from austenitization temperature (950 °C) of 0.01 °C/s (Under CC BY license from Paper VI © 2019 Authors).

The proeutectoid nature of the carbides observed at the PAG boundaries is confirmed by thermodynamic calculations using the commercial software Thermo-Calc together with the TCFE7 database, shown in Fig. 66. Also, the predicted volume fraction of carbides at 755 °C in equilibrium with austenite are given in Table 21. The compositional difference between steels #1 and #2 (especially in C and Cr contents) is apparent in the predicted equilibrium volume fractions and composition of the carbides. Although equilibrium compositions and volume fractions were not achieved during cooling at 0.01 °C/s, the relative volume fractions given in Table 21 agree with the observation that steel #1 has higher incidence of the proeutectoid carbides than steel #2.

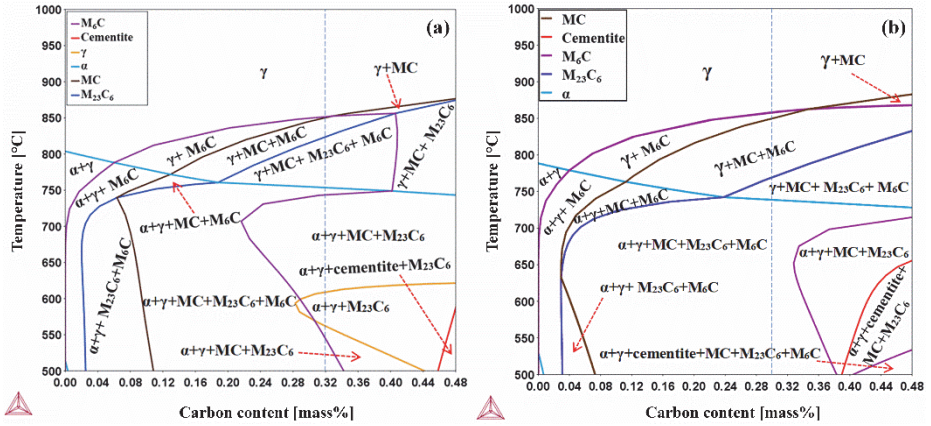

Fig. 66. Calculated equilibrium phase diagrams of steels #1 (a) and #2 (b) considering C, Cr, Ni, W, Mn, Mo and V. Dashed line indicates C content. γ austenite, α ferrite (Reprinted [adapted] under CC BY license from Paper VI © 2019 Authors).

Table 21. Predicted equilibrium precipitate volume fractions and compositions at 755 °C (Under CC BY license from Paper VI © 2019 Authors).

Carbides	Chemical constitution	Volume fraction of carbides [vol.%]	
		Steel #1	Steel #2
MC	$(V,W)_1\ (C)_1$	0.001	0.001
$M_{23}C_6$	$(Fe,Cr)_{20}\ (W,Mo)_3\ (C)_6$	0.018	0.004
M_6C	$(Fe)_2\ (W,Mo)_2\ (Fe,W,Mo,Cr)_2\ (C)_1$	0.002	0.006
Total		0.021	0.012

Combined IPF and IQ maps of the steels #1 and #2 with different CRs of 60, 1 and 0.01°C/s are shown in Fig. 67. Grain boundary misorientation distributions, lath

sizes, effective grain sizes and effective grain sizes at 90% in the cumulative grain size distribution for steels #1 and #2 at different CRs are given in Fig. 68. In addition, the reconstructed PAGS, volume fractions of retained austenite and their carbon contents are given in Table 22.

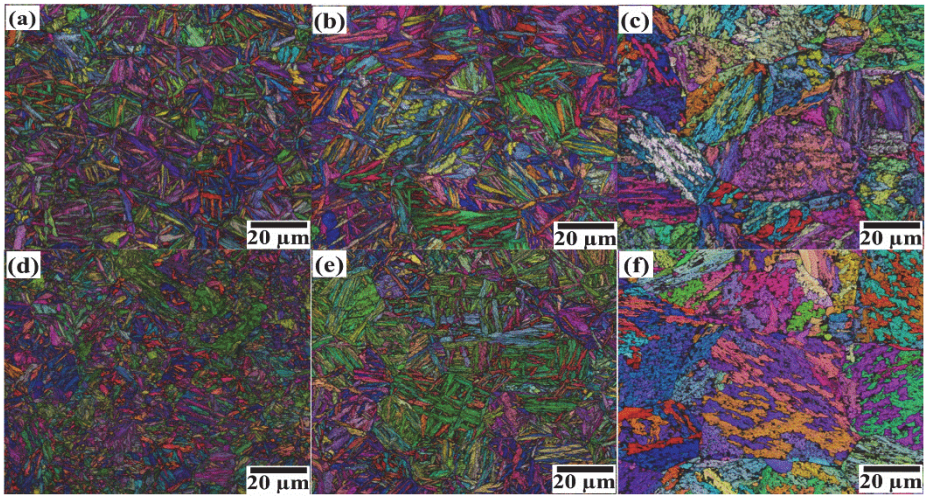

Fig. 67. Inverse pole figure (IPF) combined with image quality (IQ) map of steel #1 (a, b, c) and steel #2 (d, e, f) with CR of 60 (a, d), 1 (b, e) and 0.01 °C/s (c, f), respectively. Plane of micrographs is parallel to axis of forged bars (Under CC BY license from Paper VI © 2019 Authors).

Table 22. Prior austenite grain sizes (PAGS), volume fractions of RA (V_γ) and C_γ for investigated steels #1 and #2 at different cooling rates (Reprinted [adapted] under CC BY license from Paper VI © 2019 Authors).

Steel	Cooling rate [°C/s]	PAGS [1] [µm]	V_γ [2] [%]	C_γ [%]
#1	60	19.83 ± 1.40	4.60 ± 0.30	0.21
	1	26.18 ± 1.18	5.08 ± 0.19	0.41
	0.01	46.21 ± 7.57	17.16 ± 0.12	0.85
#2	60	35.53 ± 3.64	2.30 ± 1.10	0.36
	1	36.89 ± 1.76	2.33 ± 0.11	0.67
	0.01	55.04 ± 4.49	12.25 ± 0.11	0.82

[1] Error bars are 95% confidence intervals for mean value.

[2] Error bars are standard deviations.

In the case of steel #1 (see Fig. 67(a)–(c) and Fig. 68(a) and (c)), the change in the CR led to a significant change in the microstructural features. Fig. 68(a) shows a slight increase in the average ECD martensitic lath sizes from 0.88 to 0.98 µm when the CR decreased from 60 to 1 °C/s, while the effective (high-angle grain boundary) grain size increased from 1.04 to 1.23 µm. The $D90\%_{GA}$ increased from 4.8 to 6.9 µm when the CR decreased from 60 to 1 °C/s (see Fig. 68(a)).

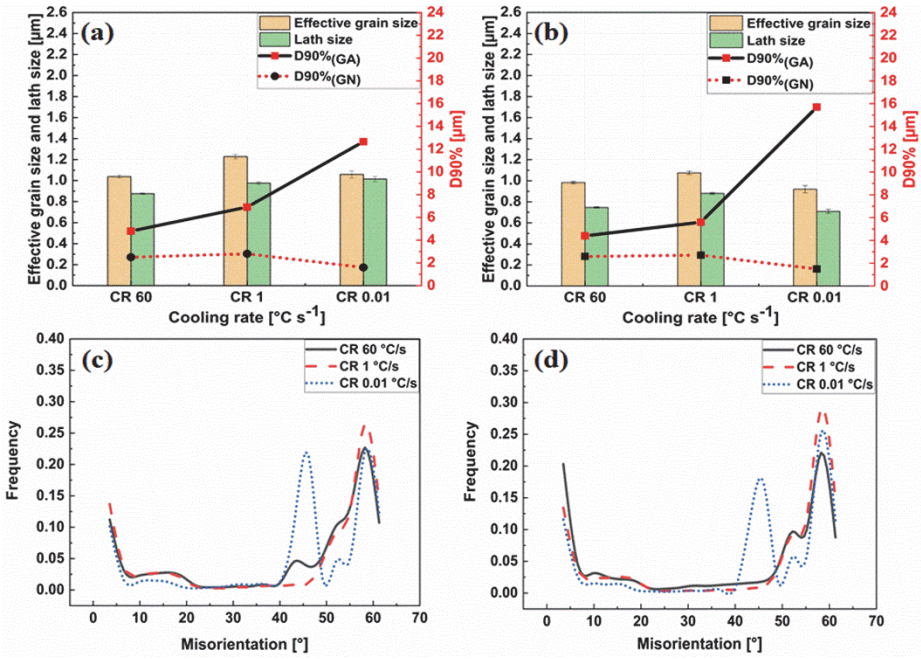

Fig. 68. Average lath size, average effective grain size and effective grain size at 90% in cumulative grain size distribution (a, b) together with grain boundary misorientation distributions (c, d) for steel #1 (a, c) and steel #2 (b, d) (Under CC BY license from Paper VI © 2019 Authors).

As can be seen from Table 22 and Fig. 69(a) and (b), the PAGS increased from 19.8 to 26.2 µm, resulting from the more extensive grain growth during the longer time at temperatures below 950 °C at the slower CR [139]. At the slowest CR of 0.01 °C/s, the above parameters are quite different, as PAGS increased significantly to 46.2 µm. The microstructure is now fully bainite, with the average ECD bainitic lath size, EGS and $D90\%_{GA}$ equal to 1.01, 1.06 and 12.65 µm, respectively. The opposite trends observed regarding the effect of CR on $D90\%_{GN}$ and $D90\%_{GA}$ for the two slowest CRs are due to the difference in the grain size distributions:

compared to CR of 1 °C/s, at 0.01 °C/s, the grain size distribution contains a larger number of small grains, which causes a reduction in $D90\%_{GN}$, as well as an increase in the size of the largest grains, which leads to an increase in $D90\%_{GA}$.

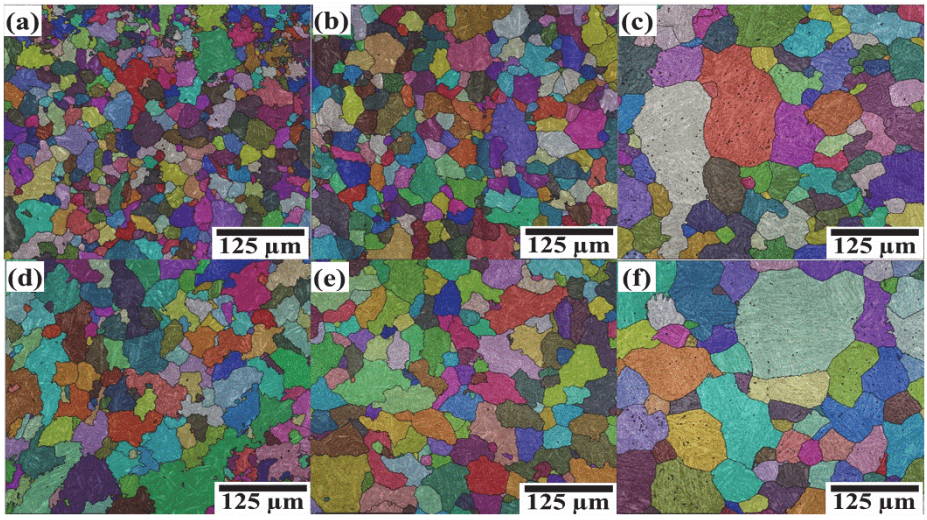

Fig. 69. Reconstructed PAG using EBSD results together with MTEX and MATLAB software for steel #1 (a, b, c) and steel #2 (d, e, f) with CRs of 60 (a, d), 1 (b, e), 0.01 °C/s (c, f). Plane of micrographs is parallel to axis of forged bars (Under CC BY license from Paper VI © 2019 Authors).

There was similar variation in the microstructural features of steel #2 as a result of changing the CR: as the CR decreases from 60 to 1 °C/s, the PAGS increased from 35.5 to 36.9 µm. The mean ECD martensitic lath size, EGS and $D90\%_{GA}$ increased from 0.75, 0.98 and 4.4 µm to 0.88, 1.08 and 5.6 µm respectively, while these microstructural features for the bainite obtained at the slowest CR become 0.71, 0.92 and 15.7 µm, respectively and PAGs is 55.0 µm. In the case of bainitic microstructure, the mean EGSs are smaller than those in the case of martensitic microstructures. This can be attributed to the strengthening of the austenite during transformation to bainite as its carbon content increases, which leads to a decrease in the bainite block size [161]. This effect can be seen in the higher frequency of high-angle boundary peaks in bainite compared to that in martensite (see Fig. 68(c) and (d)). Fig. 70 shows the variation in PAGS and $D90\%_{GA}$ as a result of CR. In both steels, PAGS and $D90\%_{GA}$ increased sharply with decreasing the CR. Also, there is a strong correlation between PAGS and $D90\%_{GA}$ which can be seen from

Fig. 70. These results are in a good agreement with those commonly reported about the reduction in block and packet size as a result of PAGS refinement [162]. The variation in PAGS (see Table 22) is presumably because of the large time difference that the austenite spends at high temperatures before the phase transformations start. For example, decreasing the temperature from 950 to 900 °C requires 83, 0.83 and 0.016 min for CRs of 0.01, 1 and 60 °C/s, respectively.

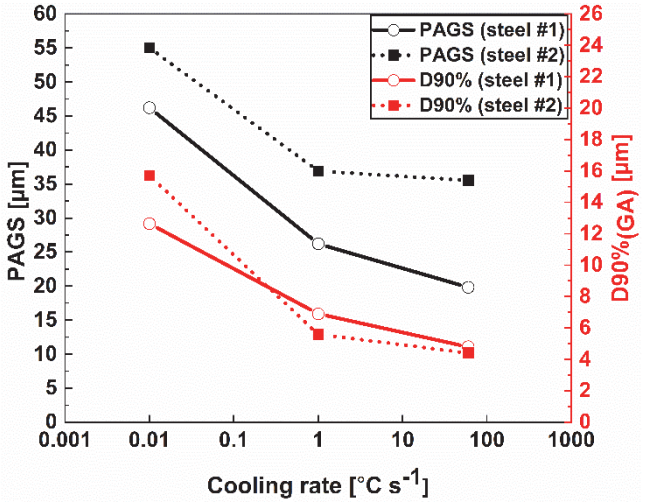

Fig. 70. Influence of cooling rate on PAGS and D90%$_{GA}$ of steel #1 and steel #2 (Reprinted [adapted] under CC BY license from Paper VI © 2019 Authors).

For steels #1 and #2, the lath and mean effective grain sizes are slightly influenced by the CR; they mainly depend on the type of microstructure formed and not on the changes in PAGS [163]. In the case of the fully martensitic structures, they increased slightly when the CR decreased from 60 to 1 °C/s. However, the formation of bainite at 0.01 °C/s led to a reduction in their values. There is a strong correlation between PAGS and D90%$_{GA}$, which increased sharply when CR was at its lowest. From Fig. 68(a) and (b), while the PAG sizes of steel #1 are smaller than those of steel #2, the lath and mean effective grain sizes are larger in steel #1 than those in steel #2, which confirms the above conclusion that the dependency of the lath and mean effective grain sizes is on the chemical composition and whether bainite or martensite forms, and not on the PAGS.

In the case of martensitic microstructures formed at 60 and 1 °C/s, RA percentage is small and practically independent of CR (see Fig. 71 and Table 22), but when the microstructure is bainite, significant amounts of RA are detected. In

bainitic microstructure, the formation of RA is assisted by various factors which increase the stability of austenite and reduce its probability for full transformation, such as i) the presence of approximately 0.6 wt.% Si in the steel, known to reduce the kinetics of cementite precipitation from austenite [164]–[166], ii) the very slow CR, which gives more time for carbon diffusion into and within the austenite [167], [168], iii) the presence of Ni [169] and iv) the presence of the granular bainite [170].

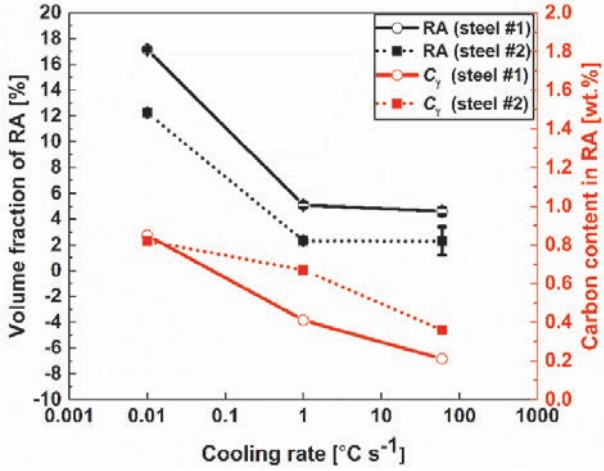

Fig. 71. Influence of cooling rates on volume fraction of RA and its carbon content for steel #1 and #2 (Reprinted [adapted] under CC BY license from Paper VI © 2019 Authors).

4.4.4 Microstructure of UHSSs after single and double austenitization and quenching followed by tempering

Grain structure

Figs. 72 and 73 show the microstructures of steels #1 and #4 after SAQT and DAQT. The microstructure of steel #1 after single austenitization and quenching followed by tempering (steel #1-SAQT), and after double austenitization and quenching followed by tempering (steel #1-DAQT), consists mainly of tempered martensite with a small fraction of finely distributed precipitates and small fraction of RA. The same is true for steel #4-SAQT and steel #4-DAQT, but they contain a lower volume fraction of precipitates due to its lower C content. Table 23 gives the volume fractions of RA in all the microstructures. In both steel compositions, the volume fraction of RA increases via the double austenitization processing route. As

illustrated below, these increases in the volume fraction of RA are induced by the enhanced precipitate dissolution that occurs during the first high-temperature austenitization, which increases the concentration of alloying elements and carbon in the matrix, leading to a reduction in the transformation temperature and the probability of complete transformation [171], [172]. The reconstructed PAG structures are shown in Fig. 74, and PAGS expressed as the mean ECD are given in Table 23. In steels #1 and #4, it can be seen that the double austenitization increases the PAGS (see Table 23) due to the reduction of the grain boundary pinning effect resulting from the precipitate dissolution in the first austenitization [172].

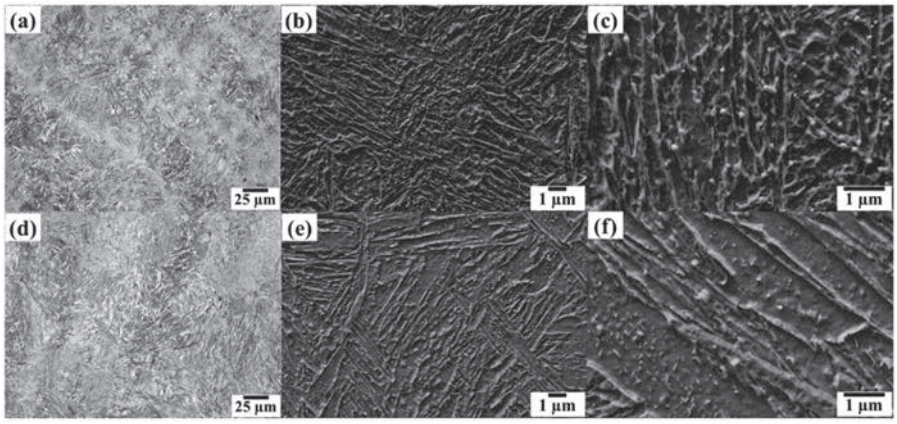

Fig. 72. LSCM micrograph and SEM micrograph of steel #1-SAQT (a, b, c) and steel #1-DAQT (d, e, f) (Under CC BY-NC-ND license from Paper VII © 2019 Authors).

Table 23. Transformation temperatures, volume fractions of RA and PAGS (Under CC BY-NC-ND license from Paper VII © 2019 Authors).

Steel Code	Transformation Temperatures [1] [°C]		RA [2] [%]	PAGS [3] [µm]
	M_s	M_f		
Steel #1-SAQT	429	144	1.85 ± 0.09	33 ± 1
Steel #1-DAQT			6.10 ± 0.18	49 ± 2
Steel #4-SAQT	444	220	1.70 ± 0.40	22 ± 1
Steel #4-DAQT			3.00 ± 0.30	29 ± 1

[1]Values are determined from dilatation curves measured using a Gleeble 3800 thermomechanical simulator.

[2] Error bars are standard deviations

[3] Linear intercept values from the reconstructed prior austenite grains in Fig. 74.

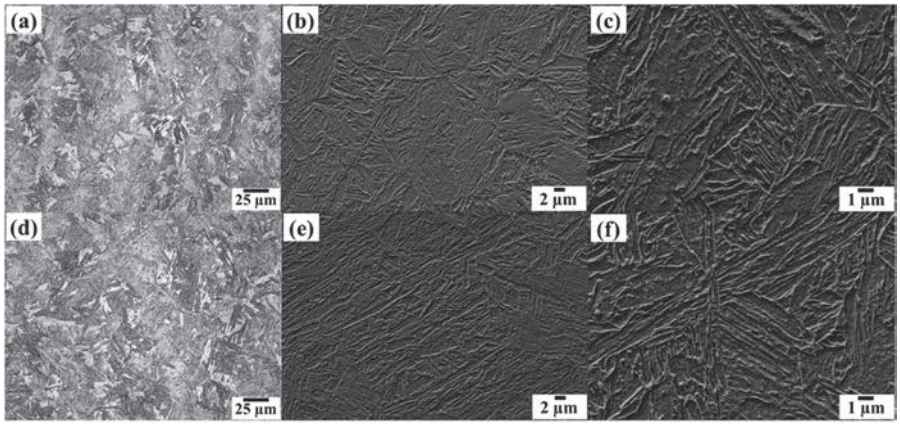

Fig. 73. LSCM micrograph and SEM micrograph of steel #4-SAQT (a, b, c) and steel #4-DAQT (d, e, f) (Under CC BY-NC-ND license from Paper VII © 2019 Authors).

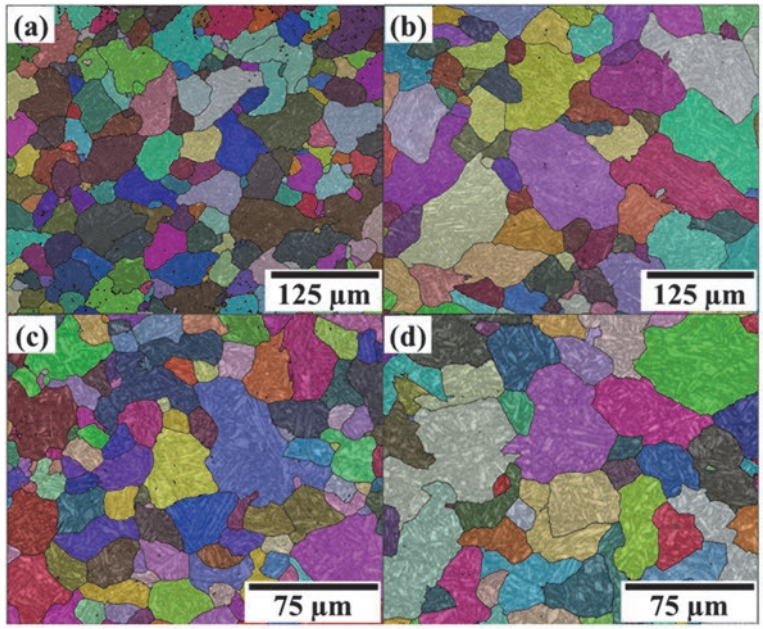

Fig. 74. PAG structures obtained by analysing EBSD data with MTEX and MATLAB software. a) steel #1-SAQT, b) steel #1- DAQT, c) steel #4-SAQT and d) steel #4-DAQT. The plane of the micrographs is parallel to the axis of the forged bar. The images shown are combinations of austenite orientation with image quality (Under CC BY-NC-ND license from Paper VII © 2019 Authors).

In the case of steel #1, as shown in Fig. 75, double austenitization has no effect on the average ECD martensitic lath size or mean effective (high-angle grain boundary) grain size, even though there is a large increase in the PAGS. However, the value of $D90\%_{GA}$ is almost threefold (see Fig. 75(d)). Fig. 75(c) shows that the double austenitization is seen to raise the frequency of low and high misorientation angles while decreasing the frequency of intermediate misorientation angles (30°–50°).

Despite the small increase in the PAGS in the case of steel #4 as a result of double austenitization, Fig. 76 shows increases in the average ECD martensitic lath size and the mean effective grain size. Also, there is a moderate increment in the value of $D90\%_{GA}$.

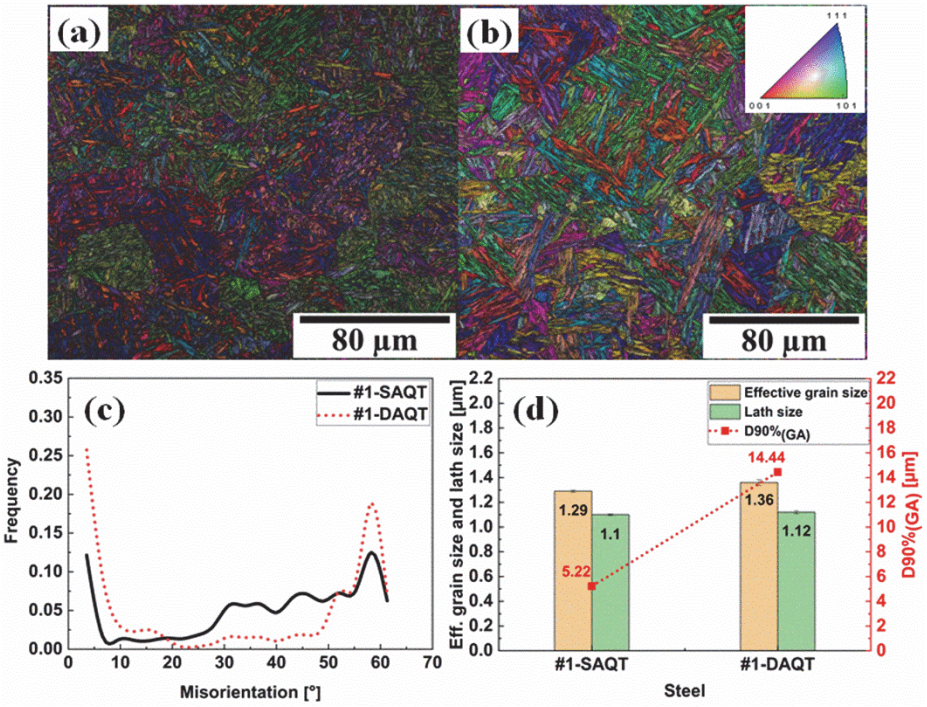

Fig. 75. Grain structure of steel #1. a) and b) Inverse pole figure (IPF) with superimposed image quality (IQ) maps, a) steel #1-SAQT and b) steel #1-DAQT. c) Grain boundary misorientation distributions. d) Average lath size, average effective grain size and effective grain size at 90 % in the cumulative grain size distribution. The plane of the micrographs is parallel to the axis of the forged bar (Under CC BY-NC-ND license from Paper VII © 2019 Authors).

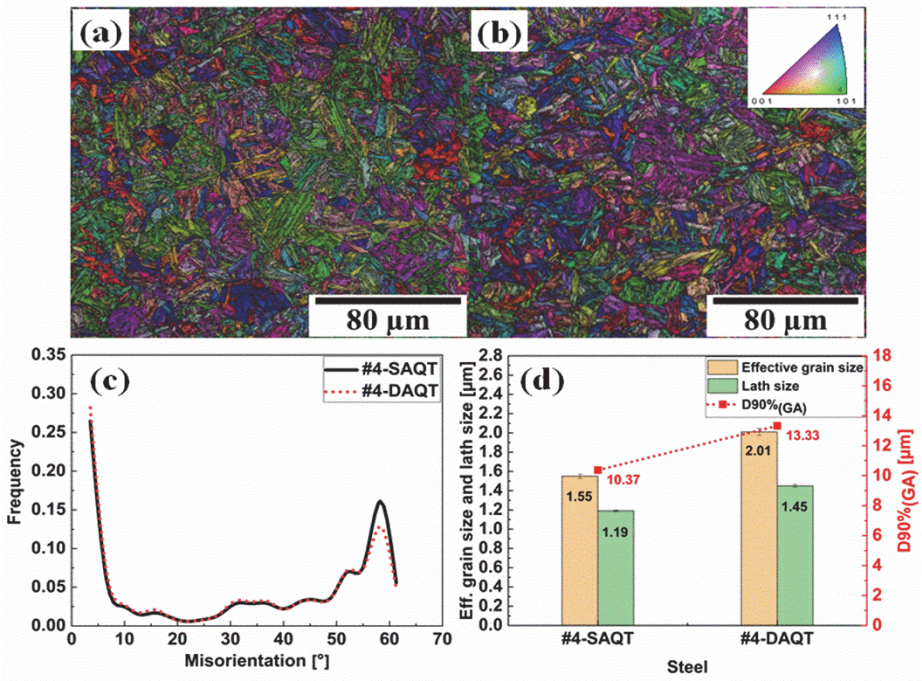

Fig. 76. Grain structure of steel #4. a) and b) Inverse pole figure (IPF) with superimposed IQ maps, a) steel #4-SAQT and b) steel #4-DAQT. c) Grain boundary misorientation distributions. d) Average lath size, average effective grain size and effective grain size at 90 % in the cumulative grain size distribution. The plane of the micrographs is parallel to the axis of the forged bar (Under CC BY-NC-ND license from Paper VII © 2019 Authors).

As illustrated further below, the higher nitrogen content of steel #4 compared to steel #1 leads to increased pinning by AlN, which gives a smaller increase of the PAGS in steel #4 compared to steel #1. There is a direct relationship between the PAGS and $D90\%_{GA}$, which was also observed in Paper VI and discussed in Section 4.4.3, as the large increase in the PAGS in the case of steel #1 is accompanied by a large increase in $D90\%_{GA}$, while the small increase in PAGS is accompanied by a small increase of $D90\%_{GA}$ in the case of steel #4. However, the changes in the ECD martensitic lath size and the mean effective grain size are attributed to the differences in the transformation temperatures, i.e. M_s and M_f, as decreasing M_s and M_f cause finer lath and effective grain sizes.

Size and frequency of precipitates

Fig. 77 and Fig. 78 show typical TEM micrographs showing the distribution and morphologies of the precipitates and their statistics in steels #1 and #4. In steel #1 (see Fig. 77), compared to the single austenitization, double austenitization has little effect on the mean extracted precipitate equivalent circle diameter. In the case of steel #4, there was generally a lower frequency of precipitates on the extraction replicas compared to steel #1, due to the lower carbon content of steel #4. In this case, double austenitization led to an increase in the frequency of fine precipitates, less than 30 nm in equivalent circle diameter and a reduction in the size of the largest precipitates (see Fig. 78).

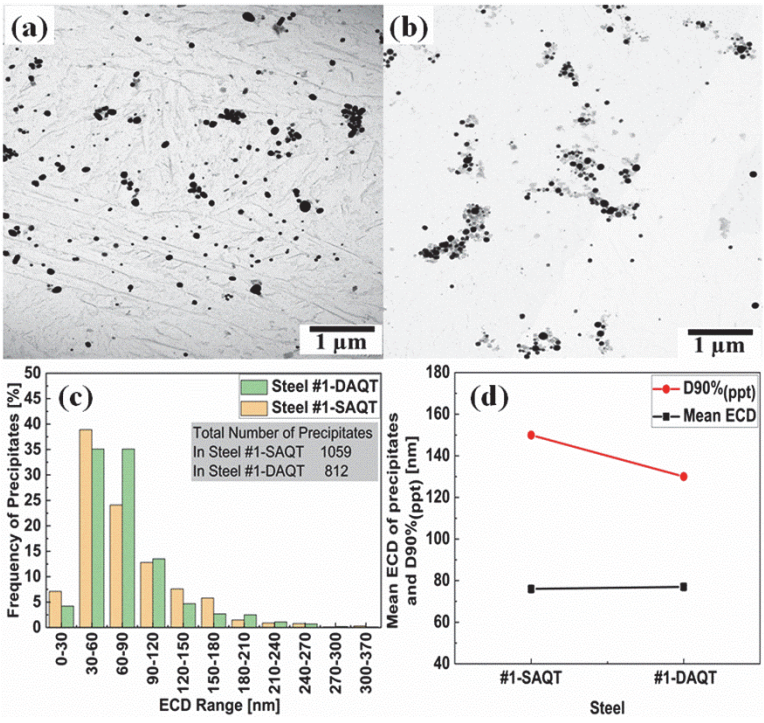

Fig. 77. Typical STEM micrographs of carbon extraction replicas for the distribution and morphologies of the precipitates for steel #1-SAQT (a) and steel #1-DAQT (b) and their statistics including size distributions (c) and mean sizes and the precipitate size at 90 % in the cumulative size distribution ($D90\%_{ppt}$) (d) (Under CC BY-NC-ND license from Paper VII © 2019 Authors).

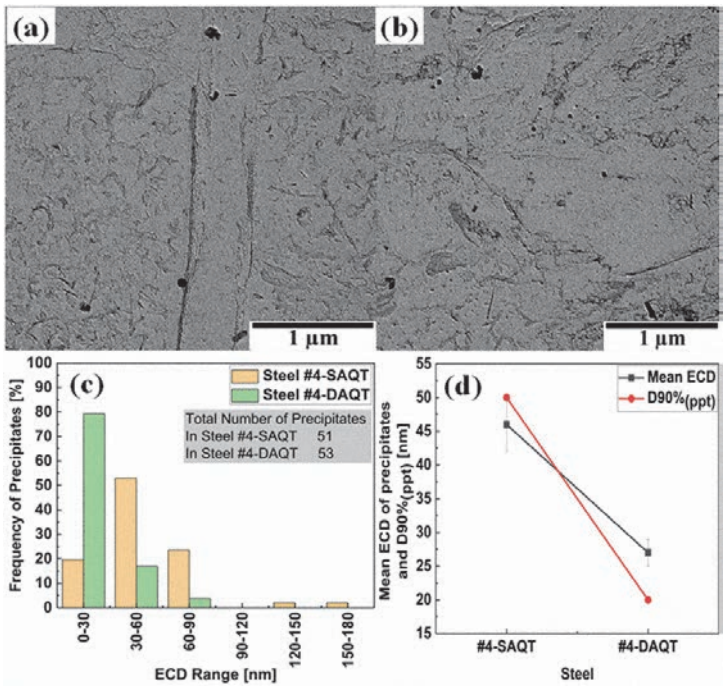

Fig. 78. Typical STEM micrographs of carbon extraction replicas for the distribution and morphologies of the precipitates for steel #4-SAQT (a) and steel #4-DAQT (b) and their statistics including size distributions (c) and mean sizes, volume fractions and the precipitate size at 90% in the cumulative size distribution ($D90\%_{ppt}$) (d) (Under CC BY-NC-ND license from Paper VII © 2019 Authors).

Chemical composition of the precipitates

According to EDS analyses, the precipitates in steel #1 after SAQT and DAQT treatment can be subdivided into four types, as can be seen from Table 24 and Fig. 79 (P1, P2, P3 and P4). Those include complex carbides M_xC_y, where M refers to Fe, Mo, W and Cr, aluminium nitride AlN, AlN with a core of (TiV)(CN) and complex (TiV)(CN) containing a few atomic percent of W, Mo and Nb. M_xC_y represent the most common precipitate type after both treatments, followed by AlN, (TiV)(CN) and complex AlN-(TiV)(CN).

In steel #4, EDS indicates that the main types of the precipitates after SAQT treatment are mainly AlN and (TiV)(CV), in addition to a few complex carbides M_xC_y. Similar types of precipitates have been observed after DAQT treatment in addition to a very small fraction of vanadium carbonitride type V(CN), as can be

seen from Fig. 79 (P5). Salunkhe et al. [173] has reported that in the presence of V, Ti(C,N) rarely exists alone, as it usually acts as a nucleation site for (Ti,V)(C,N).

Table 24. Compositions of different precipitate types (at.% and wt.%) (Under CC BY-NC-ND license from Paper VII © 2019 Authors).

Steel	Type	Composition	C	N	O	Al	Si	Ti	V	Cr	Fe	Nb	Mo	W
P1	M_xC_y	at. %	14.56	-	-	-	-	0.14	-	5.90	39.10	-	21.59	18.71
		wt.%	2.14	-	-	-	-	0.08	-	3.75	26.68	-	25.31	42.04
P2	AlN	at. %	21.31	36.74	-	41.57	0.38	-	-	-	-	-	-	-
		wt.%	13.45	27.05	-	58.94	0.56	-	-	-	-	-	-	-
P3	AlN-(TiV)CN	at. %	39.36	32.35	-	17.64	-	6.59	1.37	0.68	0.59	-	0.81	0.60
		wt.%	23.13	22.17	-	23.29	-	15.44	3.41	1.73	1.61	-	3.81	5.42
P4	(TiV)(CN)	at. %	70.08	7.29	6.55	-	-	7.14	4.96	-	-	1.68	1.10	1.20
		wt.%	39.61	4.81	4.93	-	-	16.09	11.90	-	-	7.35	4.97	10.36
P5	(V)CN	at. %	63.03	24.44	-	-	-	-	12.54	-	-	-	-	-
		wt.%	43.56	19.69	-	-	-	-	36.75	-	-	-	-	-

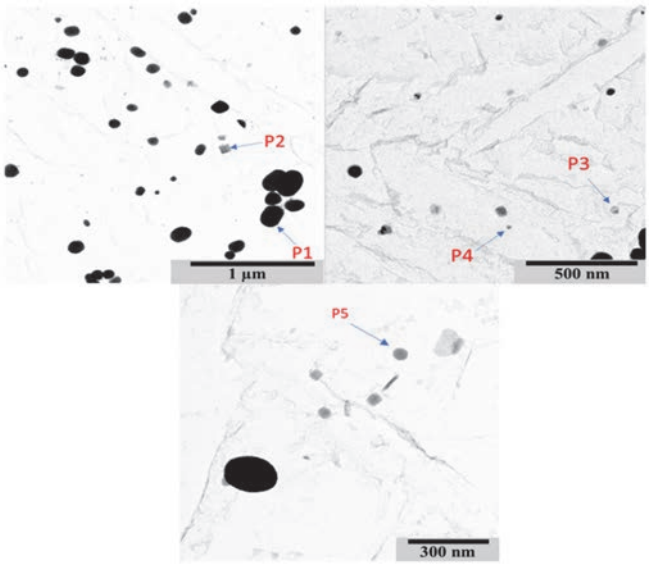

Fig. 79. Typical STEM micrographs of carbon extraction replicas for precipitates in the steels #1 and #4, (P1) complex carbides M_xC_y, (P2) aluminium nitride AlN, (P3) complex AlN with a core of (TiV)(CN), (P4) complex (TiV)(CN) with a few atomic percentages of W, Mo and Nb and (P5) vanadium carbonitride V(CN) (Under CC BY-NC-ND license from Paper VII © 2019 Authors).

Thermodynamic calculations of the precipitates

Fig. 80 and Fig. 81 show the thermodynamic calculations made using the commercial software Thermo-Calc version 2018a together with the database TCFE9. The precipitate phases in equilibrium with austenite and ferrite in the case of steel #1 include $M_{23}C_6$, M_6C, VC, AlN, TiN and (Nb,Ti)C, while in the case of steel #4 include $M_{23}C_6$, M_6C, V(C,N), AlN, TiN and NbC.

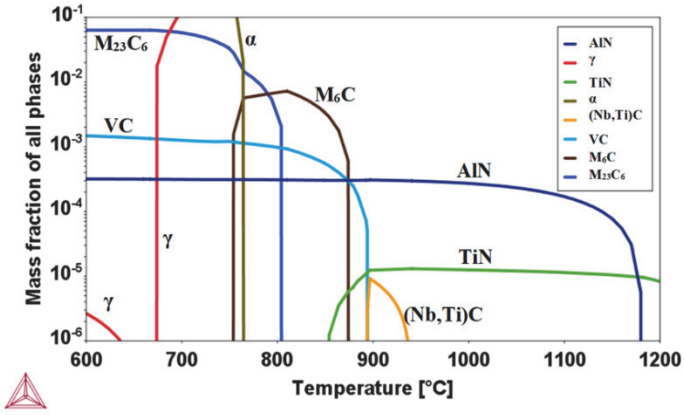

Fig. 80. Thermodynamic calculations for precipitates types in steel #1 (Under CC BY-NC-ND license from Paper VII © 2019 Authors).

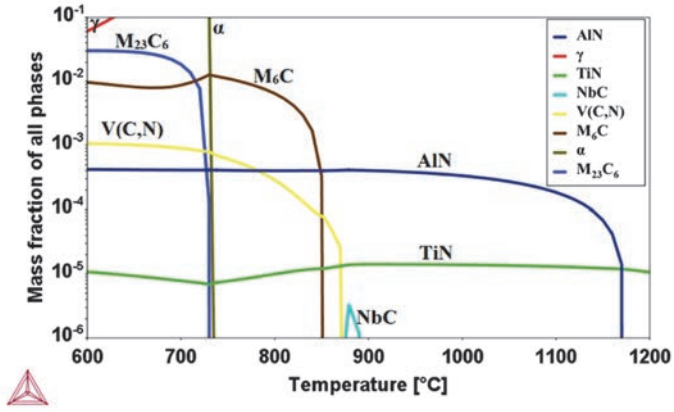

Fig. 81. Thermodynamic calculations for precipitates types in steel #4 (Under CC BY-NC-ND license from Paper VII © 2019 Authors).

Considering the history of the thermomechanical and heat treatment of the materials and the results discussed in section 4.4.2, only TiN and AlN are expected to present after holding at 930 or 1100 °C. Under equilibrium conditions, precipitates formed during air cooling after hot forging would be dissolved or changed during the heating and holding at these temperatures. Additionally, the final low-temperature tempering is not expected to result in carbide compositions involving the diffusion of substitutional alloying elements. So, the observed presence of complex carbide M_xC_y in the steels #1 and #4 implies incomplete dissolution of the primary carbides formed during solidification. These results are in a good agreement with Nurbanasari et al. [174], who reported that Thermo-Calc predictions suggest that the only stable phase is austenite while the primary carbides are left undissolved in H21 tool steel even after high temperature austenitization at 1250 °C.

4.5 Mechanical properties characterization

Paper II and IV investigated the mechanical properties of steels #1, #2, #3 and #4 without and with ESR. Paper VI examined the variation in the mechanical properties as a result of changing the CR and steel composition using steels #1 and #2. Paper VII investigated the effect of different heat treatment, including SAQT and DAQT treatments, on the mechanical properties.

4.5.1 Effect of ESR on mechanical properties

The mechanical properties of steels #1, #2, #3 and #4 with and without ESR are given in Table 25. It is clear that there are no simple trends resulting from ESR. This is to be expected, as the mechanical properties are a complex result of the combined influence of chemical composition and processing parameters on the final microstructure, as discussed below. Besides microstructure, cleanliness affects the toughness of steel significantly.

Various contributions to the yield strength, including the contribution from lath refinement strengthening (σ_L), precipitation strengthening (σ_P) and dislocation density strengthening (σ_D), have been calculated, and the results are given in Table 26. More details about the calculation methods are given in Paper IV.

Table 25. Tensile properties, Charpy-V notch impact toughness and hardness of steels #1, #2, #3 and #4 without and with ESR [Paper II], [Paper IV] (Reprinted [adapted] under CC BY license from Paper IV © 2020 Authors).

Steel	Process	Tensile properties			Charpy V test at room temperature		Hardness	
		UTS [1] [MPa]	YS [1] [MPa]	El. [1] [%]	Absorbed energy [1] [J]	Ductile fracture [2] [%]	HV10 [1]	Calculated Hardness for full martensite [3]
#1	IF	1872 ± 14.63	1145 ± 23.07	12 ± 1.33	24 ± 0.5	30	548 ± 6	558
	ESR	1978 ± 32.70	1277 ± 14.14	14 ± 0.15	25 ± 0.5	34	595 ± 5	576
#2	IF	1744 ± 9.99	1019 ± 1.29	13 ± 0.47	33 ± 0.0	52	514 ± 11	514
	ESR	1773 ± 1.53	1233 ± 10.45	15 ± 1.08	40 ± 0.0	56	526 ± 3	567
#3	IF	1729 ± 6.82	1153 ± 17.14	18 ± 0.16	36 ± 0.5	59	532 ± 10	514
	ESR	2007 ± 7.74	1216 ± 17.20	14 ± 0.25	27 ± 1.0	30	562 ± 13	549
#4	IF	1353 ± 9.06	921 ± 5.47	19 ± 0.58	53 ± 3.5	69	411 ± 4	426
	ESR	1265 ± 13.08	831 ± 19.99	21 ± 0.52	67 ± 2.5	72	386 ± 3	452

[1] Error bars are standard deviations from the mean.

[2] Ductile fracture % was calculated according to ASTM A 370-11.

[3] The hardness values for full martensitic structure have been calculated using the following equation [175]: HV (martensite) = $884C - (1 - 0.3C^2) + 294$ where C is the carbon content in wt. %.

Table 26. Contributions to yield strength [Paper II], [Paper IV] (Reprinted [adapted] under CC BY license from Paper IV © 2020 Authors).

Steel	Process	σ_L [MPa]	Increment due to ESR [MPa]	σ_P [MPa]	Increment due to ESR [MPa]	Dislocation Density [m $^{-2}$]	Dislocation σ_D [MPa]	Increment due to ESR [MPa]
#1	IF	54	23	84	1	1.75 x 10 15	201	4
	ESR	78		85		1.82 x 10 15	205	
#2	IF	69	6	85	6	1.58 x 10 15	190	12
	ESR	75		91		1.79 x 10 15	203	
#3	IF	72	66	90	16	1.58 x 10 15	190	8
	ESR	137		106		1.72 x 10 15	199	
#4	IF	59	13	78	16	1.23 x 10 15	168	7
	ESR	72		93		1.33 x 10 15	175	

Changes in the mechanical properties of steel #1

In the case of steel #1, a student's t-test analysis of the data given in Table 25 showed that ESR led to increased UTS, YS and hardness. But there is no significant variation in the elongation to fracture and Charpy V-notch (CVN) impact toughness.

The increment in the UTS, YS and hardness may be caused by several interrelated parameters, and it is hard to distinguish between the effects of these parameters. Increasing the carbon content from 0.30 to 0.32% as a result of ESR could be one of the reasons for strengthening the martensite and increasing the strength and hardness values. In ESR, the high CR results in solution hardening and improves the strength and hardenability by reducing the size of the precipitates through decreasing the diffusion of the alloying elements and increasing dissolution of the alloying elements in the matrix. Furthermore, refinement of the PAGS, effective grain size and lath size will increase the values of strength and hardness. The presence of AlN and TiN precipitates formed during the forging may be the main reason for the refinement of the PAGS, as discussed in section 4.4.1 and 4.4.2. These could produce Zener pinning effects that hinder the growth of the PAG. In addition, an increase in the volume fraction of RA may contribute to enhancing the UTS as a result of its transformation to martensite through the TRIP effect. In addition to the microstructure refinement and precipitation strengthening, the dislocation density will contribute to increasing the yield strength via dislocation strengthening mechanism. The calculated incremental contributions to the yield strength as a result of ESR from σ_L, σ_P and σ_D were 23 MPa, 1 MPa and 4 MPa respectively, as can be seen from Table 26. The residual 104 MPa from the total

enhancement of the yield strength as a result of ESR may be caused by the refinement of the PAGS [18], [176] and the effective grain size [176], [177], and the slight increase in the content of carbon from 0.30 to 0.32%, as most of the strength of martensite is perhaps due to the segregated carbon atoms [71]. Therefore, probably most of the increment in the yield strength as a result of ESR is due to the slight increase in the carbon content.

While there is a large increment in the UTS, YS and hardness as a result of ESR, the elongation and impact toughness have the same values, or they increased slightly. Also, there is a slight increment in the percentage of ductile fracture, as can be seen from Table 25. This is because of the high degree of refining with ESR, as discussed in section 4.1.2 and 4.2, in which the total impurity level reduced with ESR by 46%, and, also, removal of most MnS, which has the most detrimental effects on the ductility and toughness. Some of the MnS are nucleated and grown on some oxide or nitride inclusions, leading to smaller size multiphase inclusions with an oxide or nitride core surrounded by sulphide, e.g. ($MnS.Al_2O_3$), ($MnS.TiN.Al_2O_3$), ($MnS.CaO.Al_2O_3$), ($MnS.TiO_2$), (MnS.TiN), (MnS.(TiV)N) and (MnS.TiON) with the modified (Ca.Mn)S and $CaS.Al_2O_3$. These newly formed NMIs have more resistance for deformation than MnS, which also enhances the impact toughness. Additionally, removal of hard and large oxides inclusions which have a low deformability index, and have and occupy large area fractions, e.g. ($Al_2O_3.SiO_2$), ($MnO.Al_2O_3.SiO_2$), ($MnO.SiO_2$), ($CaO.MnO.Al_2O_3.SiO_2$), ($MnS.Al_2O_3.SiO_2$), ($MnS.SiO_2$), or converted to other modified inclusions with a lower melting point, such as $xCaO.yAl_2O_3$, has the main reason of preventing deterioration of the impact toughness and elongation to fracture properties. Moreover, refinement of the effective grain size leads to an increase in the high angle grain boundaries that the cracks need to pass through, which increases the required energy and thereby prevents the deterioration in the impact toughness, or even enhances it.

However, there is no increase in the impact toughness as a result of ESR, which may be due to increasing aluminium content and the area fraction of Al_2O_3 particles by 85% and 95%, respectively, with ESR as a result of Al deoxidant addition at the beginning or during the experiment. Furthermore, the presence of TiN with ESR in the complex multiphase inclusions like (TiV)N ($MnS.TiN.Al_2O_3$), (MnS.TiN), (MnS.(TiV)N), ($TiN.Al_2O_3$) and (TiON.MnS) can be one of the reasons which prevents an increase in the impact toughness, although there is a high degree of refining in the microstructure features. This is because of the TiN inclusions

characterizes with large blocky cubic morphology and cracks initiate easily at the its sharp corner, or in the TiN particles itself because of its brittleness [178].

Changes in the mechanical properties of steel #2

In the case of steel #2, a student's t-test analysis of the data given in Table 25 showed that ESR led to a significant increase in YS and CVN impact toughness.

The significant improvement in the YS and the slight increment in the UTS and hardness are attributed to different interrelated parameters, including: i) increase in the carbon content from 0.25 to 0.31% as a result of ESR, which represents the main reason for increasing the strength and the hardness value via strengthening of the martensite, ii) the refinement of the lath size will also contribute to the YS [179]–[181], and iii) dislocation strengthening. The calculated incremental contributions to the yield strength as a result of ESR from σ_L, σ_P and σ_D, given in Table 26, show an expected increment in the yield strength of about 24 MPa. The remaining 190 MPa from the total actual increase in the yield strength after ESR is mainly from the increase in carbon content from 0.25 to 0.31%. Because of the segregation of carbon atoms to the lath boundaries and dislocations, some studies [64], [71] showed that the yield strength of martensite increases in proportion to the square root of the carbon content according to equation

$$\sigma_{0.2}\ (\text{MPa}) = 413 + 1.72 \text{ x } 10^3\ (\text{wt.\% C})^{1/2}. \qquad (38)$$

Moreover, this represents the main single parameter controlling the strength of as-quenched martensite. In addition, the slight increment in the UTS and the ductility may result from increasing the volume fraction of RA as a result of ESR, as illustrated in Table 13, through the TRIP effect [176], [182], [183].

The improvement in the impact toughness as a result of ESR is attributed to different parameters: i) decreasing the TIL and the area fraction of NMIs larger than 3 μm and modification of some inclusions by Ca, as discussed in section 4.2, ii) increasing the volume fraction of RA (given in Table 13), eliminating the deterioration of the toughness which is normally associated with the increase in the strength properties [176], [182], [183], and iii) the slight refining of the PAGS (given in Table 13) [184], [185].

Changes in the mechanical properties of steel #3

In the case of steel #3, a student's t-test analysis of the data given in Table 25 showed that ESR led to an increase in UTS, YS and hardness values. However, it led to a decrease in the elongation to fracture and CVN impact toughness (see Table 25). The calculated incremental contributions to the yield strength as a result of ESR from σ_L, σ_P and σ_D, given in Table 26, show an expected increment in the yield strength of about 91 MPa, which is close to the actual increase of 63 MPa. The decrement in elongation to fracture and CVN impact toughness are natural consequences of the large increase in the UTS and are, perhaps, in combination with the presence of Al_2O_3 inclusions which formed as a result of ESR.

Changes in the mechanical properties of steel #4

In contrast to the predicted increase in the hardenability and strength due to ESR, there is a major difference in the mechanical properties of this steel as a result of ESR, as UTS, YS and hardness are decreased (see Table 25). However, elongation to fracture and CVN impact toughness are improved, as can be seen from Table 25.

Increasing the volume fraction of bainite, as discussed in section 4.4.1, from 54% to 66% with ESR represents the main reason for the decrease in the tensile properties and hardness, while the elongation and impact toughness (see Table 25) were increased because of the refinement of the martensitic and bainitic structure, i.e. the effective grain and lath sizes (discussed in section 4.4.1). Decreasing the effective grain size leads to an increase in the high angle boundaries, which is confirmed by the slight increasing in the peak of misorientation at 58°. This leads to an increase in the work needed to propagate the initiated cracks across its high angle grain boundaries as a result of changing the crystallographic orientation and the crack direction when a crack starts to propagate across the high angle boundary [186]. This leads to enhancing the CVN impact toughness.

4.5.2 Effect of chemical composition and cooling rate on mechanical properties

Table 27 and Fig. 82 give the mechanical properties of steel #1 and #2 after the thermal cycles (shown in Fig. 9) with CRs of 60, 1 and 0.01°C/s. Fig. 83 shows the variation in the mechanical properties with the temperatures for 50%

transformation. As commonly observed [163], the UTS, YS and hardness are improved as the transformation temperature drops with increasing the CR.

Table 27. Tensile properties, Charpy-V notch impact toughness and hardness of steels #1 and #2 with cooling rates of 60, 1 and 0.01 °C/s (Reprinted [adapted] under CC BY license from Paper VI © 2019 Authors).

Steel	Cooling rate	Tensile properties			Charpy V test at room temperature		Charpy V test at -40°C		Hardness [3]
	[°C/s]	UTS [1]	YS [1]	El. [1]	Absorbed energy [1]	Ductile fracture [2]	Absorbed energy [1]	Ductile fracture [2]	[HV10]
		[MPa]	[MPa]	[%]	[J/cm^2]	[%]	[J/cm^2]	[%]	
#1	0.01	1417 ± 3	800 ± 11	14 ± 0	21 ± 2	34	14 ± 0	11	417 ± 5
	1	1978 ± 16	1205 ± 65	8 ± 1	24 ± 2	43	18 ± 0	29	578 ± 3
	60	2109 ± 2	1343 ± 86	7 ± 2	18 ± 0	29	14 ± 0	20	635 ± 6
#2	0.01	1351 ± 10	793 ± 19	19 ± 0	24 ± 0	25	15 ± 1	11	394 ± 4
	1	1786 ± 7	1095 ± 13	9 ± 1	27 ± 1	51	21 ± 1	45	535 ± 3
	60	1896 ± 30	1292 ± 38	10 ± 2	23 ± 1	39	17 ± 1	33	582 ± 4

[1] Error bars are standard deviations of three measurements.

[2] Ductile fracture % was calculated according to ASTM A 370-11.

[3] Error bars are standard deviations of ten measurement.

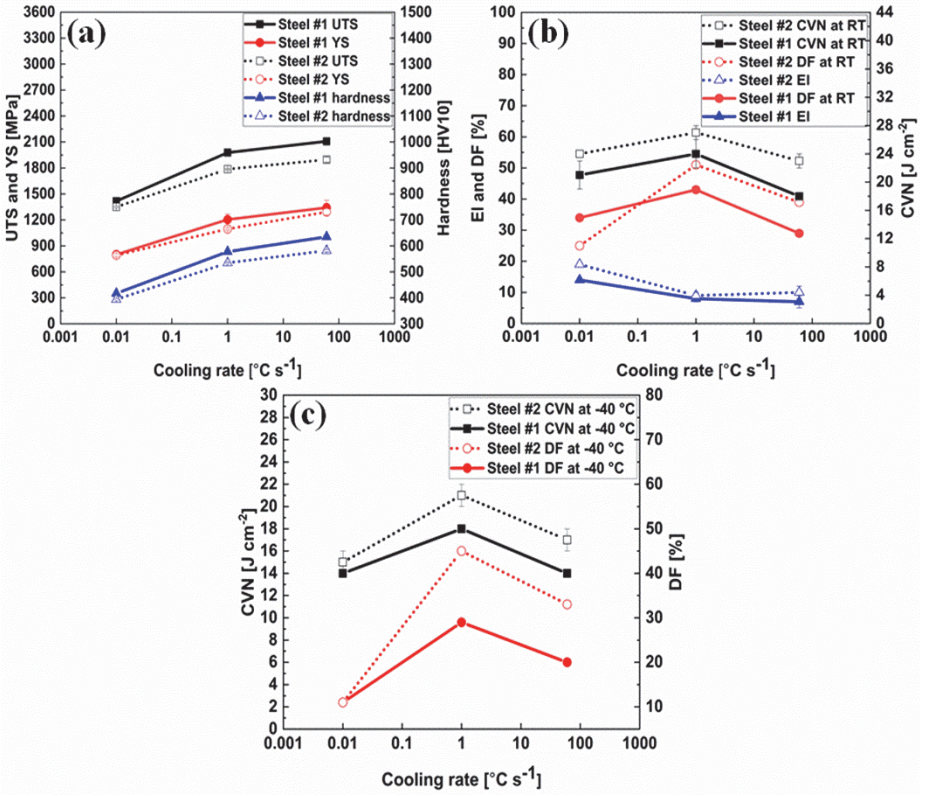

Fig. 82. Variation of mechanical properties with cooling rate (Reprinted [adapted] under CC BY license from Paper VI © 2019 Authors).

This behavior is attributed to several interrelated parameters, such as refinement of PAGS and the martensitic lath size, as well as increasing the carbon content and other alloying elements in the solid solution in the martensite. These results are in line with the results reported by Kennett and Findley [187] that the strength of micro-alloyed ASTM A514 steel in the as-quenched and low temperature tempered state is enhanced with the refinement of the PAGS. Lan et al. [188] also reported that refinement of the PAGS, packets and blocks of low carbon bainitic steel led to improving the UTS and YS. In addition to the above parameters, the presence of granular bainite with proeutectoid carbides at PAG boundaries leads to a decrease in the strength and hardness values. Also, it leads to reducing the toughness. Higher CR improves the strength but, due to the presence of hard martensite, it leads to a decrease in the elongation to fracture.

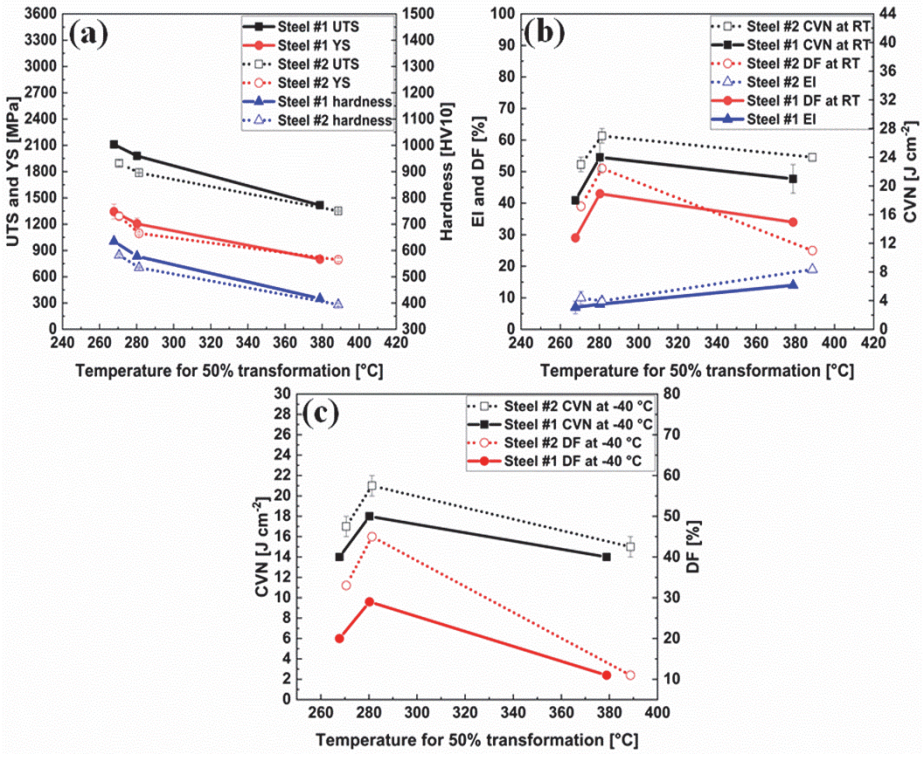

Fig. 83. Effect of 50% transformation temperature on mechanical properties (Reprinted [adapted] under CC BY license from Paper VI © 2019 Authors).

Increasing the CR from 0.01 to 1 °C/s led to an increase in the toughness properties, including impact toughness at RT and −40 °C and ductile fracture (DF) percentage, but those decreased with a further increase in the CR to 60 °C/s. A similar trend was reported by Kumar et al. [139]. The very high strength values and lower volume fraction of RA at the highest CR (60 °C/s) compared with the other CRs may be the main reasons for the reduction of the toughness properties at this CR [189]. Although the lowest CR (0.01°C/s) gives the lowest values of strength and highest volume fraction of RA, it shows the lowest toughness compared to the other CRs. This may be as a result of the large $D90\%_{GA}$, associated with the large PAGS, the presence of carbides at the grain boundaries and the presence of granular bainite, which is characterized by its low resistance to crack propagation as a result of its large crystallographic packet size and crack nucleation sites with coarse martensite-austenite (M-A) constituents [160], [190]. These results are in line with the results

obtained by Luo et al. [163], who investigate the influence of various CRs using water, oil, rapid air and sand cooling on the microstructure and toughness properties of NiCrMoV low-carbon steels. They suggested that decreasing the toughness at the slowest CR is attributed to the occurrence of granular bainite.

The higher strength and lower toughness of steel #1 in comparison with steel #2 are probably due to the higher C and Cr content and the lower Ni content, which led to the microstructural differences discussed above. The larger effective grain size of steel #1, often associated with a lower strength, has presumably been countered by higher contributions from a greater TRIP effect resulting from the high content of RA, and solid solution and precipitation strengthening.

Fig. 84 and Fig. 85 show the relationship between the yield strength and impact toughness at RT and −40 °C. It can be seen from the figures that for the martensitic microstructures, there is an inverse relationship between yield or tensile strength and CVN impact toughness. The trend line for the martensitic microstructures does not extend to the bainitic microstructures with proeutectoid carbides obtained at the slowest CR, however. In that case, impact toughness is poorer, despite much lower yield and tensile strengths. So, the formation of bainite with the proeutectoid carbides should be avoided to get better strength-toughness combinations.

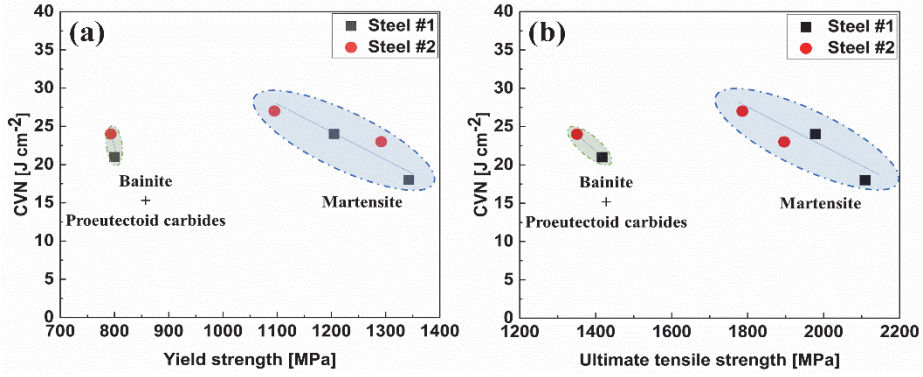

Fig. 84. Relationship between yield strength, ultimate tensile strength and impact toughness at room temperature (Reprinted [adapted] under CC BY license from Paper VI © 2019 Authors).

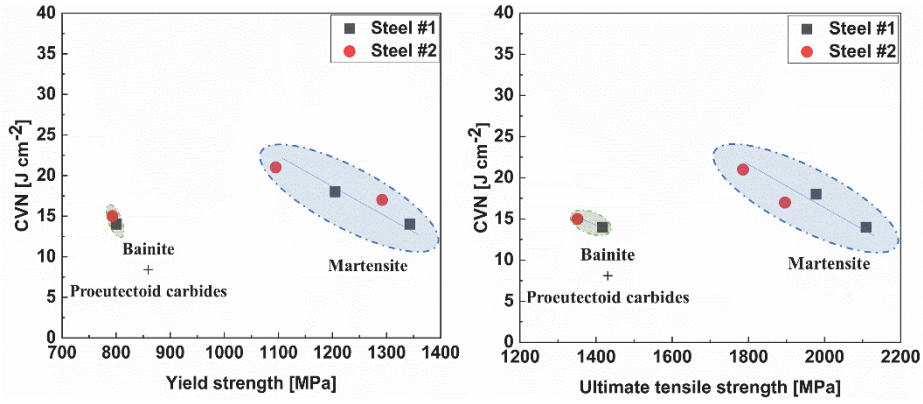

Fig. 85. Relationship between yield strength, ultimate tensile strength and impact toughness at −40 °C (Reprinted [adapted] under CC BY license from Paper VI © 2019 Authors).

4.5.3 Effect of double austenitization and quenching on mechanical properties after tempering

The mechanical properties of steels #1 and #4 after both SAQT and DAQT treatment are given in Table 28 and shown in Fig. 86.

In the case of steel #1, DAQT processing led to a decrease in UTS, YS and hardness slightly, while it led to enhancing the CVN impact toughness at room temperature and −40 °C, as can be seen from Table 28 and Fig. 86. Such findings are in a good agreement with the results obtained by Rao and Thomas [24], who studied the effect of SAQT and DAQT processing on low alloy steel containing (0.25 wt.% C, 4.0 wt.% Cr and 1.93 wt.% Mn) and reported that DAQT processing led to enhancing the toughness by 13 J, with slight loss of about 75 MPa in the YS. Also, as a result of DAQT, the ductile fracture at RT and –40 °C increased slightly, while the elongation to fracture has no significant variation. The marginal reduction in the hardness, UTS and YS are attributed to various interrelated parameters. The carbide dissolution as a result DAQT treatment (discussed in section 4.4.4) leads to an increase in the alloy concentration in solid solution, which enhances the hardenability and solid solution strengthening. Contrarily, the dissolution of carbides increases the content of carbon in the matrix, which increases the stability of RA and increased its content in the final microstructure, leading to lower hardness value [173]. However, it is well known that higher RA volume fraction leads to an increase in the UTS through TRIP effect. Increasing the lath and

effective grain sizes is considered one of the main reasons for the decrement in the hardness and the strength properties. In addition, increasing the PAGS can cause a reduction in the yield strength [191]. The enhancement in the CVN impact toughness and ductile fracture, which was observed as a result of DAQT treatment, may be attributed to several interrelated parameters, including: i) the increase in the RA volume fraction [171], [172], [192] as the presence of retained austenite films between the laths can arrest or deflect cleavage cracks [193], ii) the slight reduction in the strength properties, and iii) the refinement of the precipitates [21], [23], [192], [194], as it is well known that the impact toughness is decreased by the presence of large undissolved carbides, which can act as nuclei for microvoids [195].

In the case of steel #4, as a result of DAQT treatment, the CVN impact toughness and percentage of ductile fracture were improved without any reduction in the hardness, UTS or YS. Similar parameters discussed for steel #1 are also working in the case of steel #4. However, the limited increase in the PAGS, effective grain and lath sizes are the main reason for retaining the same level of hardness, UTS or YS in combination with an improved level of the CVN impact toughness and percentage ductile fracture.

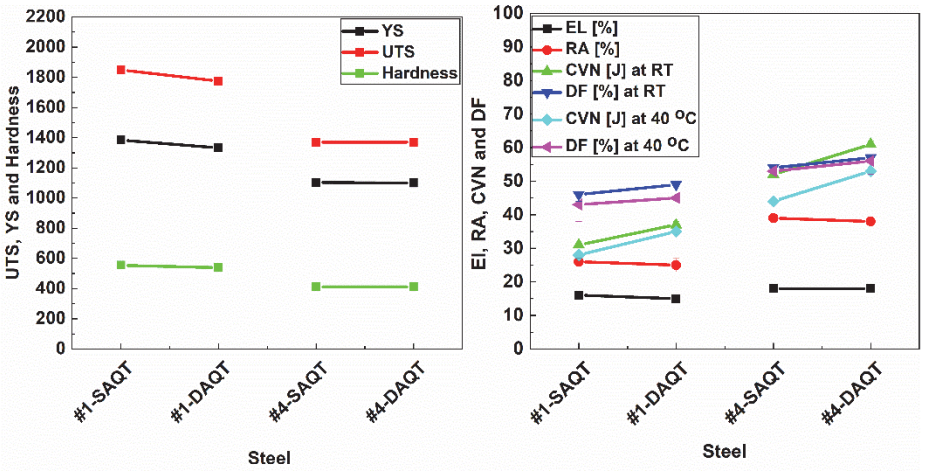

Fig. 86. Effect of single and double austenitization, quenching and tempering on the mechanical properties of steel #1 and steel #4 (Under CC BY-NC-ND license from Paper VII © 2019 Authors).

Table 28. Tensile properties, Charpy-V notch impact toughness and hardness of steels #1 and #4 after single and double austenitization, quenching and tempering (Under CC BY-NC-ND license from Paper VII © 2019 Authors).

Steel	Tensile properties				Charpy V test at room temperature		Charpy V test at −40°C		Hardness [3]
	UTS [1]	YS [1]	El. [1]	Reduction area [1]	Absorbed energy [1]	Ductile fracture [2]	Absorbed energy [1]	Ductile fracture [2]	[HV10]
	[MPa]	[MPa]	[%]	[%]	[J]	[%]	[J]	[%]	
Steel #1-SAQT	1849 ± 8	1383 ± 8	16 ± 0	26 ± 1	31 ± 0	46 ± 2	28 ± 0	43 ± 5	555 ± 2
Steel #1-DAQT	1775 ± 3	1333 ± 13	15 ± 0	25 ± 2	37 ± 1	49 ± 1	35 ± 1	45 ± 0	538 ± 2
Steel #4-SAQT	1370 ± 4	1103 ± 28	18 ± 0	39 ± 0	52 ± 1	54 ± 1	44 ± 0	53 ± 6	413 ± 2
Steel #4-DAQT	1370 ± 3	1100 ± 4	18 ± 0	38 ± 1	61 ± 1	57 ± 2	53 ± 0	56 ± 4	412 ± 2

[1] Error bars are standard deviations of three measurements.

[2] Ductile fracture % was calculated according to ASTM A 370-11.

[3] Error bars are standard deviations of ten measurement.

5 Summary and conclusions

The most important conclusions that can be drawn from this thesis are presented in this section in three subheadings: i) influence of ESR on the yield of alloying elements, cleanliness, microstructure and mechanical properties of the investigated CrNiMoWMnV ultrahigh-strength steels, ii) effect of CR and composition on microstructure and mechanical properties of ultrahigh-strength steels, and iii) the influence of single and double austenitization and quenching on the microstructure and mechanical properties of the investigated CrNiMoWMnV ultrahigh-strength steels after tempering at 200 °C.

5.1 Influence of electroslag remelting on the yield of alloying elements, cleanliness, microstructure and mechanical properties of the investigated CrNiMoWMnV ultrahigh-strength steels

Overall, ESR of the investigated UHSSs using synthetic fused slag consisting of 70% CaF_2, 15% Al_2O_3 and 15% CaO gave a high yield of the alloying elements, i.e. Cr, Ni, Mo, W, Mn and V, while it provided a low yield of Si. In addition to the dependency of the yield of alloying elements on the slag composition and the ESR operating parameters, it depends on the starting chemical composition of the consumable electrode, or rather the activities of the alloying elements which are determined by the interaction coefficients between the alloying elements and the other elements in the molten state. The yield of Cr, W, V, Mn and Ni in the remelted ingot decreased by increasing their activity in the molten state. In some cases, the yield of Mo was increased, and this is attributed to the extremely lower interaction coefficient between Mo and O and its less negative free energy of oxidation, combined with the effect of losses in the impurities S, P and N and the other alloying elements like Cr, Mn, Si and V. The yield of Ni is high in all investigated UHSSs, which is attributed to the low interaction coefficient between Ni and O. The yield of Mn is relatively high despite the strong negative interaction between Mn with O and S, and this can be explained by the high activity of MnO in the molten slag. The yield of Si is small because of its high negative free oxidation energy. Moreover, once the Si in the consumable electrode oxidized to form SiO_2 in the slag, SiO_2 reacted with the CaO in the slag to form a stable calcium silicate which lowers the activity of SiO_2, which further reduces the concentration of Si in the final ingots.

Increasing the S activity in the molten steel pool improves the degree of desulphurization. About 97–99% of S is removed from the steel as gas by metal-gas and slag-gas interactions. Dephosphorization was only 5% for all investigated UHSSs. Denitrification can be performed using ESR with 70-15-15 CaF_2-CaO-Al_2O_3 synthetic slag, and it ranges from 8–63% depending on the steel composition.

ESR improves the cleanliness of investigated UHSSs through reducing the total impurity level (O%+S%+N%) and the content of NMIs by as much as 46% and 62% respectively. In all the ESR treated steels, about 94% of the total inclusion counts were smaller than 6 μm, compared to about 90% in the case of steels without ESR. Four main classes of NMIs, including oxides, sulphides, nitrides and complex multiphase inclusions, were observed in the investigated steels without and with ESR. ESR results in significant changes in the area percentages, number densities, maximum equivalent circle diameters, and chemical composition of the various NMIs. ESR lead to removing most of MnS inclusions, while it caused formation of new NMIs like $MnS.Al_2O_3$ and TiN.MnS, which were formed by reprecipitation of MnS on oxide or nitride inclusions. Such NMIs are relatively low in number density, area percentage and maximum ECDs. Some sulphides were modified by Ca to (CaMn)S and $CaS.Al_2O_3$. Some nitrides, such as TiN and (TiV)N, were nucleated and precipitated during the solidification phase. Fine Al_2O_3 particles were formed in the investigated steels due to the Al addition as deoxidant to the molten slag during the ESR to protect the molten metal pool from the atmospheric oxygen. Most of the NMIs particles up to 98% in the remelted ingots have ECD less than 6 μm. The Al content increased in the remelted ingots due to the addition of Al as deoxidant during ESR. There is a good agreement between the thermodynamic calculations and the experimental results, as the expected mass fraction of MnS inclusions, which represent the main NMIs, decreases as a result of ESR. The predicted complex NMIs like $MnO.Al_2O_3.SiO_2$ and the molten inclusions in addition to silicon oxides are predicted to be removed completely as a result of ESR. The degree of cleanliness of the remelted ingots depends on the chemical composition and the total impurity levels in the consumable electrode.

General conclusions cannot be made regarding the effect of ESR on the NMI characteristics, microstructure and mechanical properties. The influence of ESR depends mainly on the impurity level, the starting chemical composition and the change in chemical composition during ESR, together with the composition of the slag and the details of the subsequent thermomechanical treatment. ESR leads to refining the PAGS, and it has no effect on the degree of micro-segregation. In the case of fully martensitic steels, ESR leads to an increment in the UTS, YS and

hardness. However, elongation to fracture, CVN impact toughness, and percentage ductile fracture varies with the steel chemistry. The improvement in the UTS, YS and hardness are attributed to several interrelated parameters, including: the refinement of the PAGS, the effective high-angle grain size and the lath size; an increase in the number of fine precipitates; and an increase in RA. In the case of steel with a mixed martensitic-bainitic microstructure, ESR led to an increase in the volume fraction of bainite as a result of the slight variation in the chemical composition brought about by ESR. This led to improving CVN impact toughness, elongation to fracture, and the ductile fracture percentage.

5.2 Effect of cooling rate and composition on the microstructure and mechanical properties of ultrahigh-strength steels

Two UHSSs with different contents of C, Cr and Ni were studied with regard to their phase transformations, microstructures and mechanical properties in the as-cooled, untempered condition for CRs ranging from 60 to 0.01 °C/s.

The steel with a high C and Cr content provided a fully martensitic microstructure for a wide range of CRs ranging from 60 °C/s to 0.08 °C/s. But decreasing the CR led to a decrease in the hardness of the martensite. Depending on the steel compositions, bainite-martensite mixtures are formed down to CRs of 0.02 °C/s or 0.08 °C/s. At a CR of 0.01 °C/s, granular bainite represents the main microstructure constituent with proeutectoid carbides precipitated at the PAG boundaries. There is a significant amount of retained austenite obtained within the bainitic microstructure compared to that obtained within the martensitic microstructure. This is because of the presence of Si (0.6 wt.%), Ni (2-3 wt.%) and the very slow CR for bainitic microstructure. The PAGS and $D90\%_{GA}$ decreased as the CR increased as a result of decreasing the time required for the grain growth.

The values of UTS, YS, YS/UTS ratio and hardness increased with increasing the CR, as a result of the refinement of the microstructural features, e.g. martensitic lath size and EGS. However, the highest (60 °C/s) and lowest (0.01 °C/s) CR is associated with a low level of toughness; the first case is due to an extremely high strength level and the low level of retained austenite, while the second case is due to microstructure coarsening, i.e. large PAGS and $D90\%_{GA}$, in addition to the precipitation of carbides at PAG boundaries and the presence of granular bainite.

At the slowest CR studied, the steel with low content of C and Cr but high in Ni content contained a low volume fraction of the proeutectoid carbides at PAG boundaries.

In order to get a good combination between strength and toughness properties, the microstructure should be mainly martensitic, while the formation of granular bainite and proeutectoid carbides at PAG boundaries should be completely avoided.

5.3 The effect of double austenitization and quenching on the microstructure and mechanical properties of CrNiMoWMnV ultrahigh-strength steels after low-temperature tempering

With the aim of improving the combination of strength and toughness, two heat treatments were applied on two UHSSs with 0.32 and 0.18 wt.% C and tensile strengths in the range of 1370–1850 MPa, and then the microstructure and the mechanical properties were evaluated. The heat treatments are i) single austenitization at 930 °C followed by quenching and tempering at 200 °C (SAQT), and ii) austenitization at 1100 °C and quenching followed by a second austenitization at 930 °C, quenching and tempering at 200 °C, i.e. double austenitization and quenching followed by tempering (DAQT).

The final microstructures of the examined UHSSs after all treatment comprised tempered martensite with small fractions of retained austenite and precipitates. Four types of precipitates were observed in the investigated UHSSs: i) tungsten rich complex carbides M_xC_y, ii) aluminium nitride AlN, iii) titanium vanadium carbonitride (TiV)(CN), and iv) complex AlN with a core of (TiV)(CN).

The volume fraction of retained austenite was increased in the examined UHSSs after DAQT treatment, compared to SAQT treatment. This can be attributed to the dissolution of the precipitates that occurs during the first high-temperature austenitization, thus increasing the alloying element in the matrix, which lowers the transformation temperature and thereby provides uncomplete transformation.

DAQT treatment led to an increase in the PAGS and the effective martensite grain size at 90% of cumulative grain area distribution in the examined UHSSs, but the effect was much higher in the 0.32C steel. This was because of the reduced grain boundary pinning effect as a result of the greater dissolution of precipitates in the first high-temperature austenitization. Also, in the case of 0.32C steel, there is a lower contribution from AlN to grain boundary pinning due to its lower N content. However, there is a slight increase in the effective martensite grain and lath sizes due to the compensating effect of precipitate dissolution on M_s and M_f temperatures, as reducing the transformation temperatures due to the dissolutions of carbides led to refining the effective grain and lath sizes. DAQT treatment led to

refining the mean size and $D90\%_{ppt}$ size of the precipitates in the case of 0.18C steel. However, it led to refining $D90\%_{ppt}$ only in the 0.32C steel.

For the investigated UHSS steels, DAQT improves the CVN impact toughness. In the case of the 0.32C steel, this occurs at the cost of a small reduction in hardness, UTS and YS, but in the case of the 0.18C steel, there is no deterioration in hardness or tensile properties (UTS, YS and El.%). The improvement in the CVN impact toughness can be attributed to the increase in retained austenite and refinement of the precipitates.

6 Novel features

It is believed that the following findings and observations are original to this thesis:

- In ESR, the yield of alloying elements not only depends on the slag composition and ESR parameters, but also on the starting chemical composition of the consumable electrode, or rather, the activities of the alloying elements as determined by the interaction coefficients between the elements.
- Thermodynamic calculations and ESR showed dissolution of all NMIs in the consumable electrode, formation of new NMIs and modifications of others in the produced ingot.
- The refinement of the precipitates and the increase in their number density and volume fraction caused by ESR together with the high cooling rate in ESR led to a refinement the final microstructural features, such as prior austenite grain size, effective martensite grain size and lath size.
- In the case of fully martensitic steels studied, ESR leads to an increase in the UTS, YS and hardness. However, the effect of ESR on elongation to fracture, CVN impact toughness, and percentage ductile fracture varies with the steel chemistry.
- For the steel with a mixed martensitic-bainitic microstructure, the changes in chemical composition brought about by ESR led to an increase in the volume fraction of bainite, which lowered the UTS and YS, but enhanced the elongation to fracture, the CVN impact toughness, and the percentage ductile fracture.
- The best combination of strength and CVN impact toughness is achieved by choosing CRs that achieve a fully martensitic microstructure without the formation of granular bainite and proeutectoid grain boundary carbides.
- The effect of SAQT and DAQT processes on the microstructure and mechanical properties depends on the starting chemical composition. DAQT improves the CVN impact toughness. In the case of the 0.32C steel, this occurs at the cost of a small reduction in hardness, UTS and YS, but in the case of the 0.18C steel, there is no deterioration in hardness or tensile properties (UTS, YS and El.%). The improvement in the CVN impact toughness can be attributed to the increase in retained austenite and refinement of the precipitates.

7 Recommendation for further research

The present work shows the possibility to produce UHSS with high impact toughness using the following process route: low-cost air induction melting, ESR, and temperature-controlled forging and cooling followed by reheating, quenching and tempering at 200 °C. Extensive studies are given on each stage of the production route and even though the results are quiet promising, the following topics could be studied in the future:

- In the current study, in ESR, only one synthetic slag composition has been used. So, it is possible to study the effect of various slag compositions to get the best cleanliness in terms of total impurity level and the content of NMIs in the produced steel.
- In Paper V, the reason for the observed increase in the PAGS after a total strain of 0.8 with a finish forging temperature of 950 °C requires further investigation.
- Study the effect of CR on the dislocation density and find the relationship between the variation in the PAGS and the dislocation density.
- The heat treatment of these steels is not well established. Only two heat treatments (SAQT and DAQT) have been studied in the current work. In order to get a good combination of strength and toughness, the effect of various heat treatments on the final microstructure and mechanical properties can be studied. The volume fraction of the retained austenite plays an important role in the current investigated steels. So, some heat treatments can be studied with the aim of increasing the retained austenite volume fraction, for example: i) quenching and partitioning, and ii) quenching and partitioning and tempering.
- The fine precipitates play an important role in the current investigated steel. So, the variation in the tempering temperature and time can be studied with the aim of increasing the volume fraction of the fine precipitates and studying their effect on the final microstructure and mechanical properties.
- Further investigations are needed to know the wear resistance, weldability, corrosion resistance and fatigue properties of the proposed steel, along with the high temperature strength properties.

List of references

[1] "World steel in figures 2019," World Steel Association, 2019. [Online]. Available: https://www.worldsteel.org/.

[2] H. Suopajärvi, "Bioreducer use in blast furnace ironmaking in Finland," Ph.D. dissertation, University of Oulu, Oulu, Finland, 2014.

[3] "Steel's contribution to a low carbon future and climate resilient societies," World Steel Association, 2017. [Online]. Available: https://www.worldsteel.org/.

[4] M. Wörtler *et al.*, "Steel's contribution to a low-carbon Europe 2050," The Boston Consulting Group, 2013.

[5] M. Dilmore and J. D. Ruhlman, "Eglin steel—a low alloy high strength composition," US7537727B2, May 26, 2009.

[6] A. K. Vaish, G. V. R. Iyer, P. K. De, B. A. Lakra, A. K. Chakrabarti, and P. Ramachandrarao, "Electroslag remelting-its status, mechanism and refining aspects in the production of quality steels," *J. Metall. Mater. Sci.*, vol. 42, no. 1, pp. 11–29, 2000.

[7] W. E. Duckworth and G. Hoyle, *Electro-slag refining*. Chapman & Hall, 1969.

[8] U. Biebricher and H. Scholz, "Electro slag remelting technologies in the past and in the future," *Metall. Plant Technol. Int.*, vol. 22, no. 3, pp. 36–38, 1998.

[9] H. Halfa, M. Eissa, and A. Fathy, "Electroslag remelted ultra- high strength high ductility martensitic," in *Proceedings of the Conference Metal*, Brno, Czech Republic, EU, 2013, p. 7.

[10] A. Pribulová, P. Futáš, A. Kmita, D. Márasová, and M. Holtzer, "Impact of electro slag remelting on 14 109 steel properties," *Arch. Metall. Mater.*, vol. 62, no. 1, pp. 181–185, Mar. 2017, doi: 10.1515/amm-2017-0025.

[11] S. K. Maity, N. B. Ballal, G. Goldhahn, and R. Kawalla, "Development of low alloy titanium and niobium microalloyed ultrahigh strength steel through electroslag refining," *Ironmak. Steelmak.*, vol. 35, no. 5, pp. 379–386, Jul. 2008, doi: 10.1179/174328107X203895.

[12] S. K. Maity, N. B. Ballal, G. Goldhahn, and R. Kawalla, "Development of ultrahigh strength low alloy steel through electroslag refining process," *ISIJ Int.*, vol. 49, no. 6, pp. 902–910, 2009, doi: 10.2355/isijinternational.49.902.

[13] C. Zhang *et al.*, "Effect of microstructure on the strength of 25CrMo48V martensitic steel tempered at different temperature and time," *Mater. Des. 1980-2015*, vol. 36, pp. 220–226, Apr. 2012, doi: 10.1016/j.matdes.2011.11.026.

[14] S. Morito, H. Yoshida, T. Maki, and X. Huang, "Effect of block size on the strength of lath martensite in low carbon steels," *Mater. Sci. Eng. A*, vol. 438–440, pp. 237–240, Nov. 2006, doi: 10.1016/j.msea.2005.12.048.

[15] Y. Liu, D. Ye, Q. Yong, J. Su, K. Zhao, and W. Jiang, "Effect of heat treatment on microstructure and property of Cr13 super martensitic stainless steel," *J. Iron Steel Res. Int.*, vol. 18, no. 11, pp. 60–66, Nov. 2011, doi: 10.1016/S1006-706X(11)60118-0.

[16] C. Zhang *et al.*, "Effect of martensitic morphology on mechanical properties of an as-quenched and tempered 25CrMo48V steel," *Mater. Sci. Eng. A*, vol. 534, pp. 339–346, Feb. 2012, doi: 10.1016/j.msea.2011.11.078.

[17] A. J. Kaijalainen, P. P. Suikkanen, T. J. Limnell, L. P. Karjalainen, J. I. Kömi, and D. A. Porter, "Effect of austenite grain structure on the strength and toughness of direct-quenched martensite," *J. Alloys Compd.*, vol. 577, pp. S642–S648, Nov. 2013, doi: 10.1016/j.jallcom.2012.03.030.

[18] S. C. Kennett and K. O. Findley, "Strengthening and toughening mechanisms in martensitic steel," in *Advanced Materials Research*, 2014, vol. 922, pp. 350–355.

[19] Q. Wang, C. Zhang, R. Li, J. Gao, M. Wang, and F. Zhang, "Characterization of the microstructures and mechanical properties of 25CrMo48V martensitic steel tempered at different times," *Mater. Sci. Eng. A*, vol. 559, pp. 130–134, Jan. 2013, doi: 10.1016/j.msea.2012.08.049.

[20] A. N. Isfahany, H. Saghafian, and G. Borhani, "The effect of heat treatment on mechanical properties and corrosion behavior of AISI420 martensitic stainless steel," *J. Alloys Compd.*, vol. 509, no. 9, pp. 3931–3936, Mar. 2011, doi: 10.1016/j.jallcom.2010.12.174.

[21] X. Xiong, F. Yang, X. Zou, and J. Suo, "Effect of twice quenching and tempering on the mechanical properties and microstructures of SCRAM steel for fusion application," *J. Nucl. Mater.*, vol. 430, no. 1–3, pp. 114–118, Nov. 2012, doi: 10.1016/j.jnucmat.2012.06.047.

[22] M. H. Khani Sanij, S. S. Ghasemi Banadkouki, A. R. Mashreghi, and M. Moshrefifar, "The effect of single and double quenching and tempering heat treatments on the microstructure and mechanical properties of AISI 4140 steel," *Mater. Des.*, vol. 42, pp. 339–346, Dec. 2012, doi: 10.1016/j.matdes.2012.06.017.

[23] J. Liu, H. Yu, T. Zhou, C. Song, and K. Zhang, "Effect of double quenching and tempering heat treatment on the microstructure and mechanical properties of a novel 5Cr steel processed by electro-slag casting," *Mater. Sci. Eng. A*, vol. 619, pp. 212–220, Dec. 2014, doi: 10.1016/j.msea.2014.09.063.

[24] B. V. N. Rao and G. Thomas, "Structure-property relations and the design of Fe-4Cr-C base structural steels for high strength and toughness," *Metall. Trans. A*, vol. 11, no. 3, pp. 441–457, Mar. 1980, doi: 10.1007/BF02654568.

[25] M. Sarikaya, B. G. Steinberg, and G. Thomas, "Optimization of Fe/Cr/C base structural Steels for improved strength and toughness," *Metall. Trans. A*, vol. 13, no. 12, pp. 2227–2237, Dec. 1982, doi: 10.1007/BF02648394.

[26] E. Chang, C. Y. Chang, and C. D. Liu, “The effects of double austenitization on the mechanical properties of a 0.34C containing low-alloy Ni-Cr-Mo-V steel,” *Metall. Mater. Trans. A*, vol. 25, no. 3, pp. 545–555, Mar. 1994, doi: 10.1007/BF02651596.

[27] M. Yellishetty, G. M. Mudd, P. G. Ranjith, and A. Tharumarajah, “Environmental life-cycle comparisons of steel production and recycling: sustainability issues, problems and prospects,” *Environ. Sci. Policy*, vol. 14, no. 6, pp. 650–663, Oct. 2011, doi: 10.1016/j.envsci.2011.04.008.

[28] H.-J. Odenthal, J. Alken, A. Kemminger, F. Krause, N. Vogl, and S. Rühl, “Applied numerical simulation for safe and efficient process conditions of metallurgical plants,” presented at the 8th European Oxygen Steelmaking Conference (EOSC), Taranto (I), Oct. 2018.

[29] E. Mousa, “Modern blast furnace ironmaking technology: potentials to meet the demand of high hot metal production and lower energy consumption,” *Metall. Mater. Eng.*, vol. 25, no. 2, pp. 69–104, Jul. 2019, doi: 10.30544/414.

[30] “Fact sheet: climate change mitigation,” World steel association, 2019. [Online]. Available: https://www.worldsteel.org/.

[31] P. Cavaliere, *Ironmaking and steelmaking processes: greenhouse emissions, control, and reduction*, 1st ed. Springer International Publishing, 2016.

[32] “European steel in figures 2019,” The European Steel Association (EUROFER), 2019. [Online]. Available: https://www.eurofer.eu/.

[33] “The future of steel scrap,” BDSV, 2016. [Online]. Available: https://www.bdsv.org/.

[34] T. V. Philip and T. J. McCaffrey, “Ultrahigh-strength steels,” in *Properties and Selection: Irons, Steels, and High-Performance Alloys*, ASM International, 1990, pp. 430–448.

[35] J. Kömi, P. Karjalainen, and D. Porter, “Direct-Quenched Structural Steels,” in *Encyclopedia of Iron, Steel, and Their Alloys*, CRC Press, 2016.

[36] G. Malakondaiah, M. Srinivas, and P. R. Rao, “Ultrahigh-strength low-alloy steels with enhanced fracture toughness,” *Prog. Mater. Sci.*, vol. 42, no. 1–4, pp. 209–242, Jan. 1997, doi: 10.1016/S0079-6425(97)00016-9.

[37] P. Kylee, “Modeling the effects of heat treatment on micro-segregation in Ultrahigh-strength cast steel,” Baccalaureate Thesis, The Pennsylvania State University, Pennsylvania, USA, 2010.

[38] P. C. Lynch, “The development of ultrahigh strength low alloy cast steels with increased toughness,” Ph.D. dissertation, The Pennsylvania State University, Pennsylvania, USA, 2011.

[39] F. C. Campbell, *Manufacturing technology for aerospace structural materials*, 1st ed. Amsterdam ; Boston: Elsevier, 2006.

[40] K. Sato, “Improving the toughness of ultrahigh strength steel,” Ph.D. dissertation, University of California, Berkely, California, USA, 2002.

[41] W. M. Garrison, “Ultrahigh-strength steels for aerospace applications,” *JOM*, vol. 42, no. 5, pp. 20–24, May 1990, doi: 10.1007/BF03220942.

[42] G. Krauss, “Heat treated martensitic steels: microstructural systems for advanced manufacture.,” *ISIJ Int.*, vol. 35, no. 4, pp. 349–359, 1995, doi: 10.2355/isijinternational.35.349.
[43] M. Srinivas and A. V. Reddy, “Aero steels: part 2—high alloy steels,” in *Aerospace Materials and Material Technologies*, N. E. Prasad and R. J. H. Wanhill, Eds. Singapore: Springer Singapore, 2017, pp. 173–198.
[44] S. K. and R. Kawall, “Ultrahigh strength steel: development of mechanical properties through controlled cooling,” in *Heat Transfer - Engineering Applications*, V. Vikhrenko, Ed. InTech, 2011.
[45] E. Pereloma and D. V. Edmonds, Eds., *Phase transformations in steels*. Oxford; Philadelphia: Woodhead Publishing, 2012.
[46] W. Sha, *Steels from materials science to structural engineering*. London: Springer London, 2013.
[47] H. Bhadeshia and R. Honeycombe, *Steels: microstructure and properties*. Jordan Hill: Elsevier Science, 2006.
[48] H. Bhadeshia and R. Honeycombe, “Tempering of martensite,” in *Steels: Microstructure and Properties*, Elsevier, 2017, pp. 237–270.
[49] T. O. Webb, D. C. Van Aken, and S. N. Lekakh, “Evaluating chemical homogeneity in the performance of Eglin steel,” in *AFS Proceedings*, schaumburg, USA, 2014, pp. 1–16.
[50] V. Tungala, A. Arora, B. Gwalani, R. S. Mishra, R. E. Brennan, and K. C. Cho, “Microstructure and mechanical properties of friction stir processed cast Eglin steel (ES-1),” *Mater. Sci. Eng. A*, vol. 709, pp. 105–114, Jan. 2018, doi: 10.1016/j.msea.2017.10.033.
[51] B. M. Leister and J. N. DuPont, “Development of a continuous cooling transformation diagram for Eglin steel,” *Mater. Sci. Technol.*, vol. 31, no. 12, pp. 1425–1432, Sep. 2015, doi: 10.1179/1743284714Y.0000000720.
[52] B. M. Leister, J. N. DuPont, M. Watanabe, and R. A. Abrahams, “Mechanical properties and microstructural evolution of simulated heat-affected zones in wrought eglin steel,” *Metall. Mater. Trans. A*, vol. 46, no. 12, pp. 5727–5746, Dec. 2015, doi: 10.1007/s11661-015-3131-x.
[53] G. E. Totten, Ed., *Steel heat treatment: metallurgy and technologies*, 2nd ed. Boca Raton, FL: Taylor & Francis, 2007.
[54] P. Suikkanen, “Development and processing of low carbon bainitic steels,” Ph.D. dissertation, University of Oulu, Oulu, Finland, 2009.
[55] H. H. Kolla *et al.*, “Development of an ultrahigh strength low alloy steel for armour applications,” *Mater. Sci. Technol.*, vol. 27, no. 2, pp. 551–555, Feb. 2011, doi: 10.1179/026708309X12560332736476.
[56] S. Piva, “Non-metallic inclusion changes in Si-Mn killed steels,” Ph.D. dissertation, Carnegie Mellon University, Pittsburgh, Pennsylvania, United States, 2018.

[57] R. Bridget Punch, “Toughness enhancement of high strength low alloy strip steels,” Ph.D. dissertation, University of Birmingham, Birmingham, England, 2013.
[58] F. G. Wilson and T. Gladman, “Aluminium nitride in steel,” *Int. Mater. Rev.*, vol. 33, no. 1, pp. 221–286, Jan. 1988, doi: 10.1179/imr.1988.33.1.221.
[59] A. Tuling and B. Mintz, “Crystallographic and morphological aspects of AlN precipitation in high Al, TRIP steels,” *Mater. Sci. Technol.*, vol. 32, no. 6, pp. 568–575, Apr. 2016, doi: 10.1179/1743284715Y.0000000126.
[60] T. Gladman, *The physical metallurgy of microalloyed steels*. London: Maney, 1997.
[61] Y. Kang, H. Yu, J. Fu, K. Wang, and Z. Wang, “Morphology and precipitation kinetics of AlN in hot strip of low carbon steel produced by compact strip production,” *Mater. Sci. Eng. A*, vol. 351, no. 1–2, pp. 265–271, Jun. 2003, doi: 10.1016/S0921-5093(02)00845-6.
[62] G. N. Haidemenopoulos, *Physical metallurgy: principles and design*. Boca Raton: Taylor & Francis, a CRC title, part of the Taylor & Francis imprint, a member of the Taylor & Francis Group, the academic division of T&F Informa, plc, 2018.
[63] S. Choi, “Optimization of microstructure and properties of high strength spring steel,” Ph.D. dissertation, Delft University of Technology, Delft, Netherlands, 2011.
[64] G. Krauss, “Martensite in steel: strength and structure,” *Mater. Sci. Eng. A*, vol. 273–275, pp. 40–57, Dec. 1999, doi: 10.1016/S0921-5093(99)00288-9.
[65] S. Morito, H. Tanaka, R. Konishi, T. Furuhara, Maki, and T, “The morphology and crystallography of lath martensite in Fe-C alloys,” *Acta Mater.*, vol. 51, no. 6, pp. 1789–1799, 2003.
[66] H. Kitahara, R. Ueji, N. Tsuji, and Y. Minamino, “Crystallographic features of lath martensite in low-carbon steel,” *Acta Mater.*, vol. 54, no. 5, pp. 1279–1288, 2006.
[67] S. C. Kennett, “Strengthening and toughening mechanisms in low-C microalloyed martensitic steel as influenced by austenite conditioning,” Thesis, Colorado School of Mines. Arthur Lakes Library, 2007.
[68] L. Morsdorf, O. Jeannin, D. Barbier, M. Mitsuhara, D. Raabe, and C. C. Tasan, “Multiple mechanisms of lath martensite plasticity,” *Acta Mater.*, vol. 121, pp. 202–214, Dec. 2016, doi: 10.1016/j.actamat.2016.09.006.
[69] S. Morito, J. Nishikawa, and T. Maki, “Dislocation density within lath martensite in Fe-C and Fe-Ni alloys,” *ISIJ Int.*, vol. 43, no. 9, pp. 1475–1477, 2003.
[70] N. Hansen and X. Huang, “Microstructure and flow stress of polycrystals and single crystals,” *Acta Mater.*, vol. 46, no. 5, pp. 1827–1836, Mar. 1998, doi: 10.1016/S1359-6454(97)00365-0.

[71] B. Hutchinson *et al.*, "Microstructures and hardness of as-quenched martensites (0.1–0.5%C)," *Acta Mater.*, vol. 59, no. 14, pp. 5845–5858, Aug. 2011, doi: 10.1016/j.actamat.2011.05.061.

[72] S. Takaki, K.-L. Ngo-Huynh, N. Nakada, and T. Tsuchiyama, "Strengthening mechanism in ultra low carbon martensitic steel," *ISIJ Int.*, vol. 52, no. 4, pp. 710–716, 2012, doi: 10.2355/isijinternational.52.710.

[73] T. Gladman, "Precipitation hardening in metals," *Mater. Sci. Technol.*, vol. 15, no. 1, pp. 30–36, Jan. 1999, doi: 10.1179/026708399773002782.

[74] R. E. Smallman and A. H. W. Ngan, "Precipitation hardening," in *Modern Physical Metallurgy*, Elsevier, 2014, pp. 499–527.

[75] S. Pallaspuro, "On the factors affecting the ductile-brittle transition in as-quenched fully and partially martensitic low-carbon steels," Ph.D. dissertation, University of Oulu, Oulu, Finland, 2018.

[76] G. J. Roe and B. L. Bramfitt, "Notch toughness of steels," in *Properties and Selection: Irons, Steels, and High-Performance Alloys*, ASM International, 1990, pp. 737–754.

[77] Y. Ren *et al.*, "Detection of non-metallic inclusions in steel continuous casting billets," *Metall. Mater. Trans. B*, vol. 45, no. 4, pp. 1291–1303, Aug. 2014, doi: 10.1007/s11663-014-0042-y.

[78] Z. G. Yang *et al.*, "The fatigue behaviors of zero-inclusion and commercial 42CrMo steels in the super-long fatigue life regime," *Acta Mater.*, vol. 52, no. 18, pp. 5235–5241, Oct. 2004, doi: 10.1016/j.actamat.2004.06.031.

[79] M. D. Chapetti, T. Tagawa, and T. Miyata, "Ultra-long cycle fatigue of high-strength carbon steels part I: review and analysis of the mechanism of failure," *Mater. Sci. Eng. A*, vol. 356, no. 1, pp. 227–235, Sep. 2003, doi: 10.1016/S0921-5093(03)00135-7.

[80] M. D. Chapetti, T. Tagawa, and T. Miyata, "Ultra-long cycle fatigue of high-strength carbon steels part II: estimation of fatigue limit for failure from internal inclusions," *Mater. Sci. Eng. A*, vol. 356, no. 1, pp. 236–244, Sep. 2003, doi: 10.1016/S0921-5093(03)00136-9.

[81] L. H. He and J. H. Zhao, "Evolution of stresses in composites with rigid inclusions during interface diffusion: a two-dimensional case," *Int. J. Eng. Sci.*, vol. 38, no. 11, pp. 1181–1195, Jul. 2000, doi: 10.1016/S0020-7225(99)00070-1.

[82] C. Bertrand *et al.*, "Metallurgy of plastic inclusions to improve fatigue life of engineering steels," *Ironmak. Steelmak.*, vol. 30, no. 2, pp. 165–169, Apr. 2003, doi: 10.1179/030192303225001667.

[83] P. Kaushik, J. Lehmann, and M. Nadif, "State of the art in control of inclusions, their characterization, and future requirements," *Metall. Mater. Trans. B*, vol. 43, no. 4, pp. 710–725, Aug. 2012, doi: 10.1007/s11663-012-9646-2.

[84] E. A. Chichkarev, “Modeling the coagulation and removal of nonmetallic inclusions during the injection of an inert gas into a melt,” *Metallurgist*, vol. 54, no. 3–4, pp. 236–243, Jul. 2010, doi: 10.1007/s11015-010-9286-1.

[85] D. Janke, Z. Ma, P. Valentin, and A. Heinen, “Improvement of castability and quality of continuously cast steel,” *ISIJ Int.*, vol. 40, no. 1, pp. 31–39, 2000, doi: 10.2355/isijinternational.40.31.

[86] S. Yang, Q. Wang, L. Zhang, J. Li, and K. Peaslee, “Formation and modification of MgO·Al2O3-based inclusions in alloy steels,” *Metall. Mater. Trans. B*, vol. 43, no. 4, pp. 731–750, Aug. 2012, doi: 10.1007/s11663-012-9663-1.

[87] B. Arh, B. Podgornik, and J. Burja, “Electroslag remelting: a process overview,” *Mater. Tehnol.*, vol. 50, no. 6, pp. 971–979, Dec. 2016, doi: 10.17222/mit.2016.108.

[88] “ESR - Electroslag Remelting.” INTECO special melting technologies GmbH, 2012, [Online]. Available: http://www.gotrawama.eu/siderurgia/ESR%20Mailversion_2012-10-09.pdf.

[89] R. H. Nafziger, *The electroslag melting process*. U.S. Bureau of Mines, 1974.

[90] D. Kopeliovich, “Electroslag remelting.” www.substech.com (accessed Oct. 10, 2019).

[91] T. Mattar, K. El-Fawakhry, H. Halfa, and M. Eissa, “Effect of nitrogen alloying on sulphur behaviour during ESR of AISI M41 steel,” *Steel Res. Int.*, vol. 79, no. 9, pp. 691–697, Sep. 2008, doi: 10.1002/srin.200806185.

[92] T. Mattar, “Effect of ESR and nitrogen alloying on the cleanliness of M41 steel,” *J. Mater. Sci. Technol. MST*, vol. 17, no. 1, pp. 35–46, 2009.

[93] Y.-W. Dong, Z.-H. Jiang, Y.-L. Cao, A. Yu, and D. Hou, “Effect of slag on inclusions during electroslag remelting process of die steel,” *Metall. Mater. Trans. B*, vol. 45, no. 4, pp. 1315–1324, Aug. 2014, doi: 10.1007/s11663-014-0070-7.

[94] J. Reitz, M. Maurischat, and B. Friedrich, “Optimized control of slag chemistry for the electroslag remelting of large size ingots,” 2008, doi: 10.13140/rg.2.1.1723.4802.

[95] R. H. Nafziger, “Electroslag melting process,” Bureau of Mines, Albany, OR (USA). Albany Metallurgy Research Center, United States, Technical Report PB-263219; BM-B-669, 1976. Accessed: Oct. 14, 2019. [Online]. Available: https://www.osti.gov/biblio/7213466-electroslag-melting-process.

[96] T. Mattar, A. Fathy, H. El Faramawy, M. Eissa, and K. El fawakhry, “Optimization of desulphurization of tool steels during EAF and ESR processes,” in *Metal2001*, Ostrava, Czech Republic, 2001, p. 6.

[97] K. Mehrabi, M. R. Rahimipour, and A. Shokuhfar, “The effect of slag types and melting rate on electro-slag remelting (ESR) processing,” *International Journal of Iron & Steel Society of Iran*, vol. 2, pp. 37–42, 2005.

[98] M. Hayashi, N. Sano, and P. Fredriksson, “Evaluation of thermodynamic activity of a metallic oxide in a ternary slag from the sulphide capacity of the slag,” *ISIJ Int.*, vol. 44, no. 11, pp. 1783–1786, 2004, doi: 10.2355/isijinternational.44.1783.

[99] M. Eissa and A. EI-Mohammadi, “Effect of physical properties of slag on sulphur removal mechanism during ESR process,” *Steel Res.*, vol. 69, no. 10–11, pp. 413–417, Oct. 1998, doi: 10.1002/srin.199805573.

[100] H. Scholz, U. Biebricher, and H. Franz, “State of the art in VAR and ESR processes – a comparison,” 2014.

[101] K. O. Yu, J. A. Domingue, G. E. Maurer, and H. D. Flanders, “Macrosegregation in ESR and VAR processes,” *JOM*, vol. 38, no. 1, pp. 46–50, Jan. 1986, doi: 10.1007/BF03257955.

[102] “MTEX Toolbox | MTEX.” https://mtex-toolbox.github.io/index.html (accessed May 02, 2020).

[103] V. Javaheri, T. Nyyssönen, B. Grande, and D. Porter, “Computational design of a novel medium-carbon, low-alloy steel microalloyed with niobium,” *J. Mater. Eng. Perform.*, Apr. 2018, doi: 10.1007/s11665-018-3376-9.

[104] T. Nyyssönen, M. Isakov, P. Peura, and V.-T. Kuokkala, “Iterative determination of the orientation relationship between austenite and martensite from a large amount of grain pair misorientations,” *Metall. Mater. Trans. A*, vol. 47, no. 6, pp. 2587–2590, Jun. 2016, doi: 10.1007/s11661-016-3462-2.

[105] T. Nyyssönen, “Quenching and partitioning of high-aluminum steels,” Ph.D. dissertation, Tampere University of Technology, Tampere, Finland, 2017.

[106] B. Birol and M. N. Saridede, “The effect of slag optical basicity on alloying element losses of steel by electroslag remelting (ESR),” *Trans. Indian Inst. Met.*, vol. 69, no. 3, pp. 751–757, Apr. 2016, doi: 10.1007/s12666-015-0549-1.

[107] T. Mattar, “Electro-slag remelting of AISI M41 high-speed tool steel scrap,” in *6th International Tooling Conference, Karlstad*, 2002, pp. 10–13.

[108] T. A. Engh, C. J. Simensen, and O. Wijk, *Principles of metal refining*. Oxford ; New York: Oxford University Press, 1992.

[109] T. R. Bandyopadhyay, P. K. Rao, and N. Prabhu, “Behavior of alloying elements during electro-slag remelting of ultrahigh strength steel,” *Metallurgical and Mining Industry*, vol. 4, no. 1, p. 11, 2012.

[110] M. Eissa, T. Mattar, and K. El fawakhry, “Nitrogen behavior during electro-slag remelting of tool steel,” presented at the Tool Steels in the Next Century, University of Leoben, Leoben, Austria, 1999.

[111] A. Ahmed and A. Fathy, “Effect of slag properties and nitrogen addition on behaviour of alloying elements during ESR of AISI M41 tool steel,”

Ironmak. Steelmak., vol. 35, no. 6, pp. 458–464, Aug. 2008, doi: 10.1179/174328108X318356.

[112] M. R. Eloy and N. Sano, "Nitrogen solubility in CaO-SiO2, CaO-MgO-SiO2, and BaO-MgO-SiO2 melts," *Metall. Trans. B*, vol. 21, no. 1, pp. 97–104, Feb. 1990, doi: 10.1007/BF02658120.

[113] I. Sohn, D. J. Min, and J. H. Park, "Thermodynamic study on the effect of CaF2 on the nitrogen and carbon solubility in the CaO-Al2O3-CaF2 slag system," *Steel Res.*, vol. 70, no. 6, pp. 215–220, Jun. 1999, doi: 10.1002/srin.199905629.

[114] J. P. Hajra and M. Divakar, "Thermodynamics of surfaces and adsorption in the Fe-S, Fe-N, and Fe-S-N systems at 1823 K," *Metall. Mater. Trans. B*, vol. 30, no. 3, pp. 429–433, Jun. 1999, doi: 10.1007/s11663-999-0075-9.

[115] E. R. Martinez, V. O. Espejo, and F. Manjarrez, "The solubility of nitrogen in the CaO-CaF2-Al2O3 system and its relationship with basicity.," *ISIJ Int.*, vol. 33, no. 1, pp. 48–52, 1993, doi: 10.2355/isijinternational.33.48.

[116] X. Shuang, Z. Hui, C. Yang, and W. Qing-xiang, "Change and control of nitrogen in molten steel production process," *J Chongqing Univ: Eng*, vol. 13, no. 1, p. 6, 2014, doi: 10.11835/j.issn.1671-8224.2014.01.02.

[117] J. Burja, F. Tehovnik, M. Godec, J. Medved, B. Podgornik, and R. Barbic, "Effect of electroslag remelting on the non-metallic inclusions in H11 tool steel," *J. Min. Metall. Sect. B Metall.*, vol. 54, no. 1, pp. 51–57, 2018, doi: 10.2298/JMMB160623053B.

[118] S. Li, G. Cheng, Z. Miao, W. Dai, L. Chen, and Z. Liu, "Evolution of oxide inclusions in G20CrNi2Mo carburized bearing steel during industrial electroslag remelting," *ISIJ Int.*, 2018, doi: 10.2355/isijinternational.ISIJINT-2018-072.

[119] H. Doostmohammadi, P. G. Jönsson, J. Komenda, and S. Hagman, "Inclusion characteristics of bearing steel in a runner after ingot casting," *Steel Res. Int.*, vol. 81, no. 2, pp. 142–149, Feb. 2010, doi: 10.1002/srin.200900106.

[120] K. Oikawa, K. Ishida, and T. Nishizawa, "Effect of titanium addition on the formation and distribution of MnS inclusions in steel during solidification.," *ISIJ Int.*, vol. 37, no. 4, pp. 332–338, 1997, doi: 10.2355/isijinternational.37.332.

[121] M. Wakoh, T. Sawai, and S. Mizoguchi, "Effect of S content on the MnS precipitation in steel with oxide nuclei.," *ISIJ Int.*, vol. 36, no. 8, pp. 1014–1021, 1996, doi: 10.2355/isijinternational.36.1014.

[122] H. S. Kim, H.-G. Lee, and K.-S. Oh, "Precipitation behavior of MnS on oxide inclusions in Si/Mn deoxidized steel," *Met. Mater.*, vol. 6, no. 4, pp. 305–310, Jul. 2000, doi: 10.1007/BF03028076.

[123] U. B. Pal *et al.*, "Behavior of ceria as an actinide surrogate in electroslag remelting and refining slags," *Metall. Mater. Trans. B*, vol. 32, no. 6, pp. 1119–1128, Dec. 2001, doi: 10.1007/s11663-001-0100-0.

[124] M. Maeda, T. Yahata, K. Mitugi, and T. Ikeda, “Aluminothermic reduction of titanium oxide,” *Mater. Trans. JIM*, vol. 34, no. 7, pp. 599–603, 1993, doi: 10.2320/matertrans1989.34.599.
[125] S. Duan *et al.*, “Investigation of the oxidation behaviour of Ti and Al in inconel 718 superalloy during electroslag remelting,” *Sci. Rep.*, vol. 8, no. 1, Dec. 2018, doi: 10.1038/s41598-018-23556-3.
[126] L. Yang, G. Cheng, S. Li, M. Zhao, and G. Feng, “Generation mechanism of TiN inclusion for GCr15SiMn during electroslag remelting process,” *ISIJ Int.*, vol. 55, no. 9, pp. 1901–1905, 2015, doi: 10.2355/isijinternational.ISIJINT-2015-253.
[127] L. Yang and G. Cheng, “Characteristics of Al2O3, MnS, and TiN inclusions in the remelting process of bearing steel,” *Int. J. Miner. Metall. Mater.*, vol. 24, no. 8, pp. 869–875, Aug. 2017, doi: 10.1007/s12613-017-1472-8.
[128] D. A. R. Kay and R. J. Pomfret, “Removal of oxide inclusions during AC electroslag remelting,” *J Iron Stee Inst*, vol. 209, no. 12, pp. 962–965, 1971.
[129] J. Fu and J. Zhu, “Change of oxide inclusions during electroslag remelting process,” *Acta Met. Sin*, vol. 7, no. 3, pp. 250–262, 1964.
[130] D. Zhou, X. Chen, J. Fu, P. Wang, J. Li, and M. Xu, “Inclusions in electroslag remelting and continuous casting bearing steels,” *J. Univ. Sci. Technol. BeijingChina*, vol. 22, no. 1, pp. 26–30, 2000.
[131] Z. B. Li, W. H. Zhou, and Y. D. Li, “Mechanism of removal of non-metallic inclusions in the ESR process,” *Iron Steel*, vol. 15, no. 1, pp. 20–26, 1980.
[132] Z. B. Li, J. W. Zhang, and X. Q. Che, “Control of content and composition of non-metallic inclusion in ESR steel,” *J Iron Steel Res*, vol. 9, no. 2, p. 7, 1997.
[133] A. Mitchell, “Oxide inclusion behaviour during consumable electrode remelting,” *Ironmak. Steelmak.*, vol. 1, no. 3, pp. 172–179, 1974.
[134] F. Wang, X. C. Chen, and H. J. Guo, “Influences of adding aluminum on inclusions in H13 steel through P–ESR,” in *Advanced Materials Research*, 2012, vol. 476, pp. 218–226.
[135] B. Zuzek, M. Sedla, and B. Podgornik, “Effect of segregations on mechanical properties and crack propagation in spring steel,” *Frat. Ed Integrità Strutt.*, no. 34, 2015.
[136] C.-B. Shi, X.-C. Chen, H.-J. Guo, Z.-J. Zhu, and H. Ren, “Assessment of oxygen control and its effect on inclusion characteristics during electroslag remelting of die steel,” *Steel Res. Int.*, vol. 83, no. 5, pp. 472–486, 2012.
[137] “HSC Chemistry.” http://www.hsc-chemistry.com/.
[138] C. W. Bale *et al.*, “FactSage thermochemical software and databases, 2010–2016,” *Calphad*, vol. 54, pp. 35–53, Sep. 2016, doi: 10.1016/j.calphad.2016.05.002.
[139] S. Kumar, S. K. Nath, and V. Kumar, “Continuous cooling transformation behavior in the weld coarse grained heat affected zone and mechanical

properties of Nb-microalloyed and HY85 steels," *Mater. Des.*, vol. 90, pp. 177–184, Jan. 2016, doi: 10.1016/j.matdes.2015.10.071.
[140] D. J. Dyson and B. Holmes, "Effect of alloying additions on the lattice parameter of austenite," *J Iron Steel Inst*, vol. 208, no. 5, pp. 469–474, 1970.
[141] J.-P. Schillé, Z. Guo, N. Saunders, and A. P. Miodownik, "Modeling phase transformations and material properties critical to processing simulation of steels," *Mater. Manuf. Process.*, vol. 26, no. 1, pp. 137–143, 2011.
[142] Z. Zhao, C. Liu, Y. Liu, and D. O. Northwood, "A new empirical formula for the bainite upper temperature limit of steel," *J. Mater. Sci.*, vol. 36, no. 20, pp. 5045–5056, 2001.
[143] W. Bleck *et al.*, "Optimisation of microstructure in multiphase steels containing retained austenite," *EUR*, no. 21131, pp. 1–199, 2004.
[144] B. C. De Cooman, "Structure–properties relationship in TRIP steels containing carbide-free bainite," *Curr. Opin. Solid State Mater. Sci.*, vol. 8, no. 3–4, pp. 285–303, 2004.
[145] S. Traint, A. Pichler, K. Hauzenberger, P. Stiaszny, and E. Werner, "Influence of silicon, aluminium, phosphorus and copper on the phase transformations of low alloyed TRIP-steels," *Steel Res. Int.*, vol. 73, no. 6–7, pp. 259–266, 2002.
[146] S. Papaefthymiou, W. Bleck, S. Kruijver, and J. Sietsma, "Influence of intercritical deformation on microstructure of TRIP steels containing Al," *Mater. Sci. Technol.*, vol. 20, no. 2, p. 201, 2004.
[147] B. Arh, B. Podgornik, and J. Burja, "Electroslag remelting: a process overview," *Mater. Technol.*, vol. 50, pp. 971–979, 2016.
[148] R. Kawalla, "Development of ultrahigh strength steel by electroslag refining: Effect of inoculation of titanium on the microstructures and mechanical properties," *ISIJ Int.*, vol. 46, no. 9, pp. 1361–1370, 2006.
[149] Q. Wang, C. Zhang, R. Li, J. Gao, M. Wang, and F. Zhang, "Characterization of the microstructures and mechanical properties of 25CrMo48V martensitic steel tempered at different times," *Mater. Sci. Eng. A*, vol. 559, pp. 130–134, 2013.
[150] J. Man, Y. T. Yang, and G. J. Shao, "The Microstructure and elements distribution of high-chiromium hypereatectoid steel by high-temperature homogenization," *Adv. Mater. Res.*, 2013. https://www.scientific.net/AMR.652-654.975 (accessed May 11, 2018).
[151] N. D'Souza, M. Lekstrom, and H. B. Dong, "An analysis of measurement of solute segregation in Ni-base superalloys using X-ray spectroscopy," *Mater. Sci. Eng. A*, vol. 490, no. 1–2, pp. 258–265, 2008.
[152] M. Wang, X. Zha, M. Gao, Y. Ma, K. Liu, and Y. Li, "Structure, microsegregation, and precipitates of an alloy 690 ESR ingot in industrial scale," *Metall. Mater. Trans. A*, vol. 46, no. 11, pp. 5217–5231, 2015.
[153] J. Miettinen, S. Louhenkilpi, H. Kytönen, and J. Laine, "IDS: Thermodynamic–kinetic–empirical tool for modelling of solidification,

microstructure and material properties," *Math. Comput. Simul.*, vol. 80, no. 7, pp. 1536–1550, 2010.
[154] Y. Chen, Y. Wang, and A. Zhao, "Precipitation of AlN and MnS in low carbon aluminium-killed steel," *J. Iron Steel Res. Int.*, vol. 19, no. 4, pp. 51–56, Apr. 2012, doi: 10.1016/S1006-706X(12)60087-9.
[155] G. Jeanmaire, M. Dehmas, A. Redjaïmia, S. Puech, and G. Fribourg, "Precipitation of aluminum nitride in a high strength maraging steel with low nitrogen content," *Mater. Charact.*, vol. 98, pp. 193–201, Dec. 2014, doi: 10.1016/j.matchar.2014.11.001.
[156] J.-G. Jung, J.-S. Park, J. Kim, and Y.-K. Lee, "Carbide precipitation kinetics in austenite of a Nb–Ti–V microalloyed steel," *Mater. Sci. Eng. A*, vol. 528, no. 16–17, pp. 5529–5535, Jun. 2011, doi: 10.1016/j.msea.2011.03.086.
[157] B. Dutta, E. Valdes, and C. M. Sellars, "Mechanism and kinetics of strain induced precipitation of Nb(C,N) in austenite," *Acta Metall. Mater.*, vol. 40, no. 4, pp. 653–662, Apr. 1992, doi: 10.1016/0956-7151(92)90006-Z.
[158] S. Okaguchi and T. Hashimoto, "Computer model for prediction of carbonitride precipitation during hot working in Nb-Ti bearing HSLA steels.," *ISIJ Int.*, vol. 32, no. 3, pp. 283–290, 1992, doi: 10.2355/isijinternational.32.283.
[159] M. Mukherjee, U. Prahl, and W. Bleck, "Modelling the strain-induced precipitation kinetics of vanadium carbonitride during hot working of precipitation-hardened Ferritic–Pearlitic steels," *Acta Mater.*, vol. 71, pp. 234–254, Jun. 2014, doi: 10.1016/j.actamat.2014.03.016.
[160] F. G. Caballero *et al.*, "Influence of bainite morphology on impact toughness of continuously cooled cementite free bainitic steels," *Mater. Sci. Technol.*, vol. 28, no. 1, pp. 95–102, Jan. 2012, doi: 10.1179/1743284710Y.0000000047.
[161] T. Furuhara, N. Takayama, and G. Miyamoto, "Key factors in grain refinement of martensite and bainite," *Mater. Sci. Forum*, 2010. https://www.scientific.net/MSF.638-642.3044 (accessed Aug. 07, 2018).
[162] T. Furuhara *et al.*, "Phase Transformation from Fine-grained Austenite," *ISIJ Int.*, vol. 48, no. 8, pp. 1038–1045, Aug. 2008, doi: 10.2355/isijinternational.48.1038.
[163] Z. Luo, J. Shen, H. Su, Y. Ding, C. Yang, and X. Zhu, "Effect of substructure on toughness of lath martensite/bainite mixed structure in low-carbon steels," *J. Iron Steel Res. Int.*, vol. 17, no. 11, pp. 40–48, Nov. 2010, doi: 10.1016/S1006-706X(10)60168-9.
[164] A. Saha Podder and H. K. D. H. Bhadeshia, "Thermal stability of austenite retained in bainitic steels," *Mater. Sci. Eng. A*, vol. 527, no. 7–8, pp. 2121–2128, Mar. 2010, doi: 10.1016/j.msea.2009.11.063.
[165] E. Kozeschnik and H. K. D. H. Bhadeshia, "Influence of silicon on cementite precipitation in steels," *Mater. Sci. Technol.*, vol. 24, no. 3, pp. 343–347, Mar. 2008, doi: 10.1179/174328408X275973.

[166] A. S. Podder, I. Lonardelli, A. Molinari, and H. K. D. H. Bhadeshia, “Thermal stability of retained austenite in bainitic steel: an in situ study,” *Proc. R. Soc. Math. Phys. Eng. Sci.*, vol. 467, no. 2135, pp. 3141–3156, Nov. 2011, doi: 10.1098/rspa.2011.0212.

[167] N.-R. V. Bangaru and A. K. Sachdev, “Influence of cooling rate on the microstructure and retained austenite in an intercritically annealed vanadium containing HSLA steel,” *Metall. Trans. A*, vol. 13, no. 11, pp. 1899–1906, Nov. 1982, doi: 10.1007/BF02645933.

[168] J. Hidalgo, K. O. Findley, and M. J. Santofimia, “Thermal and mechanical stability of retained austenite surrounded by martensite with different degrees of tempering,” *Mater. Sci. Eng. A*, vol. 690, pp. 337–347, Apr. 2017, doi: 10.1016/j.msea.2017.03.017.

[169] N. Zhu, Q. Wu, Y. He, X. Lu, L. Li, and P. Hu, “Effect of Ni on the stability of retained austenite and mechanical properties for TRIP steels containing vanadium,” *Steel Res. Int.*, vol. 85, no. 2, pp. 143–154, Feb. 2014, doi: 10.1002/srin.201300098.

[170] I. B. Timokhina, P. D. Hodgson, and E. V. Pereloma, “Effect of microstructure on the stability of retained austenite in transformation-induced-plasticity steels,” *Metall. Mater. Trans. A*, vol. 35, no. 8, pp. 2331–2341, Aug. 2004, doi: 10.1007/s11661-006-0213-9.

[171] K. P. Balan, A. Venugopal Reddy, and D. S. Sarma, “Effect of single and double austenitization treatments on the microstructure and mechanical properties of 16Cr-2Ni steel,” *J. Mater. Eng. Perform.*, vol. 8, no. 3, pp. 385–393, Jun. 1999, doi: 10.1361/105994999770346963.

[172] Y. Luo, H. Guo, X. Sun, M. Mao, and J. Guo, “Effects of austenitizing conditions on the microstructure of AISI M42 high-speed steel,” *Metals*, vol. 7, no. 1, p. 27, Jan. 2017, doi: 10.3390/met7010027.

[173] S. Salunkhe, D. Fabijanic, J. Nayak, and P. Hodgson, “Effect of single and double austenitization treatments on the microstructure and hardness of AISI D2 tool steel,” *Mater. Today Proc.*, vol. 2, no. 4–5, pp. 1901–1906, 2015, doi: 10.1016/j.matpr.2015.07.145.

[174] M. Nurbanasari, P. Tsakiropoulos, and E. J. Palmiere, “A Study of carbide precipitation in a H21 tool steel,” *ISIJ Int.*, vol. 54, no. 7, pp. 1667–1676, 2014, doi: 10.2355/isijinternational.54.1667.

[175] A. G. Haynes and W. Steven, “The temperature of formation of martensite and bainite in low-alloy steel,” *J Iron Steel Inst*, vol. 183, pp. 349–359, 1956.

[176] H. F. Lan, L. X. Du, Q. Li, C. L. Qiu, J. P. Li, and R. D. K. Misra, “Improvement of strength-toughness combination in austempered low carbon bainitic steel: The key role of refining prior austenite grain size,” *J. Alloys Compd.*, vol. 710, pp. 702–710, 2017.

[177] X. Sun, Z. Li, Q. Yong, Z. Yang, H. Dong, and Y. Weng, “Third generation high strength low alloy steels with improved toughness,” *Sci. China Technol. Sci.*, vol. 55, no. 7, pp. 1797–1805, 2012.

[178] X. S. Xie and Y. P. Zeng, “The effect of inclusions on mechanical behaviour in ultra-high strength alloy steels,” in *Mater. Sci. Forum*, 2010, vol. 654, pp. 51–56.
[179] J. P. Naylor, “The influence of the lath morphology on the yield stress and transition temperature of martensitic-bainitic steels,” *Metall. Trans. A*, vol. 10, no. 7, pp. 861–873, 1979.
[180] X. D. Wang, N. Zhong, Y. H. Rong, T. Y. H. (Z Y. Xu), and L. Wang, “Novel ultrahigh-strength nanolath martensitic steel by quenching–partitioning–tempering process,” *J. Mater. Res.*, vol. 24, no. 1, pp. 260–267, Jan. 2009, doi: 10.1557/JMR.2009.0029.
[181] T. Y. Hsu and Z. Y. Xu, “Design of Structure, Composition and Heat Treatment Process for High Strength Steel,” *Mater Sci Forum*, vol. 561–565, pp. 2283–2286, Oct. 2007, doi: 10.4028/www.scientific.net/MSF.561-565.2283.
[182] G. Gao, H. Zhang, X. Gui, P. Luo, Z. Tan, and B. Bai, “Enhanced ductility and toughness in an ultrahigh-strength Mn–Si–Cr–C steel: The great potential of ultrafine filmy retained austenite,” *Acta Mater.*, vol. 76, pp. 425–433, Sep. 2014, doi: 10.1016/j.actamat.2014.05.055.
[183] H. Nakagawa and T. Miyazaki, “Effect of retained austenite on the microstructure and mechanical properties of martensitic precipitation hardening stainless steel,” *J. Mater. Sci.*, vol. 34, no. 16, pp. 3901–3908, 1999, doi: 10.1023/A:1004626907367.
[184] C. Wang, M. Wang, J. Shi, W. Hui, and H. Dong, “Effect of microstructure refinement on the strength and toughness of low alloy martensitic steel,” *J. Mater. Sci. Technol.*, vol. 23, no. 5, pp. 659–664, 2007.
[185] C. Zhang, Q. Wang, J. Kong, G. Xie, M. Wang, and F. Zhang, “Effect of martensite morphology on impact toughness of ultra-high strength 25CrMo48V steel seamless tube quenched at different temperatures,” *J. Iron Steel Res. Int.*, vol. 20, no. 2, pp. 62–67, 2013.
[186] Q. Zhou, L. Qian, J. Tan, J. Meng, and F. Zhang, “Inconsistent effects of mechanical stability of retained austenite on ductility and toughness of transformation-induced plasticity steels,” *Mater. Sci. Eng. A*, vol. 578, pp. 370–376, 2013.
[187] S. C. Kennett and K. O. Findley, “Strengthening and Toughening Mechanisms in Martensitic Steel,” *Adv. Mater. Res.*, vol. 922, pp. 350–355, May 2014, doi: 10.4028/www.scientific.net/AMR.922.350.
[188] H. F. Lan, L. X. Du, Q. Li, C. L. Qiu, J. P. Li, and R. D. K. Misra, “Improvement of strength-toughness combination in austempered low carbon bainitic steel: The key role of refining prior austenite grain size,” *J. Alloys Compd.*, vol. 710, pp. 702–710, Jul. 2017, doi: 10.1016/j.jallcom.2017.03.024.
[189] J. A. da Cruz, J. J. Vilela, B. M. Gonzalez, and D. B. Santos, “Effect of retained austenite on impact toughness of the multi-phase bainitic-

martensitic steel," *Adv. Mater. Res.*, vol. 922, pp. 298–303, May 2014, doi: 10.4028/www.scientific.net/AMR.922.298.
[190] T. Jia, Y. Zhou, X. Jia, and Z. Wang, "Effects of microstructure on CVN impact toughness in thermomechanically processed high strength microalloyed steel," *Metall. Mater. Trans. A*, vol. 48, no. 2, pp. 685–696, Feb. 2017, doi: 10.1007/s11661-016-3893-9.
[191] Y. Liu, L. Shi, C. Liu, L. Yu, Z. Yan, and H. Li, "Effect of step quenching on microstructures and mechanical properties of HSLA steel," *Mater. Sci. Eng. A*, vol. 675, pp. 371–378, Oct. 2016, doi: 10.1016/j.msea.2016.08.087.
[192] B. Ögel and E. Tekin, "The effect of double austenitization on the microstructure and fracture toughness of AISI M2 high speed steel," *Steel Res.*, vol. 69, no. 6, pp. 247–252, Jun. 1998, doi: 10.1002/srin.199805544.
[193] S. Long, Y. Liang, Y. Jiang, Y. Liang, M. Yang, and Y. Yi, "Effect of quenching temperature on martensite multi-level microstructures and properties of strength and toughness in 20CrNi2Mo steel," *Mater. Sci. Eng. A*, vol. 676, pp. 38–47, Oct. 2016, doi: 10.1016/j.msea.2016.08.065.
[194] Y. Zhang *et al.*, "Effects of Ti and a twice-quenching treatment on the microstructure and ductile brittle transition temperature of 9CrWVTiN steels," *Mater. Des.*, vol. 88, pp. 675–682, Dec. 2015, doi: 10.1016/j.matdes.2015.09.056.
[195] S. Zhao, X. Cheng, S. Li, and Y. Zhang, "Effect of austenitising temperature on microstructure and mechanical properties of an ultrahigh strength high alloy G33 steel," *Mater. Res. Innov.*, vol. 17, no. sup1, pp. 277–281, Jul. 2013, doi: 10.1179/1432891713Z.000000000230.

Original publications

I Ali, M., Eissa, M., El Faramawy, H., Porter, D., Kömi, J., El-Shahat, M. F., & Mattar, T. (2017). Electroslag refining of CrNiMoWMnV ultrahigh-strength steel. *Journal of Minerals and Materials Characterization and Engineering*, *5*(6), 385–407.

II Ali, M., Porter, D., Kömi, J., Eissa, M., El Faramawy, H., El-Shahat, M. F., & Mattar, T. (2018). Effect of electroslag refining on cleanness, microstructure and mechanical properties of a newly developed CrNiMoWMnV ultrahigh-strength steel. *Key Engineering Materials*, *786*, 10–22.

III Ali, M., Porter, D., Kömi, J., Heikkinen E.-P., Eissa, M., El Faramawy, H., & Mattar, T. (2019). The effect of electroslag remelting on the cleanliness of CrNiMoWMnV ultrahigh-strength steels. *Journal of Mining and Metallurgy, Section B: Metallurgy*, *55*, 381–395.

IV Ali, M., Porter, D., Kömi, J., Eissa, M., El Faramawy, H., & Mattar, T. (2020). The effect of electroslag remelting on the microstructure and mechanical properties of CrNiMoWMnV ultrahigh-strength steels. *Metals*, *10*(2), 262.

V Ali, M., Porter, D., Kömi, J., Eissa, M., El Faramawy, H., & Mattar, T. (2020). Characterization of the microstructure and precipitates formed during the thermomechanical processing of a CrNiMoWMnV ultrahigh-strength steel. *Steel Research International*, *91*(6),1900580.

VI Ali, M., Porter, D., Kömi, J., Eissa, M., El Faramawy, H., & Mattar, T. (2019). Effect of cooling rate and composition on microstructure and mechanical properties of ultrahigh-strength steels. *Journal of Iron and Steel Research International*, *26*, 1350–1365.

VII Ali, M., Porter, D., Kömi, J., Eissa, M., El Faramawy, H., & Mattar, T. (2019). The effect of double austenitization and quenching on the microstructure and mechanical properties of CrNiMoWMnV ultrahigh-strength steels after low-temperature tempering. *Materials Science & Engineering: A*, *763*, 138169.

Reprinted with permissions from Trans Tech Publications (Paper II), WILEY-VCH (Paper V), and under CC BY (Papers I, IV and VI), CC BY-SA (Paper III) and CC BY-NC-ND (Paper VII) license from Scientific Research Publishing Inc. and Authors.

Original publications are not included in the electronic version of the dissertation.

738. Wijewardhana, Uditha (2020) Sparse recovery algorithms for streaming and multidimensional signals

739. Li, Panpan (2020) Deep eutectic solvents in the production of wood-based nanomaterials

740. Nuortimo, Kalle (2020) Public acceptance in energy technology development and deployment : opinion mining case study

741. Juuti, Timo (2020) The precipitation of Laves phase and its contribution to mechanical properties in novel high-Cr ferritic stainless steels

742. Myllymäki, Pekka (2020) Chemical precipitation in the simultaneous removal of NH_4−N and PO_4−P from wastewaters using industrial waste materials

743. Alcaraz López, Onel Luis (2020) Resource allocation for machine-type communication : from massive connectivity to ultra-reliable low-latency

744. Frondelius, Tero (2020) Development of methods in engine design process

746. Särestöniemi, Mariella (2020) UWB in-body propagation and radio channel characteristics for wireless body area network applications

747. Ashraf, Faisal Bin (2020) River regimes and energy demand interactions in Nordic rivers

748. Kuula, Seppo (2020) Continuous co-creation of knowledge-intensive business services

749. Mustonen, Erno (2020) Vertical productisation over product lifecycle : co-marketing through a joint commercial product portfolio

750. Halttula, Heikki (2020) Enhancing data utilisation in the construction project lifecycle through early involvement and integration

751. Nguyen, Hoang (2020) Ettringite-based binder from ladle slag : from hydration to its fiber-reinforced composites

752. Jahromi, Sahba S. (2020) Single photon avalanche detector devices and circuits for miniaturized 3D imagers

753. Xu, Yingyue (2020) Computational modeling for visual attention analysis

754. Saarela, Martti (2020) Growth management of eHealth service start-ups

755. Kolli, Satish (2020) Sensitization in austenitic stainless steels : quantitative prediction considering multicomponent thermodynamic and mass balance effects

Book orders:
Virtual book store
http://verkkokauppa.juvenesprint.fi

UNIVERSITY OF OULU P.O. Box 8000 FI-90014 UNIVERSITY OF OULU FINLAND

ACTA UNIVERSITATIS OULUENSIS

SERIES EDITORS

A
SCIENTIAE RERUM NATURALIUM
University Lecturer Tuomo Glumoff

B
HUMANIORA
University Lecturer Santeri Palviainen

C
TECHNICA
Postdoctoral researcher Jani Peräntie

D
MEDICA
University Lecturer Anne Tuomisto

E
SCIENTIAE RERUM SOCIALIUM
University Lecturer Veli-Matti Ulvinen

F
SCRIPTA ACADEMICA
Planning Director Pertti Tikkanen

G
OECONOMICA
Professor Jari Juga

H
ARCHITECTONICA
University Lecturer Anu Soikkeli

EDITOR IN CHIEF
University Lecturer Santeri Palviainen

PUBLICATIONS EDITOR
Publications Editor Kirsti Nurkkala

ISBN 978-952-62-2671-2 (Paperback)
ISBN 978-952-62-2672-9 (PDF)
ISSN 0355-3213 (Print)
ISSN 1796-2226 (Online)

UNIVERSITY OF OULU